Study on the aerodynamic interactions of a coaxial rotor hovering in-ground effect

by

Zachary Moore

A thesis submitted to the Graduate Faculty of
Auburn University
in partial fulfillment of the
requirements for the Degree of
Master of Science

Auburn, Alabama
December 14, 2024

Keywords: Counter-rotating coaxial rotor, in-ground effect, aerodynamic interactions

Copyright 2024 by Zachary Moore

Approved by

Vrishank Raghav, Chair, Walt and Virginia Woltosz Associate Professor of Aerospace Engineering
Roy Hartfield, Walt and Virginia Woltosz Professor of Aerospace Engineering
Brian Thurow, W. Allen and Martha Reed Professor of Aerospace Engineering

Abstract

Counter-rotating coaxial rotors (CCR) offer notable advantages over conventional single-rotor systems in flight speed, payload capacity, and maneuverability. As a result, CCR configurations are being considered for future vertical flight applications ranging from urban air mobility to space exploration. However, operating two rotors in proximity on a shared axis results in complex aerodynamic interactions between the rotors that significantly influence individual rotor performance. Understanding these interactions is critical to developing safer and more efficient aircraft. This thesis aims to quantify the aerodynamic rotor-rotor interactions in a CCR operating in-ground effect (IGE), where an additional effect, the rotor-ground interaction, competes with the rotor-rotor interactions in driving the performance characteristics. An experimental facility consisting of two mechanically decoupled rotors with a height-adjustable ground plane was developed. Load measurements were collected to assess the rotor performance. They were coupled with a momentum theory-based theoretical framework to develop empirical correction factors that quantify how these interactions influence the induced power required to hover. The results indicated that in IGE conditions, the rotor-ground interaction dominates rotor performance, leading to significant performance improvements in each rotor. However, rotor-rotor interactions were modified by the presence of the ground, varying by up to approximately 8% in certain conditions, suggesting a complex coupling between rotor-rotor and rotor-ground interactions. A secondary study investigating the effects of Reynolds number on these interactions revealed that the lower rotor interactions were altered. In contrast, the upper rotor interactions were invariant to the Reynolds number, suggesting a discrepancy in the wake characteristics of the upper rotor as it impinges on the lower rotor. This thesis introduces a formulation that isolates the rotor-rotor and rotor-ground interactions of a CCR operating IGE. It provides a fundamental understanding of how ground proximity impacts the power requirements for a hovering CCR and establishes a framework for decomposing the complex aerodynamic interactions between the rotors and the ground.

Acknowledgments

This journey over the past two and a half years has been nothing short of transformative. I've gained more knowledge than in the rest of my academic life combined, and it's led me to places I never imagined, both professionally and personally. This work is a dedication to everyone and everything that has supported me along the way.

My deepest gratitude goes to my parents, Stanley and Alison Moore. You have instilled in me to be great for as long as I can remember, and I have pushed relentlessly to be great in everything I do. I can still hear "dig deep" from the bleachers, a mantra that has driven my work ethic since I started college. Every success I achieve reflects your unwavering support as much as my own efforts.

To my ever-supportive grandpa, Popo, and my precious dog, Shiloh—I know that you both are looking down with the happiest of expressions right now. It's been tough, nearly impossible at times, without your physical presence, but I've only marched on with a greater passion in your honor. I love you both forever and for always.

In my academic journey, I am profoundly grateful for the mentorship of my advisor, Dr. Vrishank Raghav. You have challenged me to grow as a researcher and person, and I am indebted for all the time you've committed to me. Your dedication and guidance have made me confident that I made the right choice to pursue graduate studies. To my committee members, Dr. Brian Thurow and Dr. Roy Hartfield—thank you for your insights and technical support that enhanced my work. I also sincerely thank Dr. Mahendra Bhagwat and Dr. Chris Cameron, whose guidance provided invaluable direction for my research and helped carve my professional skills. Thank you all for taking the time out of your busy schedules to discuss with me.

This research was supported by the U.S. Army/Navy/NASA Vertical Lift Research Center of Excellence (VLRCOE) Cooperative Agreement with Dr. Mahendra Bhagwat, serving as

Program Manager and Technical Agent, Grant Number W911W6-21-2-0002. I thank everybody in the VLRCOE program for your technical support and guidance.

To my colleagues in the Applied Fluids Research Group (AFRG) at Auburn University—thank you for your unwavering support. I want to thank two colleagues (and good friends) specifically: Aditya and Lokesh. You were a couple of the most patient people in the world with me, and I am 100% certain I would not have made it to this point without you. I am eternally indebted.

Lastly, I would be remiss (and probably be in trouble with a couple individuals) if I didn't shout out my closest friends—Joe, Mahi, Ryan, Will, Emma, Erika and Kate. I greatly thank each of you for your steadfast support, and for occasionally dragging me away from the computer to socialize over the past few months. You've kept me grounded and sane, and I'm forever grateful to you all.

When I embarked on this adventure, I planned to complete my M.S. degree and depart for industry. But these past years have brought so much fulfillment and purpose to my life that I am now setting my sights on a terminal degree. So, expect to see me back here in a few years, ready to share my next chapter with even better work. Thank you all, from the bottom of my heart.

Table of Contents

Abstract ii

Acknowledgments iii

List of Tables ix

List of Figures xii

1 Introduction 1

1.1 Conventional single-main rotor configuration 2

1.2 Counter-rotating coaxial rotors 3

1.2.1 Aerodynamic interactions 5

1.3 Literature review 6

1.3.1 Rotor-rotor interactions 7

1.3.2 Rotor-ground interactions 10

1.3.3 Reynolds number effect on a hovering rotor 14

1.3.4 Literature review summary 16

1.4 Motivation and Objectives 16

1.5 Framework 17

2 Methodology 19

2.1 Experimental coaxial rotor facility 19

2.2 Ground plane facility and development 21

2.2.1 Lower rotor thrust stand 22

2.3 Flow field measurements and analysis 23

2.4 Experimental conditions 27

2.5 Performance metrics 29

3 Theoretical Framework 31

3.1 Momentum theory 31

3.2 Baseline empirical power factor definitions 34

3.3 CCR IGE empirical power factor definitions 36

4 Quantification of the aerodynamic interactions of a hovering coaxial rotor system . . 40

4.1 Baseline performance characterization 40

4.1.1 Single rotor 40

4.1.2 Coaxial rotor hovering out-of-ground effect 44

4.2 Coaxial rotor hovering in-ground effect 47

4.2.1 Rotor-ground interactions 47

4.2.2 Rotor-rotor interactions 51

4.2.3 Comparison of the rotor-rotor interactions IGE to OGE 55

4.3 Discussion 57

5 Reynolds number effect on the aerodynamic interactions of a hovering coaxial rotor system 66

5.1 Single rotor performance characterization 66

5.1.1 Out-of-ground effect 66

5.1.2 In-ground effect 67

5.2 Coaxial rotor performance characterization 68

5.2.1 Out-of-ground effect 68

5.2.2 In-ground effect 70

6 Conclusions and future work 77

6.1 Conclusions and implications 77

6.1.1 Conclusions from quantifying the aerodynamic interactions of a hovering coaxial rotor system 77

6.1.2 Conclusions from the Reynolds number effect on rotor performance and aerodynamic interactions 79

6.2 Recommendations for future work 80

References 81

A Measurement uncertainty 88

A.1 Load measurements 88

A.2 Flow field measurements 90

B Experimental facility setup and fabrication considerations 93

B.1 Load cell measurements and calibration 93

B.2 Rotor and thrust stand vibration mitigation 93

C Single rotor flow field velocity contours 98

D Reynolds number effect on the aerodynamic interactions 100

D.1 Net ground effect on the coaxial rotor 100

D.2 Comparison of the rotor-rotor interactions in the presence of the ground with rotor-rotor interactions experienced in OGE conditions 101

E Products during the graduate program 109

List of Tables

2.1 Rotor Blade Characteristics 20

2.2 Summary of the parametric space for the experiments. 28

4.1 Single rotor induced power factor 41

4.2 Comparison of the relative inflow between extreme, intermediate, and out-of-ground operating conditions. 64

B.1 Weight of the original blades in the coaxial rotor system. 94

B.2 Weight of the blades in the coaxial rotor system after replacing the upper rotor blades. 95

List of Figures

1.1 Commercial and military examples of an SMR configuration helicopter [1, 2]. . 2

1.2 Various CCR vehicles developed in the U.S. [2, 3]. 5

1.3 Summary of the aerodynamic interactions for a CCR operating IGE. Helicopter schematic adapted from [4] and modified. 6

1.4 Quantification of the rotor-rotor interactions for a CCR hovering in OGE [5]. . . 9

1.5 2D airfoil section schematic of a rotating blade element. 9

1.6 Vortex trajectories of the upper and lower rotor in a CCR configuration [6]. . . . 10

1.7 Effect of the ground on the thrust of a rotor in hover [7]. 11

1.8 Flow visualization of the vortex structures developed by a rotor operating in two different Reynolds number regimes [8]. On left: $Re = 35,000$. Right: $Re = 275,000$. 15

1.9 Summary of the literature review conducted for this thesis. 17

2.1 CAD representation of the coaxial rotor facility. 20

2.2 CAD representation of the ground plane structure developed for this study. a). Skeleton frame structure that supports the ground plane and ensures flatness and rigidity. b). End stand that provides stability and vertical adjustment of the ground surface relative to the rotor plane. 22

2.3 CAD representation of the fully assembled ground plane structure developed for this study. 23

2.4 CAD representation of the lower rotor thrust stand and full rotor facility. a). Lower rotor thrust stand. b). Full thrust stand assembly. 24

2.5 CAD representation of the lower rotor thrust stand and ground plane assembly. . 25

2.6 Hardware used for the PIV experiments. 26

2.7 Schematic representation of the field-of-view used for PIV. 27

3.1 Momentum theory model for a hovering rotor [9]. 32

4.1 Rotor performance characterization for the lower single rotor hovering out-of-ground effect. 41

4.2 Non-ideal induced power factor for the lower single rotor hovering out-of-ground effect. 42

4.3 Ground effect factor for the lower single rotor hovering at $z/R = 0.4$. 43

4.4 Characterization of the ground effect factor for the single upper and lower rotor across a range of in-ground effect conditions. Compared with semi-empirical models by Cheeseman and Hayden [10, 11]. The total 95% confidence bound for each κ_g factor is within ± 0.040. 43

4.5 Rotor efficiency for the CCR hovering out-of-ground effect across the d/R spectrum of the present study for $C_{T,CCR}/\sigma = 0.13$. 44

4.6 Interference factor for a CCR with $d/R = 0.34$ hovering out-of-ground effect. . 45

4.7 Influence factors of the upper and lower rotors in CCR configuration at $d/R = 0.34$ hovering out-of-ground effect. 45

4.8 Interferences of the CCR hovering out-of-ground effect across the d/R spectrum of the present study. The total 95% confidence bound for each κ factor is within ± 0.045. 46

4.9 Effect of z/R on the net rotor-ground interactions of the CCR operating in IGE conditions. The total 95% confidence bound for each $(\kappa_g)_{CCR}$ factor is within ± 0.085. 49

4.10 Effect of d/R on the net rotor-ground interactions of the CCR operating in IGE conditions.The total 95% confidence bound for each $(\kappa_g)_{CCR}$ factor is within ± 0.085. 50

4.11 Effect of z/R on the rotor-rotor interactions of the CCR operating in IGE conditions. The total 95% confidence bound for each $(\kappa_{CCR})_g$ factor is within ± 0.090. 53

4.12 Effect of d/R on the rotor-rotor interactions of the CCR operating in IGE conditions. The total 95% confidence bound for each $(\kappa_{CCR})_g$ factor is within ± 0.090. 54

4.13 Net change in aerodynamic interactions of the CCR IGE when compared to the aerodynamic interactions experienced in OGE conditions. 58

4.14 a). Rotor thrust sharing for $C_{T,CCR} = 0.0081$. b). Rotor collective pitch angles for $C_{T,CCR} = 0.0081$. 59

4.15 Axial velocity contour for the CCR system operating in OGE conditions at $d/R = 0.34$. 61

4.16 Axial velocity contour for the CCR system operating in $z/R = 0.4$ conditions at $d/R = 0.34$. 61

4.17 Rotor inflow at $d/R = 0.34$. a). CCR configuration. b). Single rotor configuration with thrust matched to CCR. 62

5.1 Single rotor figure of merit variation with tip Reynolds number. 67

5.2 Reynolds number effect on the single rotor induced power factor. The total uncertainties for the upper rotor are within ± 0.025 for all Re_{tip} conditions, and uncertainties for the lower rotor are within ± 0.035. 68

5.3 Effect of Reynolds number on κ_g. a). Upper rotor. b). Lower rotor. The total uncertainties for the upper rotor are within ± 0.045 for all Re_{tip} conditions, and uncertainties for the lower rotor are within ± 0.050. 69

5.4 Rotor-rotor interactions in out-of-ground effect with varying Reynolds number conditions. a). $Re_{tip} = 120,000$. b). $Re_{tip} = 86,500$. c). $Re_{tip} = 53,000$. The total uncertainties for all Re_{tip} conditions are within ± 0.050. 71

5.5 Rotor-rotor interferences in the presence of the ground with varying Reynolds number conditions. a). $Re_{tip} = 120,000$. b). $Re_{tip} = 86,500$. c). $Re_{tip} = 53,000$. The total uncertainties for all Re_{tip} conditions are within ± 0.105. . . . 73

5.6 Influences of the lower rotor on the upper rotor in the presence of the ground with varying Reynolds number conditions. a). $Re_{tip} = 120,000$. b). $Re_{tip} = 86,500$. c). $Re_{tip} = 53,000$. The total uncertainties for all Re_{tip} conditions are within ± 0.095. 75

5.7 Influences of the upper rotor on the lower rotor in the presence of the ground with varying Reynolds number conditions. a). $Re_{tip} = 120,000$. b). $Re_{tip} = 86,500$. c). $Re_{tip} = 53,000$. The total uncertainties for all Re_{tip} conditions are within ± 0.110. 76

A.1 Measurement uncertainty for the time-averaged axial velocity in the measurement FOV for the CCR in OGE conditions. 91

A.2 Axial velocity through the upper and lower rotor planes for the CCR in OGE conditions. 91

A.3 Measurement uncertainty for the axial velocity through the upper and lower rotor planes for the CCR in OGE conditions. 92

B.1 Dimensionalized loads variation for the lower single rotor across the Reynolds number operating conditions of the present study. 94

B.2 Calibration curves for the lower rotor load cell operating at $Re_{tip} = 120,000$. a). Thrust. b). Torque. 95

B.3 Calibration curves for the lower rotor load cell operating at $Re_{tip} = 86,500$. a). Thrust. b). Torque. 96

B.4 Calibration curves for the lower rotor load cell operating at $Re_{tip} = 53,000$. a). Thrust. b). Torque. 97

C.1 Axial velocity contour for the lower single rotor operating in OGE conditions. . 99

C.2 Axial velocity contour for the lower single rotor operating in $z/R = 0.4$ conditions. 99

D.1 Rotor-ground interactions of a CCR operating in IGE conditions. a). $Re_{tip} = 120,000$. b). $Re_{tip} = 86,500$. c). $Re_{tip} = 53,000$. The total uncertainties for all Re_{tip} conditions are within ± 0.095. 103

D.2 Rotor-ground interactions of the upper rotor in the CCR operating in IGE conditions. a). $Re_{tip} = 120,000$. b). $Re_{tip} = 86,500$. c). $Re_{tip} = 53,000$. The total uncertainties for all Re_{tip} conditions are within ± 0.090. 104

D.3 Rotor-ground interactions of the lower rotor in the CCR operating in IGE conditions. a). $Re_{tip} = 120,000$. b). $Re_{tip} = 86,500$. c). $Re_{tip} = 53,000$. The total uncertainties for all Re_{tip} conditions are within ± 0.100. 105

D.4 Net change in aerodynamic interactions of the CCR IGE when compared to the aerodynamic interactions experienced in OGE conditions. a). $Re_{tip} = 120,000$. b). $Re_{tip} = 86,500$. c). $Re_{tip} = 53,000$. 106

D.5 Net change in aerodynamic interactions of the upper rotor in the CCR IGE when compared to the aerodynamic interactions experienced in OGE conditions. a). $Re_{tip} = 120,000$. b). $Re_{tip} = 86,500$. c). $Re_{tip} = 53,000$. 107

D.6 Net change in aerodynamic interactions of the lower rotor in the CCR IGE when compared to the aerodynamic interactions experienced in OGE conditions. a). $Re_{tip} = 120,000$. b). $Re_{tip} = 86,500$. c). $Re_{tip} = 53,000$. 108

Chapter 1

Introduction

The unique operational demands of present and future aerial applications have driven recent advancements in vertical flight. While single-main rotor (SMR) configurations have been well developed since the mid-20th century, there is a growing interest in multi-rotor designs due to recent scientific and exploratory efforts. Multi-rotor systems can offer advantages over SMRs regarding forward flight speed, maneuverability, and payload capacity. As such, military operations aim to implement multi-rotors to improve reconnaissance and fighting capabilities. Additionally, space exploratory and urban mobility efforts are exploring multi-rotor systems to capitalize on these advantages. Many full-scale aircraft use multi-rotor configurations, including counter-rotating coaxial rotors (CCR), tandem rotors, and side-by-side rotors, such as in military aircraft. Smaller drones and unmanned aircraft commonly utilize quad-rotor configurations.

Despite the use of multi-rotor configurations in various applications, the future of vertical flight necessitates further improvements in performance, handling, and safety. Many aspects of these systems must be thoroughly understood and require additional research to address existing knowledge gaps. This thesis aims to experimentally quantify the aerodynamic interactions inherent to the CCR configuration to evaluate their impact on vehicle performance. The introductory chapter provides a historical overview of vertical flight, the CCR configuration, and the unique aerodynamic interactions associated with them. A comprehensive literature review highlights these interactions and how previous research efforts have attempted to understand them. Then, the specific objectives and motivations of the thesis are outlined.

1.1 Conventional single-main rotor configuration

Helicopters and other vertical flight machines offer a unique benefit over fixed-wing aircraft with their hovering capability. This ability is useful for scenarios requiring a short takeoff and landing zone and where quick entries and exits are necessary. A defining characteristic of the SMR configuration is the necessity of a tail rotor to counteract the torque produced by the main rotor and to provide yaw control. The SMR configuration is widely employed in both commercial and military helicopters today. Igor Sikorsky is considered the pioneer of the SMR with his VS-300, which was documented as the first helicopter to fly with a single main rotor and tail rotor system for yaw control [12]. After his successful demonstration, these aircraft quickly gained attention in various aerial settings. Notable examples of contemporary helicopters utilizing the SMR configuration include the Robinson R44 and the Sikorsky UH-60 Black Hawk, as depicted in Fig. 1.1.

(a) Robinson R44

(b) Sikorsky UH-60 Black Hawk

Figure 1.1: Commercial and military examples of an SMR configuration helicopter [1, 2].

While SMRs have been extensively developed for performance and safety, they are constrained by several inherent limitations, one of the most prominent being the restricted forward flight speed. As the vehicle's speed increases, the dynamic pressure on the advancing side deviates from that on the retreating side. To maintain a pressure balance, the blade pitch on the retreating side is increased relative to the advancing side. However, as forward speed rises, the retreating blade reaches a critical pitch angle where an aerodynamic stall occurs, leading to a loss of lift. This phenomenon, known as retreating blade stall, is a primary constraint on helicopter forward speed. Additionally, compressibility effects on the advancing blade further

limit flight speed. The rotor size limits the payload capacity of SMRs, and the overall vehicle footprint is often relatively large due to the tail rotor and boom connecting it to the main frame. Given these limitations and the escalating demands of performance and versatility, alternative rotor designs are becoming increasingly important for research and development.

1.2 Counter-rotating coaxial rotors

One advanced approach to enhancing vertical flight performance is the counter-rotating coaxial rotor (CCR) system. In this design, two rotors are mounted coaxially and rotate in opposite directions. The opposite torques generated by the rotors cancel each other out, eliminating the need for a tail rotor. The absence of a tail rotor allows the engine power to be redirected towards more beneficial functions, such as additional thrust. The ability of the CCR to generate more thrust leads to a higher payload capacity, and the absence of a tail rotor reduces the vehicle footprint. Because the CCR configuration has an advancing blade on both sides of the rotor, they sustain the primary lifting force, and the retreating blade is not forced into a stall regime at high speeds. This allows the CCR to provide sufficient lift at faster forward flight speeds than an SMR.

Despite these advantages over the SMR configuration, CCRs have only gained significant traction in recent years as design methods and manufacturing technologies have drastically improved. Initial attempts towards developing the CCR were met with many challenges associated with the complexity of mounting two rotors coaxially. Although many attempts at flying a CCR were made in the 1930s, the design by French engineers Louis Breguet and René Dorand was one of the most notable. In 1935, their CCR design successfully flew for over an hour but crashed in a subsequent flight, which halted further research on the CCR configuration. Stanley Hiller is labeled as the American pioneer for the CCR, as he successfully flew his XH-44 coaxial helicopter in 1944 [12].

In 1964, the Advancing Blade Concept (ABC) was developed jointly by the U.S. Army and NASA. The concept was a full-scale counter-rotating coaxial rotor system measuring 12 meters in diameter. The ABC was the first significant American breakthrough in the design of CCRs and underwent extensive testing at the NASA Ames wind tunnel facility. In 1971,

Sikorsky Aircraft was contracted by the U.S. Army to design and develop a working prototype of the ABC, which became the XH-59A. This collaboration effort aimed to prove the utility of the CCR design. After various setbacks with the program, the XH-59A finally took flight, accumulating over 100 hours of successful flight time. The vehicle achieved a forward speed of 100 knots, faster than a conventional SMR and showcased unprecedented handling capabilities. Although the helicopter had substantial success, limitations in the blade design caused high structural loads and vibrations, raising safety concerns. The program was eventually halted in 1981 [13].

After the turn of the century, Sikorsky revamped research on the CCR when it developed the X2 Technology Demonstrator (X2TD). This project integrated advancements made over previous decades, including active vibration control, to address the vibratory concerns in the rotor hub of the XH-59A. In addition, the X2TD implemented a propulsor to improve the forward flight performance further. The vehicle made its first flight in 2008 and quickly broke the speed recorded by the XH-59A when it flew upwards of 250 knots [2]. The excitement generated by the X2TD led to the Sikorsky S-97 Raider and SB>1 Defiant, which were developed to compete in the two U.S. Department of Defense Future Vertical Lift (FVL) programs launched in 2009: The Future Aircraft Reconnaissance Aircraft (FARA) and Future Long-Range Assault Aircraft (FLRAA) [2].

Recent advancements in CCR technology have demonstrated the configuration's versatility across a wide range of applications. Beyond military interest, CCRs have gained attention in developing small drones and urban mobility aircraft for their high thrust capacity and compact design. NASA has employed a CCR aircraft on Mars, the Ingenuity rover. The rover arrived on Mars in early 2021 and made its first flight on April 19, 2021. The goal of this vehicle was to demonstrate powered flight on another planet, and it was a remarkable success. Over its lifetime, the Ingenuity rover made 72 flights, 67 more than were initially planned. These various CCRs are depicted in Fig. 1.2.

(a) X2 Technology Demonstrator, 2008

(b) Sikorsky S-97 Raider, 2015

(c) Sikorsky SB>1 Defiant, 2019

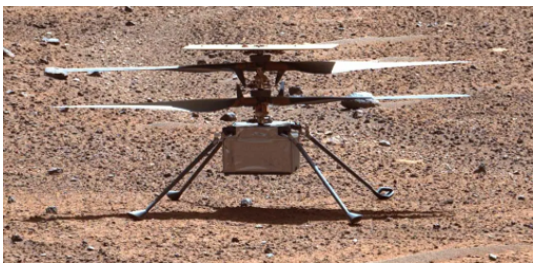

(d) Mars Ingenuity Rover, 2021

Figure 1.2: Various CCR vehicles developed in the U.S. [2, 3].

1.2.1 Aerodynamic interactions

Despite the increasing popularity of the CCR configuration, stacking two rotors in proximity generates unique aerodynamic interactions. These effects are known as rotor-rotor interactions, and they significantly impact the performance of the CCR system. When operating in-ground effect (IGE), an additional interaction occurs, known as the rotor-ground interaction. Typically, rotor-rotor interactions degrade the performance of the rotors, while rotor-ground interactions enhance the performance. These interactions are depicted in Fig. 1.3.

Rotor-rotor interactions arise due to the complex wake structures generated by each rotor. Helical vortices, shed from the blade tips, induce additional inflow through the rotor they originate from and through the adjacent rotor. Furthermore, the wake of the upper rotor directly impinges on the lower rotor of the CCR, significantly increasing the inflow through a large portion of the lower rotor. The combined influence of these effects reduces efficiency for the upper and lower rotors compared to an isolated rotor of the same solidity.

Rotor-ground interactions emerge because the ground is a boundary to the rotor's accelerating wake. When the wake impinges on the ground, the slipstream is directed radially outward, generating an outwash. This interaction reduces the inflow velocity through the rotor plane, altering the rotor performance. Consequently, the rotor requires less power IGE when compared

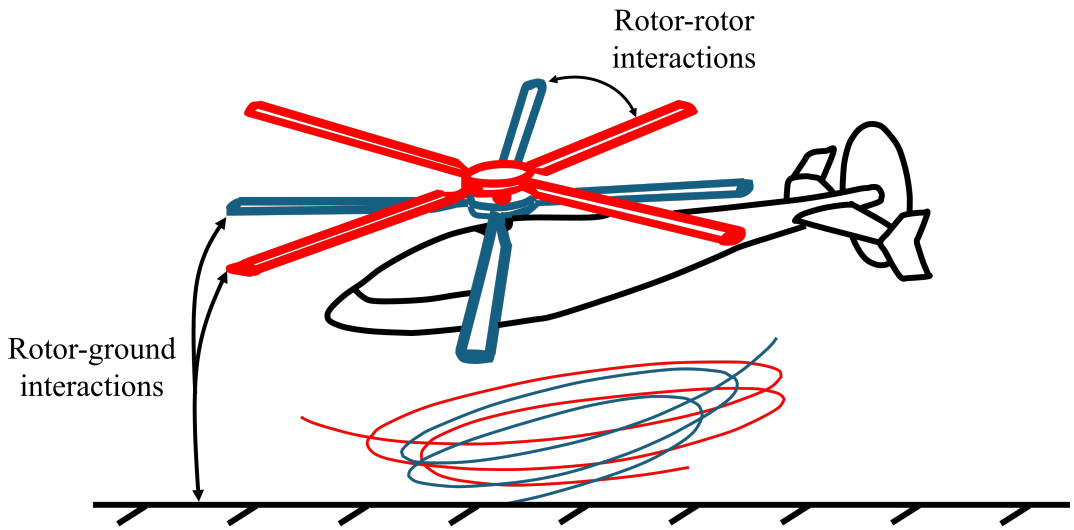

Figure 1.3: Summary of the aerodynamic interactions for a CCR operating IGE. Helicopter schematic adapted from [4] and modified.

to out-of-ground (OGE) conditions at a constant thrust. The ground benefits the individual upper and lower rotors, and provides a net positive effect for the CCR system. However, the degrading effects from the rotor-rotor interactions compete with these beneficial interactions, and the primary objective of this thesis is to investigate the interplay between these competing interactions.

1.3 Literature review

The improved capabilities of CCRs give them unique advantages over SMR configurations, leading to an increased interest in recent years. However, the complexities associated with the CCR design necessitate further research to understand their performance potential fully and to design and develop safe and effective aircraft. One prominent area of research interest focuses on the aerodynamic interactions between the two rotors, and initial studies have explored the interactional effects on the overall performance of the CCR. Still, the current understanding needs improvement, particularly in quantifying the interactions across various operating conditions. This section provides a comprehensive overview of these aerodynamic interactions and identifies critical scientific questions that require further research.

1.3.1 Rotor-rotor interactions

Aerodynamic research on the CCR was first reported in the 1950s with the works of Taylor [14], Harrington [15], and Dingeldein [16]. Taylor used balsa wood dust to visualize the flow through model-scale single and coaxial rotor systems. He observed that for a rotor spacing of 35% of the rotor radius, the tip vortices shed by each rotor of the CCR followed a similar trajectory to that of a single rotor. Harrington and Dingeldein studied the performance of a CCR using load measurements on a full-scale rotor system with a diameter of $7.62m$. For a rotor spacing of 19% of the rotor radius, they noted minimal performance differences between a four-bladed coaxial rotor and a two-bladed single rotor. Subsequent years provided scattered research findings, with research interest being regenerated on the novel ABC concept [17], as summarized in a detailed review by Coleman in [18]. One of the first significant breakthroughs regarding the understanding of CCR performance came from Nagashima et al. [19, 20], where they concluded that the performance of the upper and lower rotors of the CCR have a mutual dependence and that the axial spacing between the rotor planes has a notable effect on the performance.

Harrington's experiments [15] demonstrated that the maximum figure of merit for the coaxial rotor was slightly higher than a single rotor, which he attributed to the differences in rotor solidity. The conventional figure of merit definition is commonly used to compare rotors of equivalent disk loading and uses the minimum induced power in its computation. However, the minimum induced power of a CCR varies from that of a single rotor, as two rotors draw power rather than one. In addition, the disk loading of each rotor deviates from a single rotor due to the unequal thrust share of a CCR when a torque-matched trim is obtained. Leishman et al. [21] modified the single rotor figure of merit definition to account for the unequal thrust share of the CCR, deriving an expression that reflects the hover efficiency of a CCR. In this work, they introduced a parameter termed the interference-induced power factor, which quantifies the induced power consumption of a coaxial rotor relative to two single rotors, each with half the solidity of the coaxial rotor.

Leishman's derivation accounted for the aerodynamic influence of the upper rotor on the lower rotor but neglected the reciprocal effect of the lower rotor on the upper rotor. While

their work was foundational in advancing the understanding of CCR performance, this assumption imposed limitations, particularly given that the lower rotor plays a measurable role in the performance of the upper rotor when the rotor separation is small. More recent studies have extended this work to incorporate blade element momentum theory (BEMT) principles, leading to the development of empirical constants that model the lower rotor's influence on the upper rotor [22]. Over the past two decades, numerous research efforts have proposed both reduced-order and high-order models to gain further understanding of rotor-rotor interactions and their implications on the CCR [23, 24, 25].

Ramasamy [5] conducted an experimental study using Leishman's modified momentum theory foundations to examine the effects of axial separation on the rotor-rotor interactions. In these experiments, a torque-matched trim condition was maintained across a range of thrust conditions. He utilized the experimental data to quantify the interference-induced power factor and influence factors that describe the individual effect of each rotor on the other. As shown in Figure 1.4, the results indicated that the upper rotor consistently outperformed the lower rotor. Additionally, it was observed that the performance of the lower rotor improves as the axial separation decreases while that of the upper rotor degrades.

Similar observations have been reported in other studies [26, 27], and this behavior aligns with the expectations derived from a rotating blade element (see Fig. 1.5). When the rotor spacing is large, the vertical component of velocity (U_P) into the lower rotor plane increases due to the impingement of the fully contracted wake of the upper rotor. This results in a higher inflow angle, ϕ, which degrades the rotor's performance. When the rotor spacing is reduced, the effect of the induced inflow of the lower rotor on the upper rotor is more pronounced, leading to a decline in its performance.

In addition to these foundational studies, numerous experimental investigations have sought to characterize the wake structure of the CCR. Silwal et al. [28] showed that the upper rotor tip vortices convect radially inward and downstream faster than those of the lower rotor. These findings were consistent with the earlier work of Mortimer et al. [6], shown in Fig. 1.6, and it was concluded that the increased vortex spacing benefitted the upper rotor's performance as

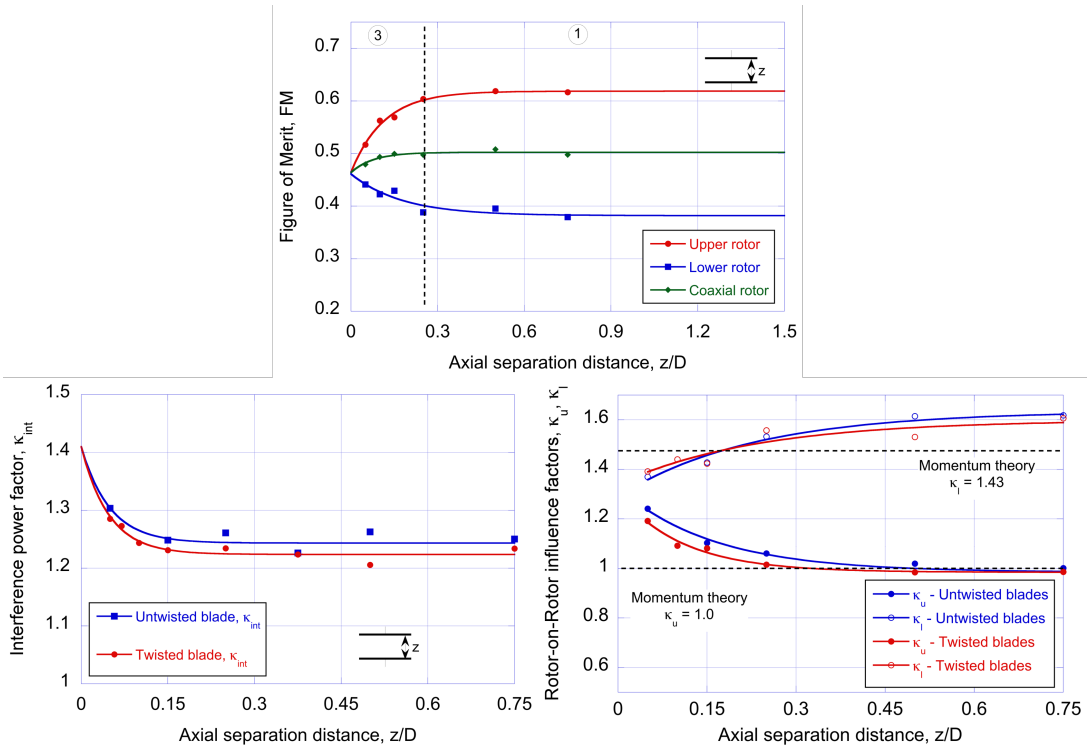

Figure 1.4: Quantification of the rotor-rotor interactions for a CCR hovering in OGE [5].

the induced inflow effects were reduced. Other studies have also observed unique wake characteristics of a CCR [29, 30, 31], including a study done by Shukla [32], where they noticed mutual interactions between the upper and lower rotor's vortices in the near-wake below the lower rotor.

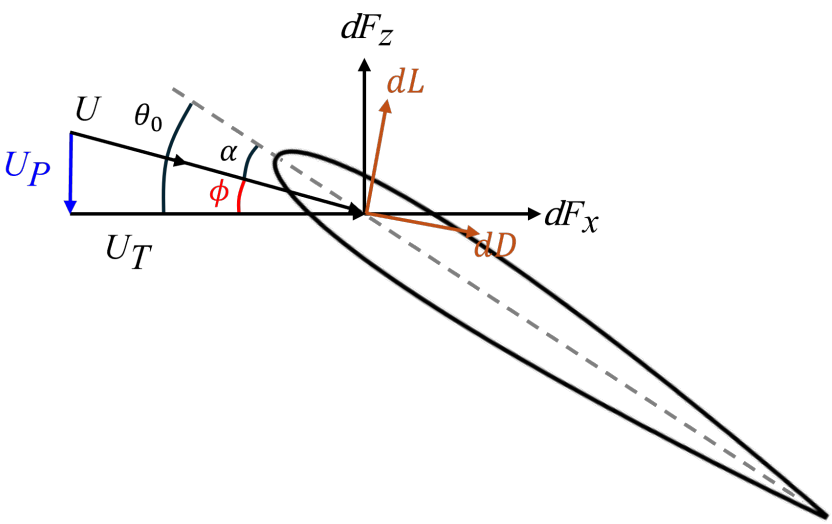

Figure 1.5: 2D airfoil section schematic of a rotating blade element.

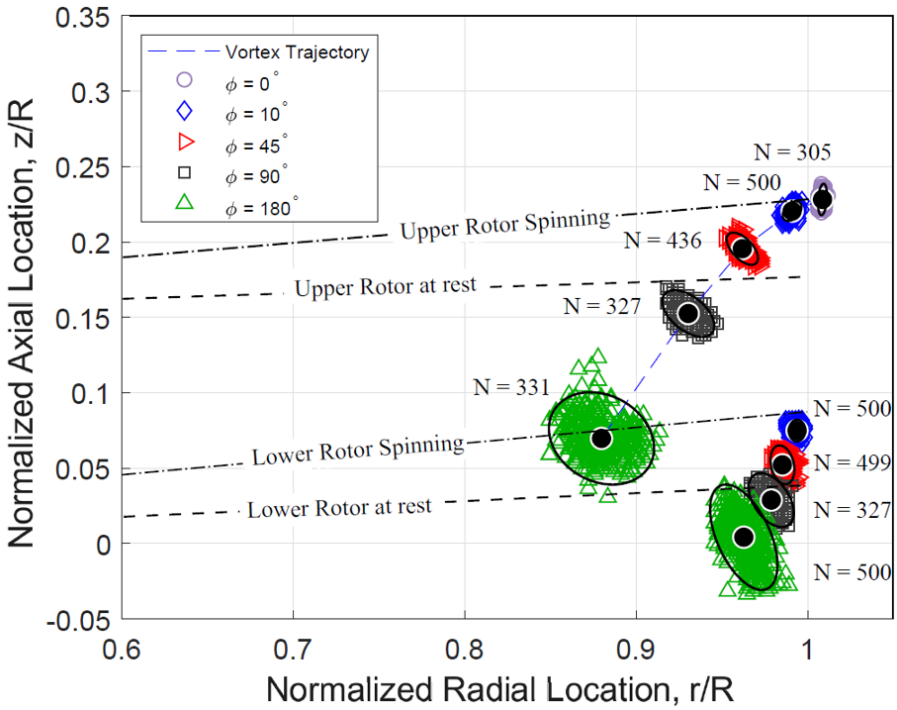

Figure 1.6: Vortex trajectories of the upper and lower rotor in a CCR configuration [6].

Previous model formulations and experimental studies on understanding the rotor-rotor interactions have laid a critical foundation for the development and design of coaxial rotor systems. However, a knowledge gap exists in experimentally quantifying these interactions and how the rotors perform under various operating conditions. For example, Ramasamy [5] quantified the coaxial rotor interactions in OGE, but expanding this understanding to encompass a broader range of flight conditions is essential. Such efforts are critical to advancing the integration of CCR configurations in future vertical lift platforms and ensuring their success across various operational scenarios.

1.3.2 Rotor-ground interactions

The previous section detailed the current understanding of rotor-rotor interactions in CCR and their impact on the upper and lower rotors. In OGE conditions, rotor-rotor interactions dominate each rotor's performance. However, as the system transitions into IGE operation, additional interactional effects compete with the rotor-rotor interactions. This section focuses on

rotor-ground interactions and their effect on rotor performance. While much research on rotor-ground interactions has involved the SMR configuration, studies on CCR configurations have been much more limited.

Ground effect on a lifting rotor is a favorable phenomenon, typically quantified by comparison to OGE performance using one of two methods: trimmed or untrimmed conditions. Trimmed conditions are achieved by reducing the rotor collective pitch or rotational speed to maintain a constant thrust, reducing the power required to sustain hover. In contrast, untrimmed conditions occur when the rotor collective or rotational speed is held constant, leading to a significant increase in thrust production while slightly reducing the power.

Untrimmed experiments have been extensively studied in the literature [33, 34, 35, 36], and a comprehensive summary of performance data from these studies and more is shown in Fig. 1.7. The physical foundation of the thrust increase can also be explained using Fig. 1.5, where the induced inflow through the rotor decreases as the rotor approaches the ground, which reduces ϕ for a fixed rotor collective.

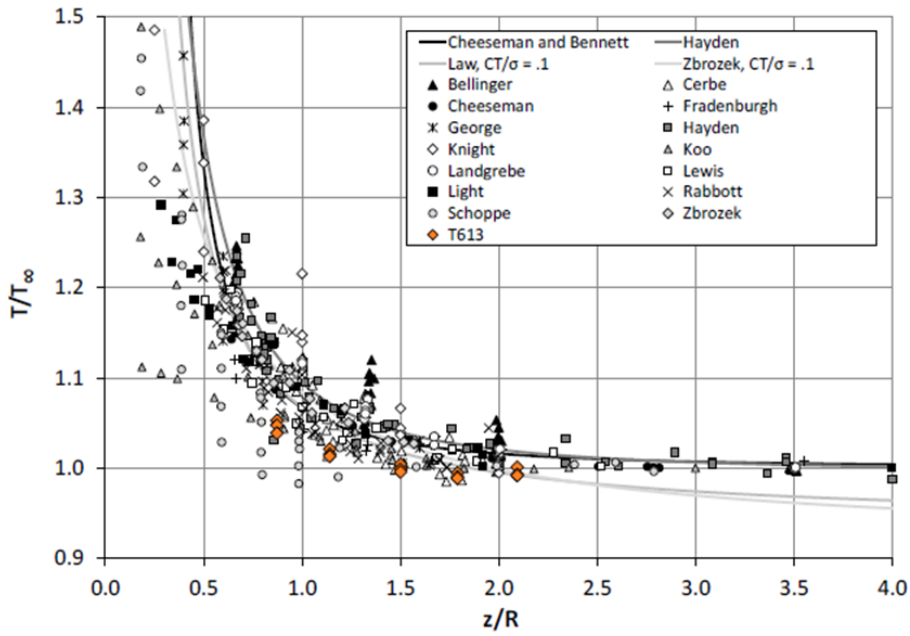

Figure 1.7: Effect of the ground on the thrust of a rotor in hover [7].

Several models have been developed to predict the thrust augmentation of a rotor due to the ground, with two key models by Cheeseman and Hayden [10, 11] still frequently referenced in modern studies for comparison with experimental data. Cheeseman's model [10] was based

on Betz [37] method of images, in which the rotor is considered a sink, and the ground as an image sink at twice the height of the rotor. However, the image sink added inflow to the rotor, decreasing its thrust. Cheeseman modified this by treating the rotor and image as sources, reducing the rotor inflow and increasing the thrust. Eq. 1.1 presents Cheeseman's model, where T_{IGE} and T_{∞} represent the rotor thrusts IGE and OGE, respectively, R is the rotor radius and z is the height from the rotor to the ground surface. Cheeseman's model proved valid, but improvement in its accuracy was still sought as it tended to overpredict much of the experimental data.

$$\frac{T_{IGE}}{T_{OGE}} = \frac{1}{1 - \left(\frac{R}{4z}\right)^2} \tag{1.1}$$

Subsequent efforts to improve the accuracy of ground effect modeling led to the development of an additional model by Hayden [11]. Building upon Cheeseman's work, Hayden introduced semi-empirical corrections derived from experimental data of helicopters operating in IGE conditions. These corrections were incorporated into the model to enhance its predictive accuracy, and the resulting formulation is expressed as

$$\frac{T_{IGE}}{T_{OGE}} = A + B\left(\frac{2R}{z}\right)^2 \tag{1.2}$$

where A and B are empirical constants and $A = 0.9926$ and $B = 0.03794$. This model was observed to predict the rotor performance IGE more accurately.

In addition to rotor performance modeling, extensive research has been carried out to characterize the flow field of a rotor hovering IGE. Since rotor wake dynamics are a driving characteristic of rotor performance, understanding the wake behavior is crucial for performance prediction. Light [36] conducted shadowgraph experiments to quantify the tip vortices and found that the spacing between vortices was larger for IGE conditions, directly affecting the induced inflow through the rotor plane. These experimental results were compared with a free-wake model and demonstrated strong agreement. Various other efforts have been carried out to

develop wake models, understand wake geometry in forward flight, and characterize the vortex structure [38, 39, 40, 41].

Beyond performance modeling and wake characterization IGE, rotor outwash has garnered significant research interest, particularly for large aircraft that generate substantial air velocities. Rotor outwash and the associated brownout phenomenon pose a serious safety concern for the helicopter, as airborne particulates can limit pilot visibility and loose objects may be re-ingested into the rotor, potentially causing damage to the vehicle. Furthermore, the strong forces generated by rotor outwash can affect nearby personnel, structures, and equipment. Ghosh [42] conducted a computational study to understand the outwash produced by various rotor configurations and found that each configuration generates distinct outwash characteristics, with tandem rotor configurations appearing to hinder pilot visibility the least. However, earlier research by Schane [43] reported downwash velocities approaching $30\ m/s$ for the CH-47A, and Ramasamy [44] observed strong outwash velocities up two rotor radii away from the blade tips, highlighting the potential for substantial impact on the surrounding environment.

Numerous studies have been conducted to characterize the IGE behavior of SMR configurations, and some investigations have been conducted into multi-rotor setups. However, research on the CCR configuration remains limited, with two notable studies by McAlister [26] and Silwal [45]. McAlister investigated the effect of the ground on rotor performance through load measurements, maintaining the torque balance by holding the upper rotor collective pitch constant and adjusting the lower rotor collective. The results showed a significant thrust increase as the CCR approached the ground, with the lower rotor experiencing the greatest thrust benefit. Although this was a seminal study, the lack of a thrust trim condition allowed for changes in the aerodynamic environment across various IGE conditions, which affected the rotor-rotor interactions.

Silwal imposed a thrust trim condition and torque balance to address this limitation. In this experiment, the CCR system exhibited performance characteristics similar to that predicted by Hayden's [11] model for a single rotor. However, significant variations were observed in the upper and lower rotor performance as the ground height changed. It was concluded that both the

rotor-rotor and rotor-ground interactions influence rotor performance, competing to dominate under different conditions.

Across these studies, a gap remains in understanding the coupled nature between rotor-rotor and rotor-ground interactions in a CCR system. As such, a comprehensive study is needed to elucidate how these interactions compete and influence rotor performance. Quantifying the performance effect of these interactions is critical for informing future design and development of CCRs while also providing deeper insight into the complex aerodynamic behavior of this configuration. Such research will contribute to optimizing CCR systems for various operational conditions.

1.3.3 Reynolds number effect on a hovering rotor

The existing literature has largely assumed that the aerodynamic interactions experienced by a CCR IGE remain consistent, irrespective of rotor size, rotational speed, or operating environment. However, with the rapid expansion of rotorcraft into diverse applications, these rotor parameters and characteristics are subject to significant variation. A standard parameter used to classify aerodynamic behavior is the Reynolds number, which measures the relative influence of inertial versus viscous forces. In conventional rotorcraft – such as those used for personal, medical, or military applications, inertial forces dominate, and the Reynolds number typically ranges on the order of 10^6 and higher. However, in small drones, urban mobility, and interplanetary exploration vehicles, the Reynolds number is often much lower, on the orders of 10^3 – 10^5. Therefore, understanding the aerodynamic performance across various Reynolds number conditions is crucial for effectively designing and optimizing future rotorcraft systems.

In experimental research, it is often difficult to conduct tests at Reynolds numbers matching those of full-scale helicopters without using air-compressed enclosures [46]. Therefore, it is essential to understand how model-scale tests in research experiments differ from full-scale vehicles. Singleton [47] performed a study in NASA Langley's wind tunnel aimed to understand the scaling parameters that must be considered in model-scale testing and concluded that the Reynolds number should be matched as high as feasible for the test setup, as lower Reynolds numbers increase the torque requirements, leading to discrepancies in performance predictions.

Due to the relative ease in performing experiments in lower Reynolds number regimes, there is extensive data to understand the aerodynamic behavior of rotors at low Reynolds numbers [48, 49]. Ramasamy [8, 50] conducted experiments to investigate the wake structure of low Reynolds number rotors and assess the influence of airfoil geometry on performance. Striking flow visualization images comparing a rotor operating at two Reynolds number regimes are seen in Figure 1.8, which shows stark differences in the wake structure. Analysis of the flow field indicated that the vortex growth at low Reynolds numbers was similar to higher Reynolds numbers. However, the roll-up time from the blade tip was prolonged. Additionally, the vortex sheet convecting from the blade's trailing edge was thicker and had more turbulent structures. These characteristics contribute to increased blade profile drag, resulting in higher losses. Research efforts have focused on reducing the profile drag while enhancing the lift of blades designed for low Reynolds numbers [51, 52].

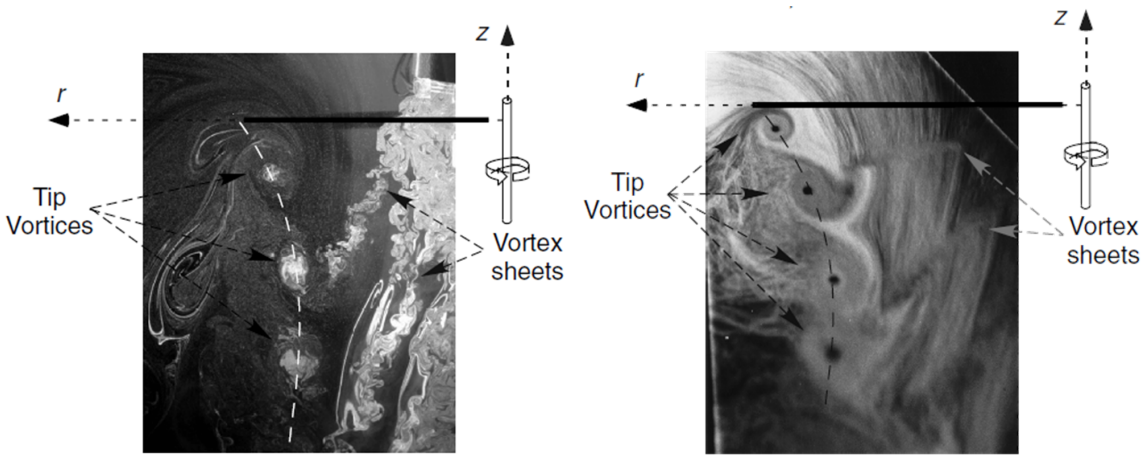

Figure 1.8: Flow visualization of the vortex structures developed by a rotor operating in two different Reynolds number regimes [8]. On left: $Re = 35,000$. Right: $Re = 275,000$.

The impact of Reynolds number on coaxial rotors has received limited attention. However, initial studies have provided valuable insight into their performance characteristics [53, 54, 55, 32]. For instance, Shukla [53, 32] conducted two experiments to assess coaxial rotor performance at low Reynolds numbers and observed a general improvement in performance with increasing Reynolds number. It was also observed that the maximum figure of merit—an efficiency parameter for rotor performance—was higher for the upper rotor than an isolated single rotor, attributed to viscous swirl recovery of the lower rotor.

Though rotor aerodynamics have been characterized in model-scale experiment ranges in the order of ($10^3 - 10^5$), there remains a knowledge gap in understanding how Reynolds number affects the performance of the CCR configuration, particularly regarding its impact on the aerodynamic interactions between the rotors. Therefore, this thesis aims to quantify these interactions and understand how the Reynolds number affects the interplay between the rotors.

1.3.4 Literature review summary

The literature review conducted for this thesis is summarized in Fig. 1.9. Two main aspects driving CCR performance are reviewed in the rotor-rotor and rotor-ground interactions. While the rotor-rotor interactions have been well characterized in literature, the coupled nature between the rotor-rotor and rotor-ground interactions has received limited attention thus far. In addition, data towards quantifying the effect of the Reynolds number on the induced power of a CCR is limited. Some key scientific questions requiring further exploration are:

1. How does in-ground effect operation affect the induced power of a CCR system and its individual rotors?

2. How can the competitive effects of the rotor-rotor and rotor-ground interactions be quantified separately?

3. What is the effect of Reynolds number on the induced power of the CCR system and its individual rotors?

1.4 Motivation and Objectives

Through an experimental approach, this thesis investigates the aerodynamic interactions influencing a counter-rotating coaxial rotor system operating in-ground effect (IGE). The primary objective is to quantify the impact of these interactions on the induced power, while the secondary objective focuses on evaluating the role of Reynolds number in shaping these interactions. The motivation driving these research goals is outlined as follows:

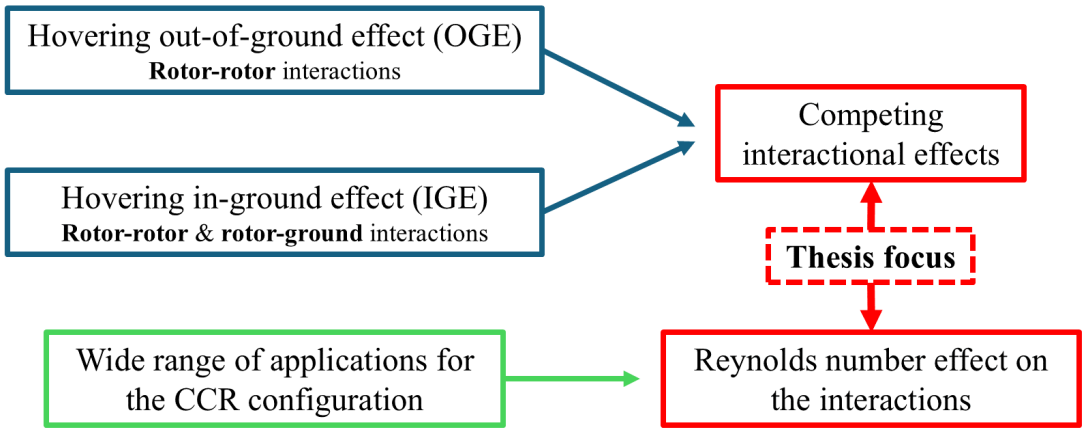

Figure 1.9: Summary of the literature review conducted for this thesis.

1. Developing a method to quantify the aerodynamic interactions of a CCR IGE by coupling experimental data with computationally efficient tools offers significant advantages for design and development. Such methods facilitate rapid iteration and optimization during the design phase.

2. Quantifying the power requirements of a CCR IGE is critical for advancing the understanding of its performance characteristics. This knowledge serves as a foundation for developing predictive models and simulations, ultimately contributing to more informed and safer flight strategies.

3. Investigating how aerodynamic interactions vary with Reynolds number is essential, as the CCR configuration exhibits unique performance advantages that are applicable across a broad spectrum of vehicle sizes and operational scenarios. Understanding these effects enables tailored designs for diverse applications.

1.5 Framework

The objectives of this thesis were carried out through an experimental facility equipped with a mechanically decoupled CCR. Each rotor was equipped with instrumentation to measure the loads experienced by each rotor. These experimental measurements were coupled with a theoretical framework developed using momentum theory foundations. The experimental facility

and framework are discussed in Chapters 2 and 3, respectively. Then, Chapter 4 characterizes the performance measurements and provides an in-depth discussion on the performance of the counter-rotating coaxial rotor operating in-ground effect. Next, Chapter 5 provides insight into the Reynolds number effect on the aerodynamic interactions, and the thesis concludes in Chapter 6 with a summary of the key findings, discusses their importance and implications, and provides directions for future research.

Chapter 2

Methodology

2.1 Experimental coaxial rotor facility

The coaxial rotor setup consisted of two identical, mechanically decoupled rotors mounted on a vertical hover thrust stand with adjustable inter-rotor spacing, d/R, as illustrated in Fig. 2.1. Each rotor was comprised of two untwisted, rectangular planform blades with length of $0.245m$ and an NACA 0015 airfoil section (sourced from Align Main Hobbies [56].). Table 2.1 summarizes the relevant rotor characteristics. The lower rotor was positioned on a vertical stand (see Sec. 2.2.1 for more details), while the upper rotor was mounted on a cantilevered beam. Both rotors were aligned coaxially via an external support structure, which has been shown to have negligible influence on their aerodynamic performance [27]. The inter-rotor spacing was adjusted by sliding the upper rotor along a vertical rail. The closest wall was at least $6R$ from the rotor tip in all directions. The ground plane was constructed from a rigid aluminum honeycomb structure and is discussed in further detail in Sec. 2.2. The rotor height above the ground plane was defined using the following non-dimensional conventions:

- $(z/R)_l$: The normalized distance between the lower rotor and the ground plane.
- $(z/R)_{CCR}$ = $(z/R)_l$ + 0.5 d/R: The normalized effective height for the coaxial system. This distance corresponds to the mid-plane between the two rotors.
- $(z/R)_u$ = $(z/R)_l$ + d/R: The normalized distance between the upper rotor and the ground plane.

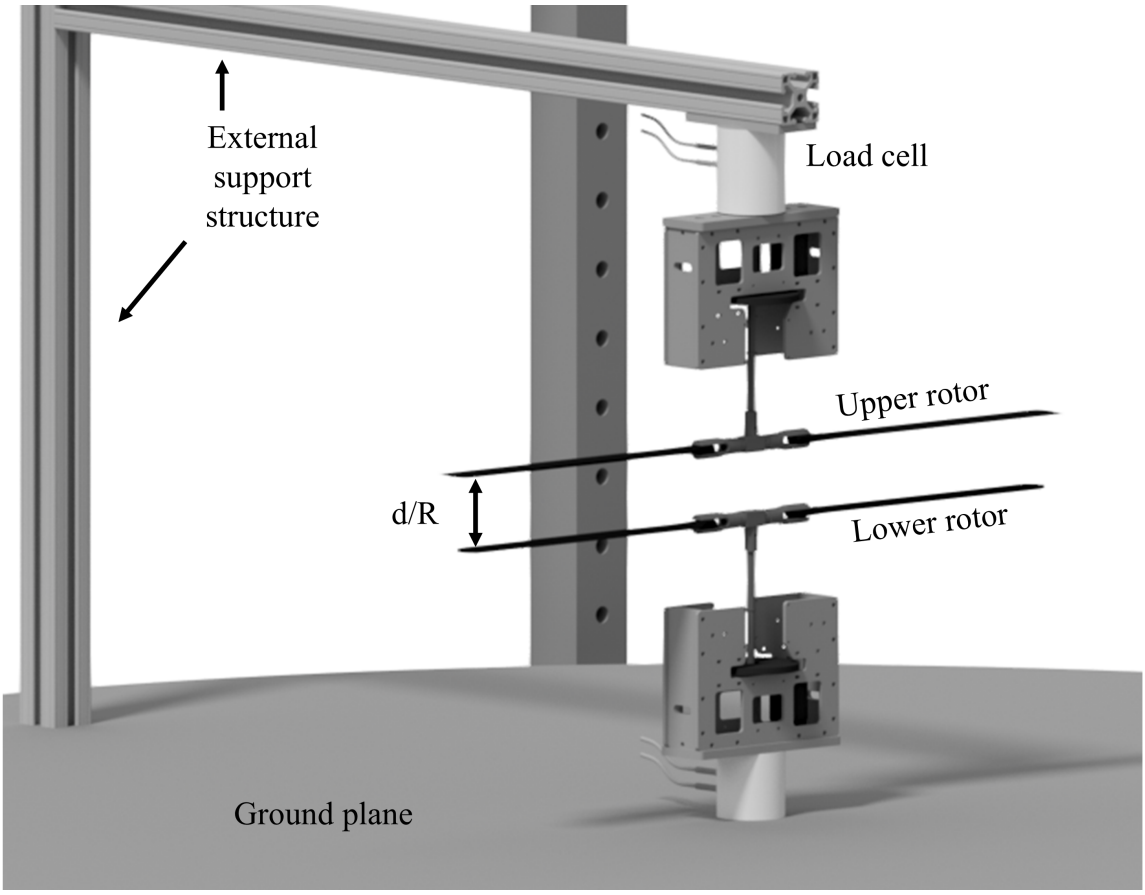

Figure 2.1: CAD representation of the coaxial rotor facility.

Table 2.1: Rotor Blade Characteristics

Parameter	Value, m
Rotor radius, R	0.292
Number of blades, N_b	2
Chord, c	0.028
Root cutout	0.078
Rotor solidity, σ	0.061
Tip Reynolds number, Re_{tip}	120,000; 86,500; 53,000
Airfoil section	NACA 0015

A helical gear transmission system, with a gear ratio of 11.25:1 was used to transmit rotational motion and torque from a brushless DC (BLDC) motor to each rotor shaft, and an electronic speed controller (ESC) ensured constant angular velocity for both rotors. The upper rotor rotated counterclockwise, and the lower rotor rotated clockwise when viewed from above, forming a counter-rotating pair. The blade pitch angle was adjusted using three servo motors (each providing a holding torque of $0.2N \cdot m$) connected to the fixed frame side of the

swashplate. The servos were controlled via an Arduino Mega interfaced with LabVIEW, and a digital pitch gauge (with $0.1°$ resolution) was used to measure and verify the pitch angle at three azimuthal locations on each blade to ensure a constant rotor collective. Rotor angular velocity was measured using an NPN Hall effect sensor. Two calibrated load cells mounted to the rotor assembly measured the axial force and torque of each rotor. Data acquisition, including load cell and Hall sensor measurements, was conducted over 750 rotor revolutions at a sampling rate of 1 kHz, using an NI DAQ system interfaced with a computer via LabVIEW. These measurements were time-averaged to mitigate temporal fluctuations and ensure accurate characterization of rotor performance. More information regarding the load cell calibration and structural vibration issues faced during rotor operation are discussed in appendix B.

2.2 Ground plane facility and development

This thesis focused on studying rotor aerodynamics in proximity to a ground surface, necessitating the implementation of a robust ground plane. To approximate an infinite ground boundary for the rotor, the ground plane dimensions were specified to extend beyond one rotor diameter from the blade tips in all directions [44]. Additionally, the ground plane required adjustability in height relative to the rotor plane, enabling measurements across various IGE conditions. Finally, the ground surface was required to be smooth and flat to minimize undesired flow disturbances and potential obstructions.

To meet these specifications, a rigid aluminum honeycomb panel was procured from Plascore, Inc. (Zeeland, MI). The panel had a thickness of $19mm$ and a hexagonal-shaped cell size of $10mm$. It was laminated on both sides with $0.5mm$ thick aluminum sheets to ensure a smooth, flat surface conducive to experimentation. A circular ground plane shape was required to approximate axisymmetric conditions, with a radius exceeding $3R$ (approximately $0.9m$ in dimensional coordinates).

The final ground plane was fabricated from two $1.22m \times 2.44m$ rectangular panels. A half-circle with a radius of $3.125R$ was cut from each to form two matching sections that created a seamless, circular surface of the desired size. Each aluminum honeycomb half-circle weighed approximately $5kg$. This design ensured a robust, flat ground plane that met the dimensional

and surface quality requirements. The final ground plane half-circles were spray painted with a matte black paint to minimize surface reflections from the laser during PIV experiments.

To meet the requirement of height adjustability, a support structure was developed to hold the ground plane beneath the lower rotor and allow for vertical adjustments, as illustrated in Fig. 2.2. This structure utilized T-slotted framing rails to form a rigid framework capable of supporting the ground plane without deformation or sagging (Fig. 2.2a). Each end of the frame was mounted to a stand (Fig. 2.2b) that was equipped with sliding bearings to facilitate smooth, precise height adjustments of the ground plane. A CAD representation of the fully assembled adjustable ground plane structure is provided in Fig. 2.3.

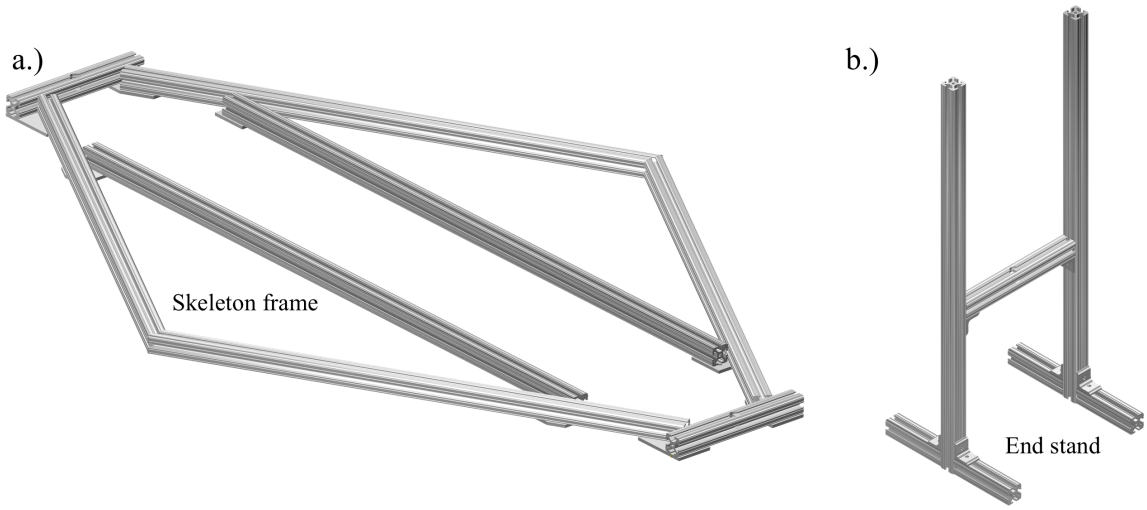

Figure 2.2: CAD representation of the ground plane structure developed for this study. a). Skeleton frame structure that supports the ground plane and ensures flatness and rigidity. b). End stand that provides stability and vertical adjustment of the ground surface relative to the rotor plane.

2.2.1 Lower rotor thrust stand

A dedicated thrust stand was designed for the lower rotor to minimize intrusion within the ground plane structure described in Sec. 2.2. This stand comprised a cylindrical vertical beam, constructed from carbon steel alloy, affixed perpendicularly to a flat base plate that rests directly on the laboratory floor (Fig. 2.4a). The assembled thrust stand weighed approximately $27kg$.

Two angled brackets extended horizontally from the thrust stand to secure it to the external main frame, arresting any movement of the stand (Fig. 2.4b). This setup ensured that the axes

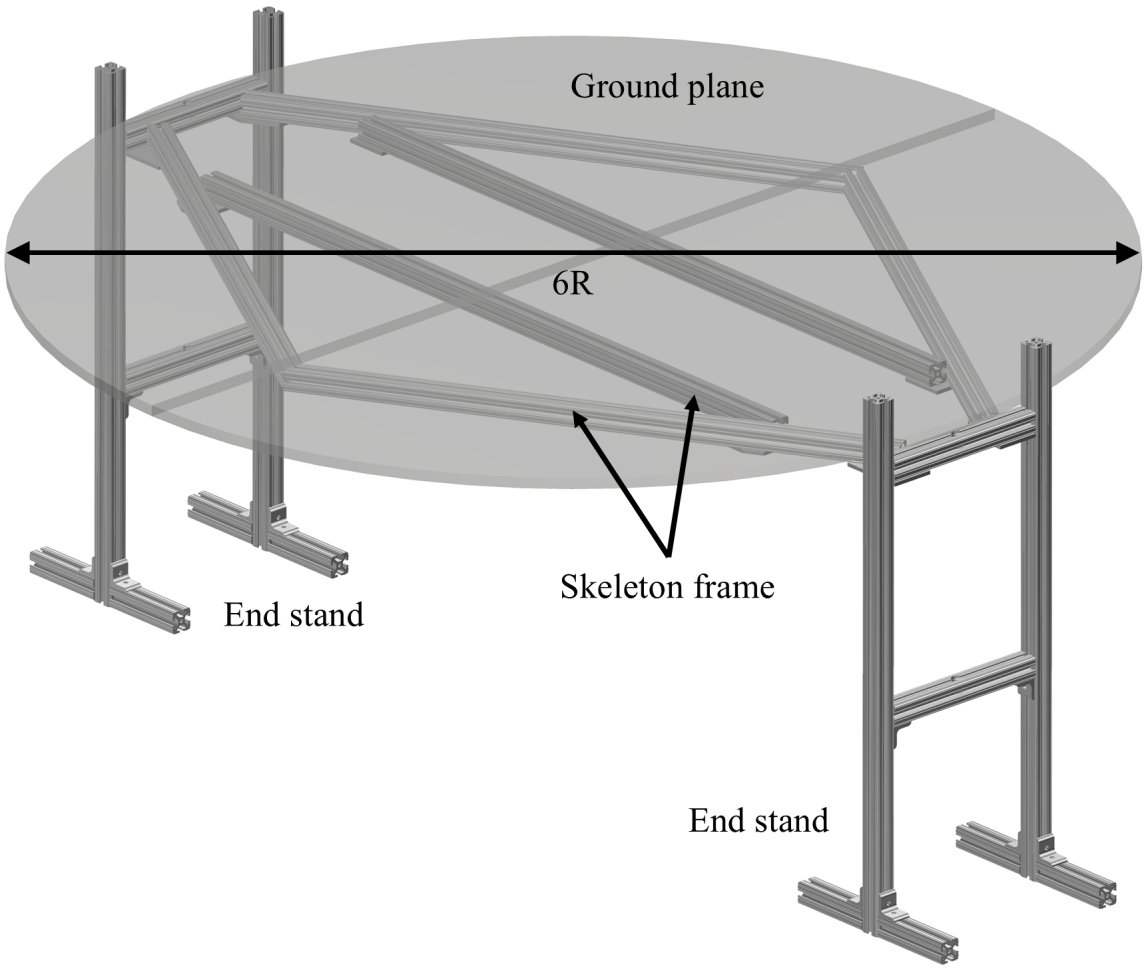

Figure 2.3: CAD representation of the fully assembled ground plane structure developed for this study.

of the upper and lower rotors remained coaxially aligned. The lower rotor was mounted on this stand with its rotor plane positioned approximately $4.3R$ $(1.31m)$ above the floor.

The vertical beam was approximately $63.5mm$ in diameter and was centered along the vertical axis of the ground plane. To accommodate this without disrupting the ground plane surface, a cutout slightly larger than the beam diameter was incorporated. The assembled configuration of the lower rotor thrust stand and the ground plane is shown in Fig. 2.5.

2.3 Flow field measurements and analysis

To investigate the underlying flow physics governing the measured rotor performance of a CCR IGE, two-dimensional, two-component particle image velocimetry (2D-2C PIV) was employed

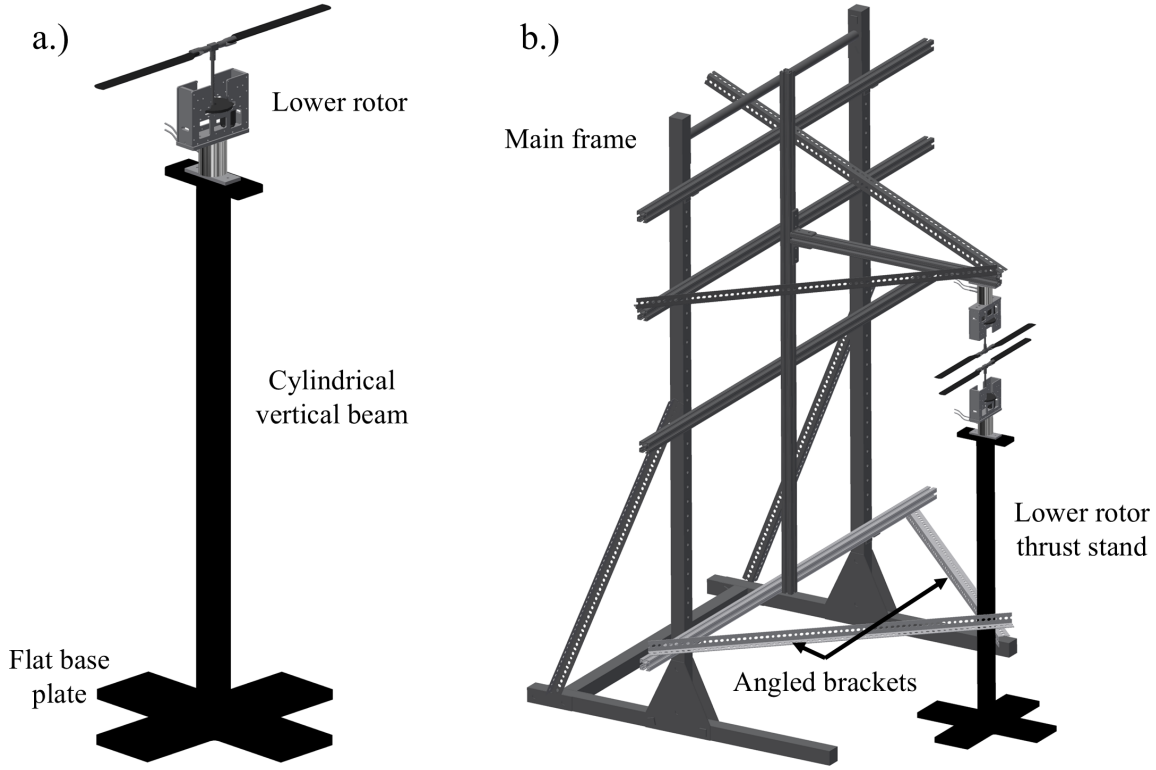

Figure 2.4: CAD representation of the lower rotor thrust stand and full rotor facility. a). Lower rotor thrust stand. b). Full thrust stand assembly.

to measure the velocity field through the rotor planes. The setup consists of a Photonics dual-head Nd-YLF laser with a 527 nm wavelength and an energy output of $30mJ$ per pulse at $1kHz$ to illuminate the field-of-view (FOV), a LaVision programmable timing unit (PTU X) for precise timing control, and a Phantom VEO4K 990 high-speed camera (4096 x 2304 resolution) to capture the flow field. The camera was fitted with a 135 mm fixed focal length lens at an aperture setting of f/4, covering the region from 0.3R to beyond the rotor tip. A thin laser sheet was obtained using a series of cylindrical lenses and aligned vertically to the rotor axis to illuminate the region of interest (ROI). Calibration was performed using a custom-built single-sided target to map camera pixel dimensions to real-world coordinates, resulting in a scale factor of 13.86 pixels/mm. The laboratory was uniformly seeded with 1-micron diameter droplets using a LaVision aerosol generator. A total of 2,100 images, corresponding to $\approx$ 157 rotor revolutions, were captured in frame-straddled mode at 460 frames per second using DaVis 10.1.2, and the δt was optimized for each case. Visual representations of the hardware used for PIV experiments are provided in Fig. 2.6.

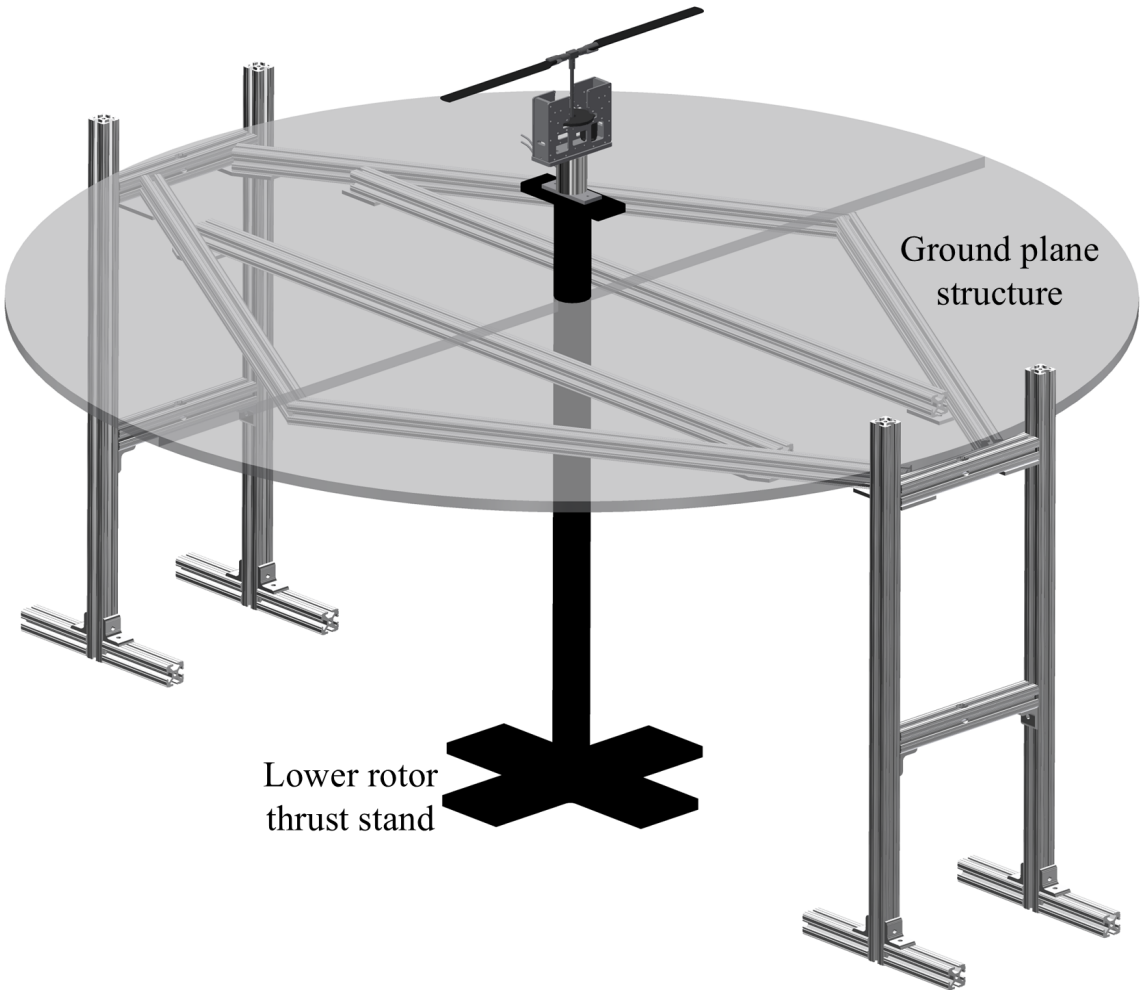

Figure 2.5: CAD representation of the lower rotor thrust stand and ground plane assembly.

Before processing, the rotor blades were masked to prevent spurious vectors at the rotor plane. Image pre-processing techniques were applied, including a sliding minimum intensity filter and sliding Gaussian smoothing, to remove background intensity and reduce image noise. Velocity vectors were calculated using a standard cross-correlation technique with an initial interrogation window size of 64×64 pixels at 50% overlap, followed by three passes with a 32×32 pixel window size at 75% overlap. Vectors with a peak ratio of less than two were discarded, and missing vectors were interpolated by averaging non-zero neighboring vectors. The final processed flow field contained 150,380 vectors with a spatial resolution of 0.58 mm covering a physical region of $0.297m \times 0.168m$ $(1.02R \times 0.58R)$ as displayed in Fig. 2.7.

Time-averaging of the post-processed vector field yielded the mean velocity field of the rotor system. This velocity field was subsequently used to extract the spanwise variation in

(a) Phantom VEO 4K 990 high-speed camera.

(b) Photonics dual head laser and controller.

(c) LaVision programmable timing unit (PTU X).

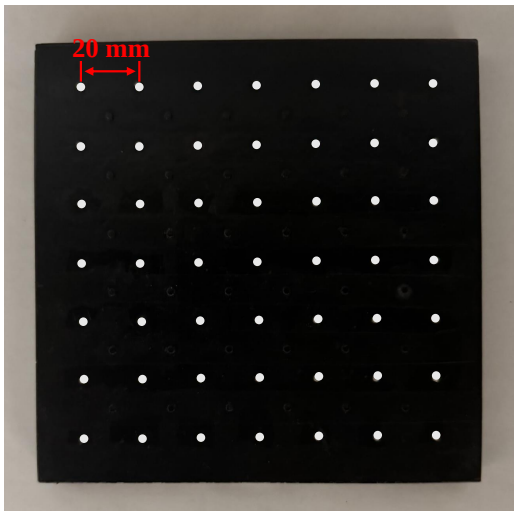

(d) Single-sided calibration target plate.

(e) LaVision aerosol generator.

Figure 2.6: Hardware used for the PIV experiments.

inflow, which is defined as the axial velocity experienced by the rotor at the rotor plane. However, due to the masking of the rotor plane, the axial velocity was extracted at 0.06R above and

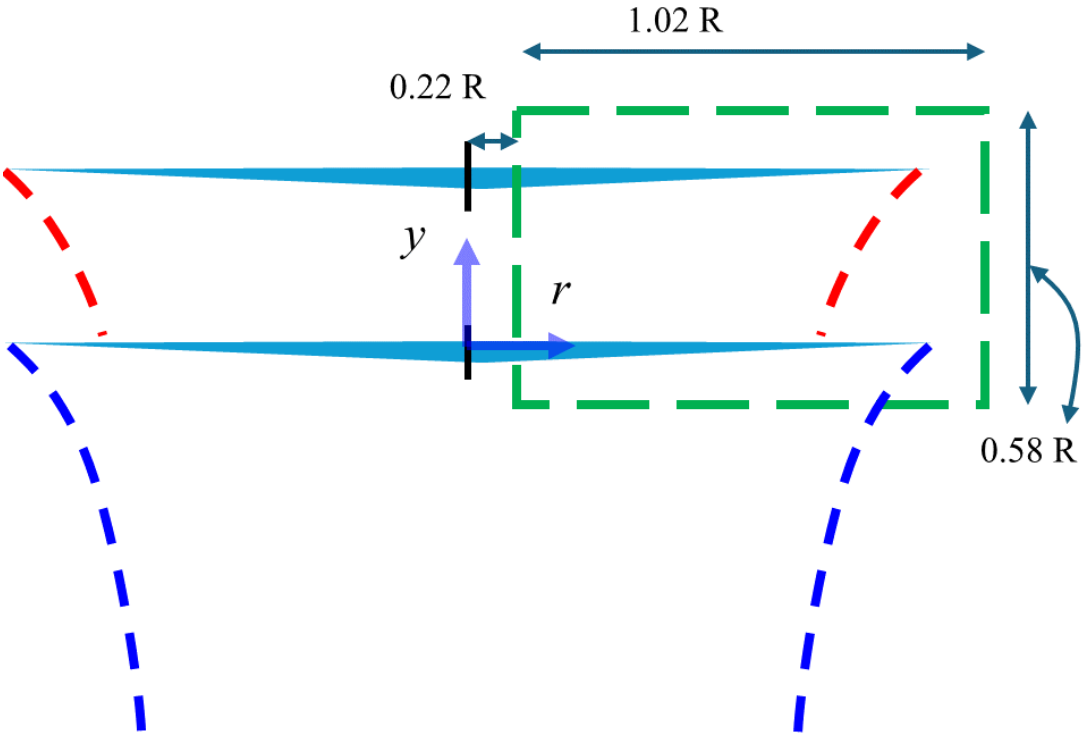

Figure 2.7: Schematic representation of the field-of-view used for PIV.

below the rotor plane and normalized by the rotor tip speed, ΩR. The inflow distribution was obtained by averaging the axial velocities at each radial location. The integrated inflow was then computed by integrating the elemental mass flow through the rotor disk, as described in Eq. 2.1.

$$\begin{gathered} \dot{m} = \int_0^R d\dot{m} \implies \rho A V = \int_0^R \rho V_y 2\pi x dx \quad \text{where} r = x/R \\ V = \frac{2}{R^2}\int_0^R V_y x dx; \quad \lambda = \frac{|V|}{\Omega R} \end{gathered} \tag{2.1}$$

2.4 Experimental conditions

The rotor performance was characterized at three constant chord-based tip Reynolds number, $Re_{tip} = 120,000; 86,500; 53,000$ (defined in Eq. 2.2, where ρ is the fluid density, ΩR is the tip velocity of the rotating blade, c is the blade chord length, and μ is the dynamic viscosity of the fluid medium). This corresponds to rotor speeds of $2060; 1495; 920$ RPM and tip Mach numbers $M_{tip} = 0.18; 0.13; 0.08$, respectively. This thesis primarily focuses on the $Re_{tip} = 120,000$ condition to quantify and understand the interactions of a coaxial rotor IGE. The lower

Reynolds number conditions are explored in Ch. 5 to assess how changes in Re_{tip} influence these interactions.

$$Re = \frac{\rho(\Omega R)c}{\mu} \equiv \frac{\text{inertial force}}{\text{viscous force}} \tag{2.2}$$

The inter-rotor spacing was varied between $d/R = 0.14 - 0.54$ to match the range where Ramasamy observed the most significant performance effects [5]. The rotor height above the ground was varied between $z/R = 0.4 - 2.4$ measured from the fixed lower rotor plane. The OGE condition was set at $z/R = 4.3$, where ground effect influences are observed to be negligible [10, 11].

The rotor thrust was altered during the experiment by varying the collective blade pitch angle, θ_0. For single rotor characterization experiments, the upper rotor was positioned at the $d/R = 0.54$ location. An extra z/R condition was also performed for the upper rotor, $z/R = 0$ (at the lower rotor plane), to fully characterize the performance. The coaxial rotor experiments were conducted at two trim conditions: 1). a constant total CCR thrust and 2). a torque-matched trim condition. Thrust conditions ranged from $C_{T,CCR} = 0$ to 0.0081, with torque balanced to within $\pm 2\%$ of the total system torque (see Eq. 2.3) [57]. The experimental test matrix for this thesis is summarized in Table 2.2.

$$\tau = \frac{|C_{Q_l}| - |C_{Q_u}|}{|C_{Q_l}| + |C_{Q_u}|} \tag{2.3}$$

Table 2.2: Summary of the parametric space for the experiments.

Parameter	Single Rotor	CCR
z/R	$(z/R)_l = 0.4 : 0.4 : 2.4,\ 4.3$ $(z/R)_u = 0.54 : 0.4 : 2.94,\ 4.84$	$(z/R)_l = 0.4 : 0.4 : 2.4,\ 4.3$
d/R	–	$0.14 : 0.1 : 0.54$
Operating Conditions	$\theta_0 = 0°$ to $8°$	$C_{T,CCR} =$ $(0 - 8.1) \times 10^{-3}$
Re_{tip}	$(53,\ 86.5,\ 120) \times 10^3$	$(53,\ 86.5,\ 120) \times 10^3$

The flow field experiments were conducted for the coaxial rotor at $C_T = 0.0081$ and torque-balanced conditions for rotor heights $z/R = 0.4, 1.6$ and OGE conditions. Flow field measurements were performed in the single rotors by maintaining the thrust and ground height the same as the individual rotors in coaxial configuration to isolate and understand the rotor-rotor interactions in the presence of ground. For the single rotor configuration, the FOV was modified to $0.84R \times 0.22R$ to better capture the flow field of the lower rotor in a single rotor configuration.

2.5 Performance metrics

In rotor performance analysis of this thesis, non-dimensional quantities were used to normalize the loads experienced for various rotor sizes and blade tip speeds. The thrust coefficient (C_T), and the power coefficient (C_P) are given by

$$C_T = \frac{T}{\rho A_d \Omega^2 R^2} \qquad C_P = \frac{P}{\rho A_d \Omega^3 R^3} \tag{2.4}$$

where T is the rotor thrust (N), P is the rotor power consumption (W), ρ is the fluid density (kg/m^3), A_d is the rotor disk area (m^2), Ω is the rotational speed of the rotor (rad/s), and R is the rotor radius (m). The rotor performance was quantified using an efficiency metric developed for a hovering rotor, termed the figure of merit (FM). The FM represents the ratio of the ideal power to the actual power required from experimentation, given by

$$FM = \frac{C_T^{3/2}}{\sqrt{2}\, C_P} \tag{2.5}$$

where C_T and C_P represent the measured thrust and power coefficients for a single rotor. The figure of merit definition for a CCR has been modified by Leishman [21] to account for the individual loads produced by each rotor of the system and given by

$$FM_{CCR} = \frac{C_{T_u}^{3/2} + C_{T_l}^{3/2}}{\sqrt{2}\,(C_{P_u} + C_{P_l})} \tag{2.6}$$

where the subscripts u and l denote the non-dimensionalized quantities of the upper and lower rotors, respectively.

Chapter 3

Theoretical Framework

A lifting rotor is a versatile machine, as it should be able to operate efficiently in hover, vertical climb and descent, and forward flight conditions. The aerodynamic characteristics of the rotor differ in each of these conditions, so its design must be considered for a wide range of operations. Because of the inherent aerodynamic complexity, obtaining accurate performance estimations in the design phase is often challenging. Over time, advancements in the understanding of rotor aerodynamics have led to a wide range of theoretical and experimental performance estimations, many having very high accuracy levels [58, 59, 60, 22].

3.1 Momentum theory

Throughout the evolution of rotor performance modeling and prediction tools, fundamental principles remain essential to provide accurate results with minimal computational requirements. Although several factors play a significant role in rotor physics, most notably within the wake and vortical structures, rotor performance can still be accurately analyzed using a simple approach known as the Rankine-Froude momentum theory. Also known as actuator disk theory, it was initially developed for marine propellers in the late 1800s and has since been adopted into the performance prediction of aircraft propellers, wind turbines, and helicopter rotors [61, 62, 63].

The actuator disk theory leverages the mass, momentum, and energy conservation laws of fluid mechanics to form relationships between the various performance characteristics of a rotor. The general flow model for momentum theory analysis of a hovering rotor is shown in

Fig. 3.1. It assumes the rotor plane to be an infinitesimally thin, solid disk supporting a pressure differential above and below it. In the actuator disk model, the rotation of the blades imparts energy into the surrounding air. Newton's third law states that an equal and opposite reaction occurs as an upwards-directed thrust. Imparting energy into the air requires a power input, and the work done to rotate the blades is known as the *induced power*. The induced power is an inevitable energy loss for a helicopter to maintain hover. Therefore, it represents the minimum power requirement, and often termed the ideal power [9, 64].

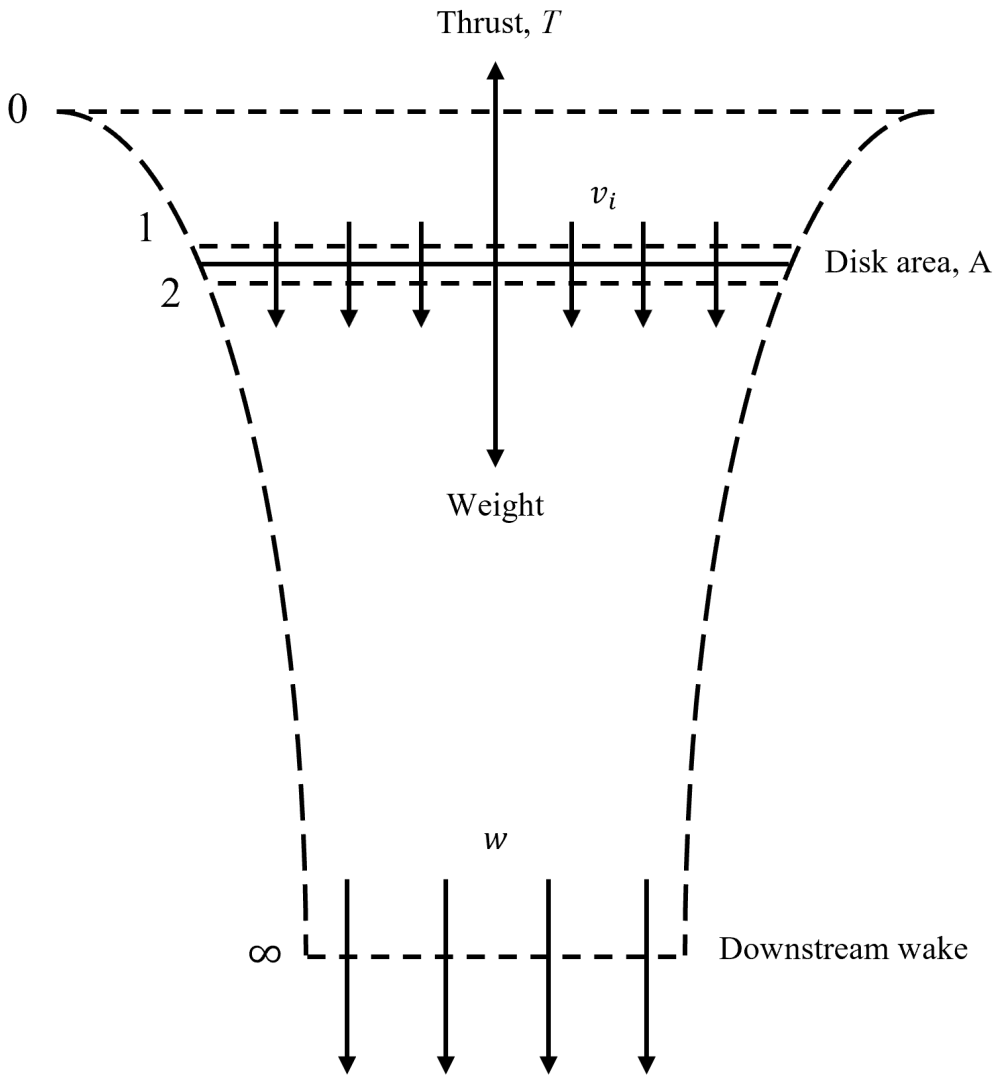

Figure 3.1: Momentum theory model for a hovering rotor [9].

In actuator disk theory, various assumptions are introduced to simplify the governing conservation equations. The flow into the rotor is assumed to be one-dimensional, incompressible, inviscid, and quasi-steady. A one-dimensional flow implies that the velocity entering the rotor

plane is axial, or perpendicular to the rotor plane. This assumption relaxes the non-ideal losses associated with tip effects, swirl effects, and spanwise flow. In an inviscid fluid, there is an absence of viscous shear between fluid elements, thereby eliminating viscous losses and leaving the induced losses as the only form of losses that require power to overcome. Incompressibility signifies a constant fluid density, and a quasi-steady flow implies that the fluid properties do not change with time. With these assumptions, the conservation laws of mass, momentum, and energy are expressed in their simplified forms as

$$\int\int_S \rho\vec{V}\cdot d\vec{S} = 0 \tag{3.1}$$

$$\int\int_S (\rho\vec{V}\cdot d\vec{S})\vec{V} = \vec{F} \tag{3.2}$$

$$\int\int_S \frac{1}{2}(\rho\vec{V}\cdot d\vec{S})|\vec{V}|^2 = W \tag{3.3}$$

where ρ is the fluid density, V is the fluid velocity, and dS is the unit normal area vector, which is defined to point out of the control volume.

In Fig. 3.1, cross-section 0 denotes an area parallel to the rotor plane, located far upstream, where the air is assumed to be quiescent in hover. Cross-sections 1 and 2 correspond to regions directly above and below the rotor plane, and cross-section ∞ depicts the far downstream wake. Between cross-sections 1 and 2, the pressure difference across the disk accelerates the fluid, generating a velocity of v_i. The wake is fully contracted at the far downstream location, known as the *vena contracta*. Here, the velocity is denoted by w.

Eqs. 3.1 to 3.3 can be applied to the actuator disk model to derive fundamental relationships between the rotor thrust, power, and induced velocity. Mass conservation states that the mass flow remains constant across the boundaries of a control surface. So, the mass flow across section 2 and the far wake are constant. Assuming 1D, incompressible flow, Eq. 3.1 can be integrated to

$$\dot{m} = \rho A v_i \tag{3.4}$$

where A represents the area of the rotor disk. The conservation of momentum establishes a relationship between the thrust produced by the rotor and the net time rate-of-change of the momentum into and out of the control volume. Given that the air is quiescent at section 0, Eq. 3.2 simplifies to

$$T = \dot{m}w \tag{3.5}$$

Finally, energy conservation states that the work done on the rotor equals the gain in kinetic energy of the air per unit time. The power consumed by the rotor is Tv_i, so Eq. 3.3 reduces to

$$Tv_i = \frac{1}{2}\dot{m}w^2 \tag{3.6}$$

These three equations can be manipulated to show that $T = 2\rho A v_i^2$ and $P = 2\rho A v_i^3$. So, the induced power scales with the cube of the induced velocity, therefore emphasizing the importance of minimizing the induced velocity in rotor design. This relationship highlights a fundamental issue with the CCR configuration, as the induced velocity of each rotor in the system is greater than that of an equivalent single rotor. As such, additional power requirements are incurred. For further derivation of the momentum theory in this chapter, the thrust and power are written in non-dimensional form for simplicity and denoted as C_T and C_P, respectively.

3.2 Baseline empirical power factor definitions

In the base derivation of momentum theory, the power described was the ideal induced power required for a lifting rotor to maintain hover. The actual total power required to hover can be split into two components, the profile power (C_{P_0}), and the induced power (C_{P_i}) as shown below:

$$C_P = C_{P_0} + C_{P_i} \tag{3.7}$$

For a hovering rotor, the profile power is assumed constant within pre-stall operating regimes and is determined by the blade's drag characteristics. The *ideal induced power* is a

function of the rotor thrust and is defined by momentum theory as $C_T^{3/2}/\sqrt{2}$. However, due to the conservative assumptions underlying momentum theory, the actual induced power required for a given thrust condition will be greater than the ideal prediction. To correct this error, a factor termed the *induced power factor*, κ_i, is introduced. The induced power factor can be experimentally quantified for a rotor, and it measures the effect of non-ideal losses, such as nonuniform inflow and tip losses, on the induced power required to hover. This factor quantifies the additional power requirement for an actual hovering rotor compared to one hovering under idealized conditions, and with a set of experimental measurements at various thrust conditions, κ_i is determined through a curve fit to Eq. 3.8.

$$C_P = C_{P_0} + \kappa_i \frac{C_T^{3/2}}{\sqrt{2}} \qquad \kappa_i = \frac{C_{Pi,exp}}{C_{Pi,ideal}} \tag{3.8}$$

A single rotor operating IGE benefits from a reduced inflow through the rotor. This benefit can be described through the *ground effect power factor*, κ_g as shown in Eq. 3.9, which quantifies the reduction in induced power required to hover IGE at a constant thrust compared to OGE conditions. In this formulation, κ_i is held constant from the OGE condition so that κ_g strictly determines the effect of the ground on the induced power.

$$C_P = C_{P_0} + \kappa_g \kappa_i \frac{C_T^{3/2}}{\sqrt{2}} \qquad \kappa_g = \frac{C_{Pi,exp,IGE}}{C_{Pi,exp,OGE}} \tag{3.9}$$

A CCR incurs additional losses, which can be quantified using three independent power factors. The overall interferences of the CCR system are represented by the *interference-induced power factor*, κ_{int}, which compares the power required by a CCR to the power required by two independent single rotors, each with half the solidity and thrust. To adjust for the difference in solidity, the induced power term is scaled by $1/\sqrt{2}$, as described by Leishman [21]. Furthermore, two *individual rotor influence factors* can be defined as $\kappa_{u|l}$, where κ_u accounts for the external influences of the lower rotor on the upper rotor's performance, and κ_l accounts for the influences of the upper rotor on the lower rotor's performance. Both factors compare the power required of the respective individual rotor in the CCR system to that of a single rotor at the same thrust, as denoted in Eq. 3.10.

$$
\begin{aligned}
C_{P,CCR} &= C_{P_0} + \kappa_{int}\frac{\kappa_i}{\sqrt{2}}\frac{C_{T,CCR}^{3/2}}{\sqrt{2}} \qquad & \kappa_{int} &= \frac{C_{Pi,exp,CCR}}{2 \cdot C_{Pi,exp,SR}} \\
C_{P,u|l} &= C_{P_0} + \kappa_{u|l}\kappa_i\frac{C_{T,u|l}^{3/2}}{\sqrt{2}} \qquad & \kappa_{u|l} &= \frac{C_{Pi,exp,u|l}}{C_{Pi,exp,SR}}
\end{aligned}
\tag{3.10}
$$

Each empirical factor defined in Eqs. 3.8 to 3.10 were experimentally computed using the present rotor facility (described in Sec. 2.1) and serve as a baseline for the empirical factors that are derived in Section 3.3. For the CCR IGE, the baseline factors are held constant, ensuring that the new factor accounts for changes specific to the unique operating condition. Their computation is presented in the beginning sections of Ch. 4. Additionally, intriguing trends were observed for these power factors for various rotor rotational speeds, which are presented and discussed in Chapter 5.

3.3 CCR IGE empirical power factor definitions

A CCR operating near the ground introduces many new complexities, as the performance detriments due to the rotor-rotor interactions compete with the favorable effects of rotor-ground interactions. Therefore, the factors introduced in Section 3.2 are inadequate to describe the performance characteristics, and new factors must be developed. The competing effects are inherently nonlinear, as each interaction continuously influences and modifies the other. Consequently, a complete decoupling of these interactions is not feasible with the current understanding of the aerodynamic interactions at play. However, a set of empirical power factors can be established to quantify the net ground effect experienced by the CCR, as well as how the rotor-rotor interactions are modified in the presence of the ground.

To quantify the ground effect on a hovering single rotor, its required power near-ground is compared to its required power out-of-ground for a constant thrust. This method can be applied similarly to a CCR. Consider a CCR hovering in OGE conditions and begins slowly approaching the ground. Before approaching the ground, the rotor-rotor interactions are at an equilibrium state, and rotor-ground interactions are absent. As the rotor system begins to move closer to the ground, rotor-ground interactions arise, influencing the performance characteristics of each rotor. Consequently, the rotor-rotor interactions are modified. Thus, when

comparing the performance of a CCR IGE to that of a CCR OGE, a *net ground effect* can be quantified; however, the rotor-rotor interactions cannot be decoupled from the ground effect. This interplay becomes apparent in Sec. 4.2. The power factors used to describe the net ground effect of the CCR IGE are presented in Eq. 3.11.

$$\begin{aligned} C_{P,CCR} &= C_{P_0} + (\boldsymbol{\kappa_g})_{\boldsymbol{int}} \kappa_{int} \frac{\kappa_i}{\sqrt{2}} \frac{C_{T,CCR}^{3/2}}{\sqrt{2}} \qquad & \kappa_{g,int} &= \frac{C_{Pi,exp,CCR,IGE}}{C_{Pi,exp,CCR,OGE}} \\ C_{P,u|l} &= C_{P_0} + (\boldsymbol{\kappa_g})_{\boldsymbol{u|l}} \kappa_{u|l} \kappa_i \frac{C_{T,u|l}^{3/2}}{\sqrt{2}} \qquad & \kappa_{g,u|l} &= \frac{C_{Pi,exp,u|l,IGE}}{C_{Pi,exp,u|l,OGE}} \end{aligned} \tag{3.11}$$

The factors described above are analogous to the single rotor ground effect factor κ_g, derived from analyzing the performance benefit for a single rotor due to operation in the proximity of a ground surface, and defined as the reduction in power for a rotor IGE compared to the power OGE. However, in a CCR, this relation is coupled to the rotor-rotor interactions. Consequently, additional empirical power factors are required to characterize the rotor-rotor interactions in the presence of the ground.

To assess the changes in rotor-rotor interactions of the CCR IGE, the power factors defined in Eq. 3.11 can be modified by dividing by the single rotor ground effect factor κ_g. By doing so, the deviations between the power factors are attributed to the rotor-rotor interactions of the CCR. This ratio isolates the ground interaction felt by the CCR from that experienced by the single rotor. Mathematically, this process begins with Eq. 3.11 and incorporates κ_g.

$$\begin{aligned} C_{P,CCR} &= C_{P_0} + \kappa_g \frac{(\boldsymbol{\kappa_g})_{\boldsymbol{int}}}{\boldsymbol{\kappa_g}} \kappa_{int} \frac{\kappa_i}{\sqrt{2}} \frac{C_{T,CCR}^{3/2}}{\sqrt{2}} \\ C_{P,u|l} &= C_{P_0} + \kappa_g \frac{(\boldsymbol{\kappa_g})_{\boldsymbol{u|l}}}{\boldsymbol{\kappa_g}} \kappa_{u|l} \kappa_i \frac{C_{T,u|l}^{3/2}}{\sqrt{2}} \end{aligned} \tag{3.12}$$

Physically, these ratios between the ground effect of the CCR and single rotor describe the performance changes of the CCR IGE compared to the performance of the single rotor at the same ground height. This can be shown by analyzing the power ratios that have been defined for each empirical factor:

$$\frac{(\kappa_g)_{int}}{\kappa_g} = \frac{\dfrac{C_{P_{i,CCR,IGE}}}{C_{P_{i,CCR,OGE}}}}{\dfrac{C_{P_{i,SR,IGE}}}{C_{P_{i,SR,OGE}}}} = \frac{\dfrac{C_{P_{i,CCR,IGE}}}{2 \cdot C_{P_{i,SR,IGE}}}}{\kappa_{int}}$$
$$\frac{(\kappa_g)_{u|l}}{\kappa_g} = \frac{\dfrac{C_{P_{i,u|l,IGE}}}{C_{P_{i,u|l,OGE}}}}{\dfrac{C_{P_{i,SR,IGE}}}{C_{P_{i,SR,OGE}}}} = \frac{\dfrac{C_{P_{i,u|l,IGE}}}{C_{P_{i,SR,IGE}}}}{\kappa_{u|l}} \tag{3.13}$$

These expressions $(\kappa_g)_{int}/\kappa_g$ and $(\kappa_g)_{u|l}/\kappa_g$ quantify the changes in interactional effects for the CCR as it transitions from OGE to IGE operating conditions. Furthermore, the right-hand side of Eq. 3.13 introduces a third ratio that describes the rotor-rotor interactions in the presence of the ground, as it compares the induced power required for the CCR to operate at a specific IGE condition to that of a single rotor at the same IGE condition.

From this derivation, three sets of empirical power factors have been introduced and are summarized in Eqs. 3.14 and 3.15. Each of these power factors describes a different aspect of the performance of a CCR IGE:

1. $(\kappa_g)_{int}$ & $(\kappa_g)_{u|l}$: The net ground effect experienced by the CCR.

2. $(\kappa_{int})_g$ & $(\kappa_{u|l})_g$: The rotor-rotor interactions of the CCR in the presence of the ground.

3. $(\kappa_{int})_g/\kappa_{int}$&$(\kappa_{u|l})_g/\kappa_{u|l}$: How the rotor-rotor interactions of the CCR IGE vary compared to the rotor-rotor interactions in OGE conditions.

$$(\kappa_g)_{int} = \frac{C_{P_{i,CCR,IGE}}}{C_{P_{i,CCR,OGE}}}; \quad (\kappa_{int})_g = \frac{C_{P_{i,CCR,IGE}}}{2 \cdot C_{P_{i,SR,IGE}}}; \quad \frac{(\kappa_{int})_g}{\kappa_{int}} = \frac{\dfrac{C_{P_{i,CCR,IGE}}}{2 \cdot C_{P_{i,SR,IGE}}}}{\dfrac{C_{P_{i,CCR,OGE}}}{2 \cdot C_{P_{i,SR,OGE}}}} \tag{3.14}$$

$$(\kappa_g)_{u|l} = \frac{C_{P_{i,u|l,IGE}}}{C_{P_{i,u|l,OGE}}}; \quad (\kappa_{u|l})_g = \frac{C_{P_{i,u|l,IGE}}}{C_{P_{i,SR,IGE}}}; \quad \frac{(\kappa_{u|l})_g}{\kappa_{u|l}} = \frac{\dfrac{C_{P_{i,u|l,IGE}}}{C_{P_{i,SR,IGE}}}}{\dfrac{C_{P_{i,u|l,OGE}}}{C_{P_{i,SR,OGE}}}} \tag{3.15}$$

These factors decompose the coupled interactional effects into components so that the competing effects of the rotor-ground and rotor-rotor interactions can be assessed separately. Each of these factors can be empirically computed from the same data set, and the definition of each factor provides a different angle into the interactional effects on the rotor power of a CCR IGE.

Each empirical factor derived in this section has an associated uncertainty, and the uncertainty propagates as factors are multiplied together. The method used to compute the total uncertainty of each factor is provided in appendix A. For clarity, error bars for each empirical factor were omitted in the figures; however, the propagated uncertainties for the factors were calculated, and the corresponding total 95% uncertainty bounds are provided in the respective figure captions.

Chapter 4

Quantification of the aerodynamic interactions of a hovering coaxial rotor system

The previous chapter established a set of empirical correction factors that characterize the interactions experienced by single and coaxial rotor systems operating in and out-of-ground effects. This chapter quantifies these factors through experimental analysis to determine the influence of the rotor-rotor and rotor-ground interactions on the induced power of the CCR IGE. To assess the performance of the coaxial rotor operating IGE, the baseline factors presented in Section 3.2 are quantified first. The chapter commences with single rotor performance characterization in OGE conditions, then moves to the IGE condition. Next, the rotor-rotor interactions of the CCR OGE are quantified. Once the baseline factors have been established for the experimental facility, the chapter transitions to the performance analysis of the CCR IGE, where most of the novel discussion lies.

4.1 Baseline performance characterization

4.1.1 Single rotor

Before quantification of the induced power factors, it was necessary to determine the stall point of the rotor to ensure operation in a constant profile power regime. The stall point of the rotor was characterized by computing the figure of merit from Eq. 2.5 to locate the maximum FM, which corresponds to the highest aerodynamic efficiency of the rotor. As shown in Fig. 4.1, the stall point was identified at a blade loading coefficient of $C_T/\sigma \approx 0.12$, indicating the threshold around which the profile drag drastically increased.

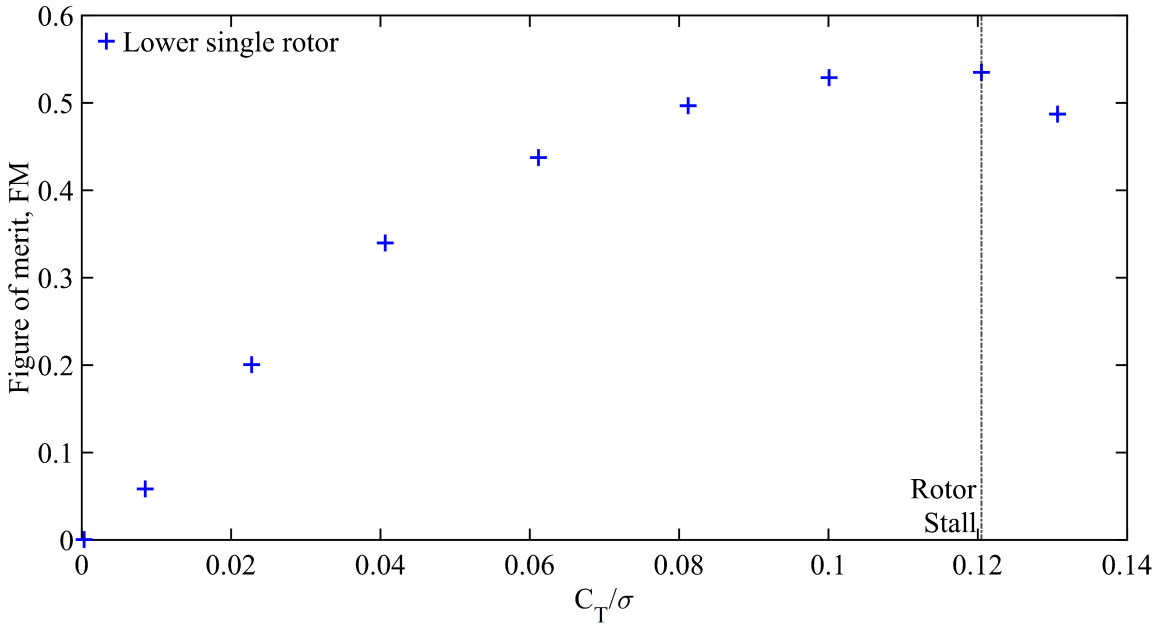

Figure 4.1: Rotor performance characterization for the lower single rotor hovering out-of-ground effect.

Section 3.2 introduced two empirical factor definitions to evaluate the induced power of a single rotor operating in various conditions: the non-ideal losses OGE (κ_i) and the ground effect (κ_g). The non-ideal losses are quantified in Fig. 4.2. For this experiment, the facility was arranged with a single rotor mounted to the thrust stand. It was operated in thrust regimes where $C_T/\sigma \leq 0.08$, which falls well below the stall regime identified in Fig. 4.1, thus ensuring operation in a constant profile power regime. To determine κ_i, a curve fit was made to the experimental data using Eq. 3.8. The non-ideal losses were measured to be 1.51 for the lower rotor, indicating that the power required from the experiment is 51% greater than the theoretical prediction due to the non-ideal losses neglected by momentum theory. Table 4.1 summarizes the non-ideal losses of the upper and lower single rotors, along with their associated uncertainties.

Table 4.1: Single rotor induced power factor

Configuration	κ_i
Upper rotor	1.53 ± 0.020
Lower rotor	1.51 ± 0.020

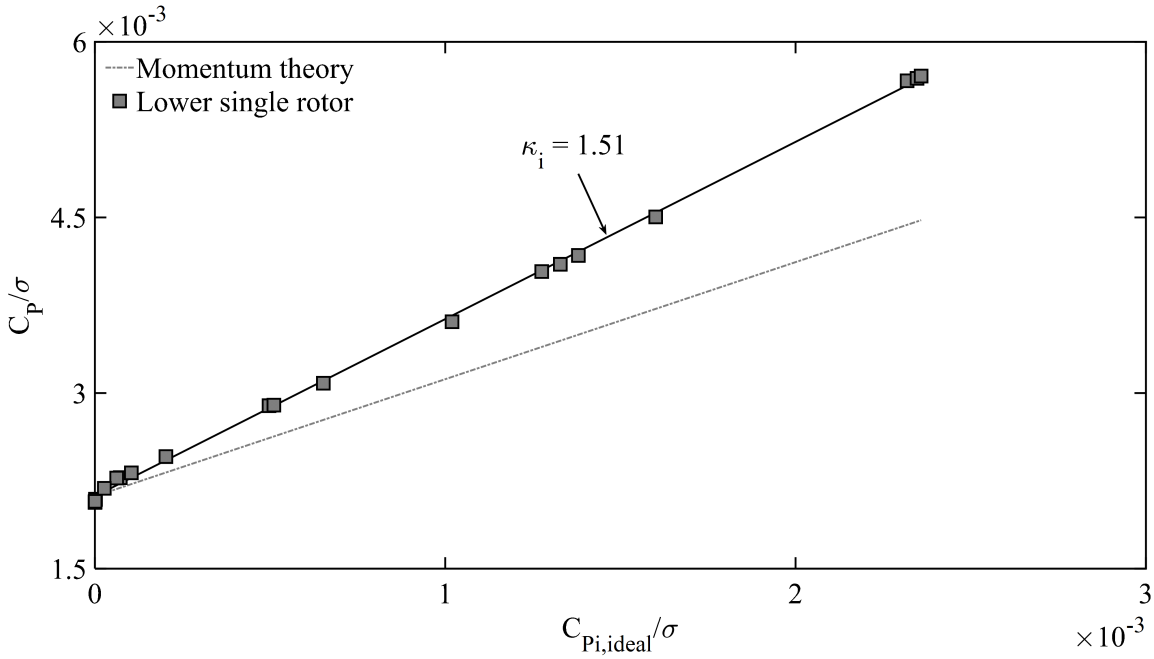

Figure 4.2: Non-ideal induced power factor for the lower single rotor hovering out-of-ground effect.

The ground effect on the rotor operating IGE was quantified similarly, assuming κ_i remained constant so that any variations in the measured induced power could be attributed solely to the rotor's proximity to the ground surface. An example is shown in Fig. 4.3 for $z/R = 0.4$, where an apparent reduction in power required for a given thrust is observed compared to the single rotor OGE. The ground effect factor for the upper and lower rotor was quantified across a range of z/R conditions, as presented in Fig. 4.4. Because the upper rotor adjusts to alter the d/R conditions in the CCR, the upper rotor's ground height spans across many more conditions than shown while operating in the CCR configuration. To preserve the appropriate ground effect factor for future CCR IGE analysis without performing upwards of 200 different IGE condition experiments, a fourth-order polynomial fit was performed on the upper rotor experimental data in Fig. 4.4.

In the single rotor, the non-ideal induced power factor $(\kappa_i > 1)$ indicates that the experimentally measured induced power exceeds the predictions of momentum theory. Conversely, the ground effect factor $(\kappa_g < 1)$ suggests that the induced power decreases when the rotor operates IGE. Since κ_g is defined relative to the power required OGE, it only implies

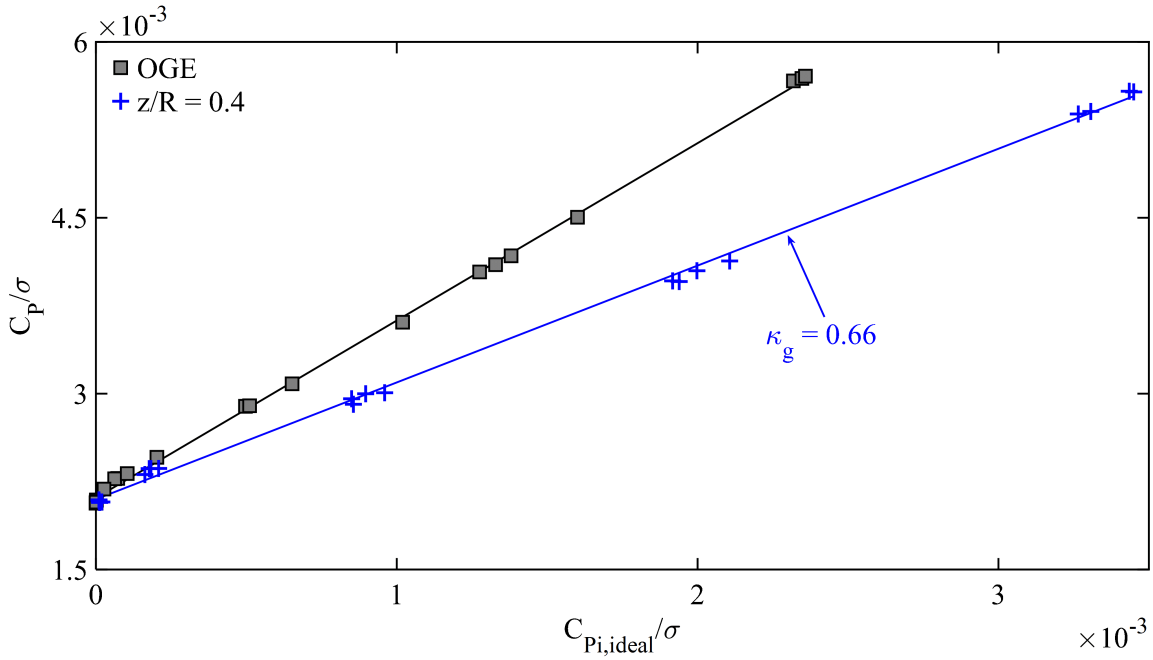

Figure 4.3: Ground effect factor for the lower single rotor hovering at $z/R = 0.4$.

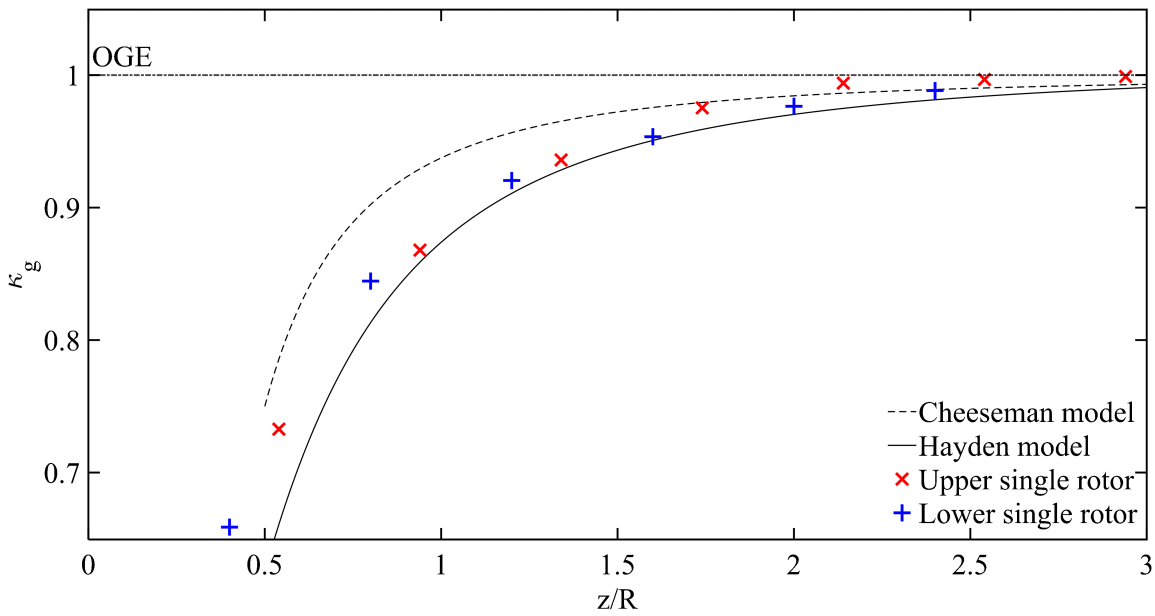

Figure 4.4: Characterization of the ground effect factor for the single upper and lower rotor across a range of in-ground effect conditions. Compared with semi-empirical models by Cheeseman and Hayden [10, 11]. The total 95% confidence bound for each κ_g factor is within ± 0.040.

that the power required to hover IGE is less than OGE; however, in very extreme IGE conditions ($z/R < 0.5$), the power in experimentation may fall below the ideal momentum theory prediction.

4.1.2 Coaxial rotor hovering out-of-ground effect

With the baseline single rotor parameters quantified across all operating conditions, the facility was reconfigured to the CCR configuration in OGE conditions. Before quantifying the rotor-rotor interactional effects on the induced power, the figure of merit was computed from the measured thrust and power consumption to characterize the rotor performance (Eq. 2.6), shown in Fig. 4.5. As observed, the overall FM of the CCR operating at $C_{T,CCR}/\sigma = 0.13$ was less than that of the single rotor due to aerodynamic losses associated with the close proximity of the two rotors in operation. Furthermore, the efficiency of the lower rotor was significantly degraded compared to the upper rotor. This reduction arises because a large portion of the rotor is effectively in a climb condition, as the upper rotor's wake impinges directly on it, resulting in a substantial increase in the inflow angle, ϕ, thereby degrading its performance.

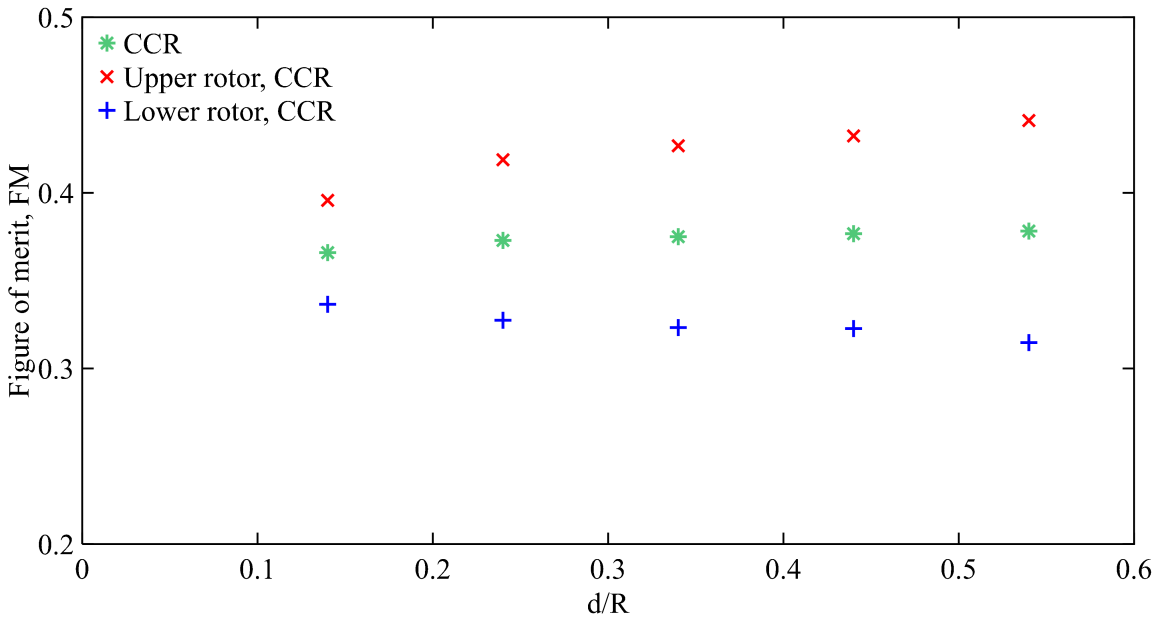

Figure 4.5: Rotor efficiency for the CCR hovering out-of-ground effect across the d/R spectrum of the present study for $C_{T,CCR}/\sigma = 0.13$.

The interference and influence factors for a CCR OGE were determined in a method analogous to the single rotor power factors, as illustrated in Figs. 4.6 and 4.7. For an inter-rotor spacing of $d/R = 0.34$, the interference factor was measured to be 1.28, indicating that a 28% more induced power is required for the CCR configuration compared to two single rotors, each with half the solidity of the CCR system. At the same d/R condition, the influences of the

upper rotor on the lower rotor resulted in a 50% increase in the lower rotor's induced power relative to a single rotor operating in isolation. Conversely, the influence of the lower rotor on the upper rotor resulted in an extra 11% induced power for the upper rotor.

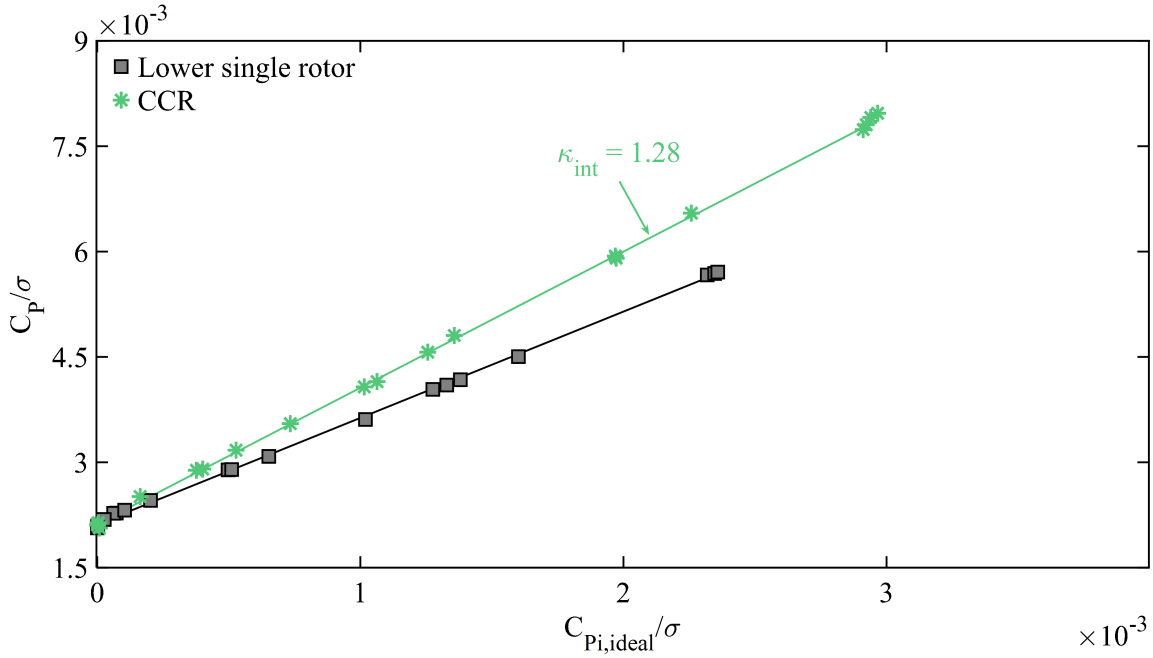

Figure 4.6: Interference factor for a CCR with $d/R = 0.34$ hovering out-of-ground effect.

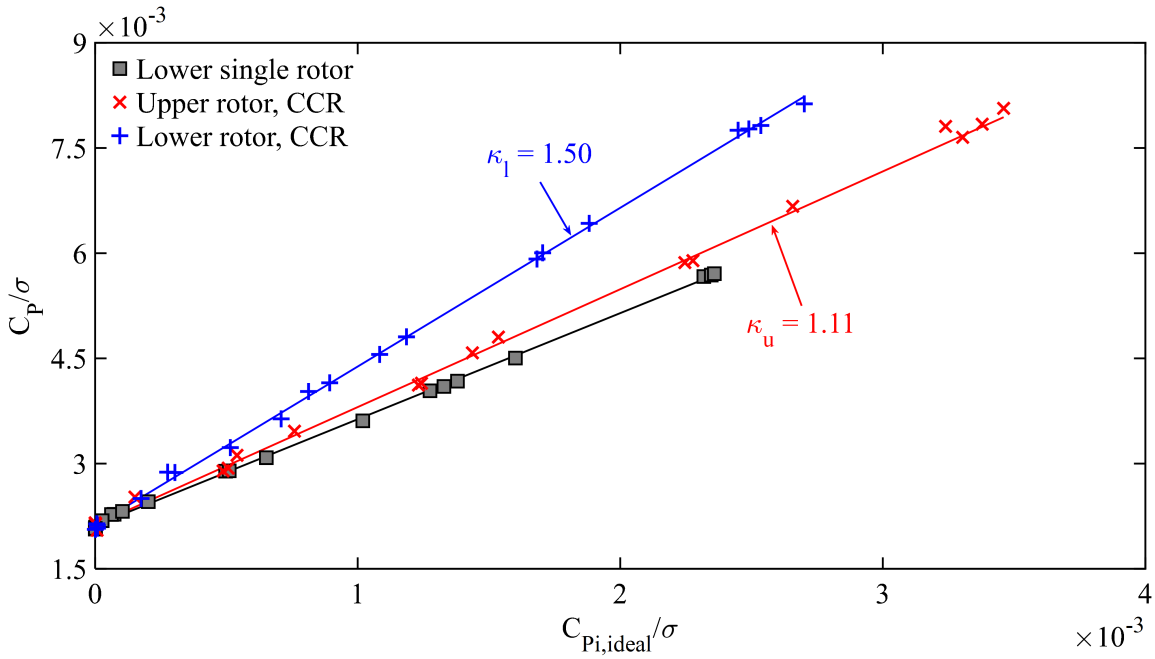

Figure 4.7: Influence factors of the upper and lower rotors in CCR configuration at $d/R = 0.34$ hovering out-of-ground effect.

The rotor-rotor interactions depend on the inter-rotor spacing, as noted previously [19, 20, 5]. The aerodynamic interactions are primarily governed by two mechanisms: induced tip vortex effects of each rotor influencing the proximal rotor, as described by the Biot-Savart law, and the direct impingement of the contracting wake from the upper rotor onto the lower rotor's plane.

At smaller inter-rotor spacings ($d/R \lesssim 0.3$), the induced flow from the lower rotor has a higher impact on the upper rotor, while the upper rotor wake has not fully developed, resulting in a reduced impact on the performance of the lower rotor. Conversely, at larger inter-rotor spacings ($d/R \gtrsim 0.3$), the lower rotor induced effects on the upper rotor diminish, while the upper rotor wake has contracted and impinges on the lower rotor with a higher velocity, leading to more substantial aerodynamic losses.

As a result, the performance of the upper rotor is expected to degrade as the rotors are brought closer together while the lower rotor performance improves. The results of the present study are shown in Fig. 4.8 and are consistent with expectations. Specifically, the sharp decline in upper rotor performance at smaller inter-rotor spacings contributes to an overall aerodynamic interference increase of the CCR by $\sim 4\%$ compared to the large spacings.

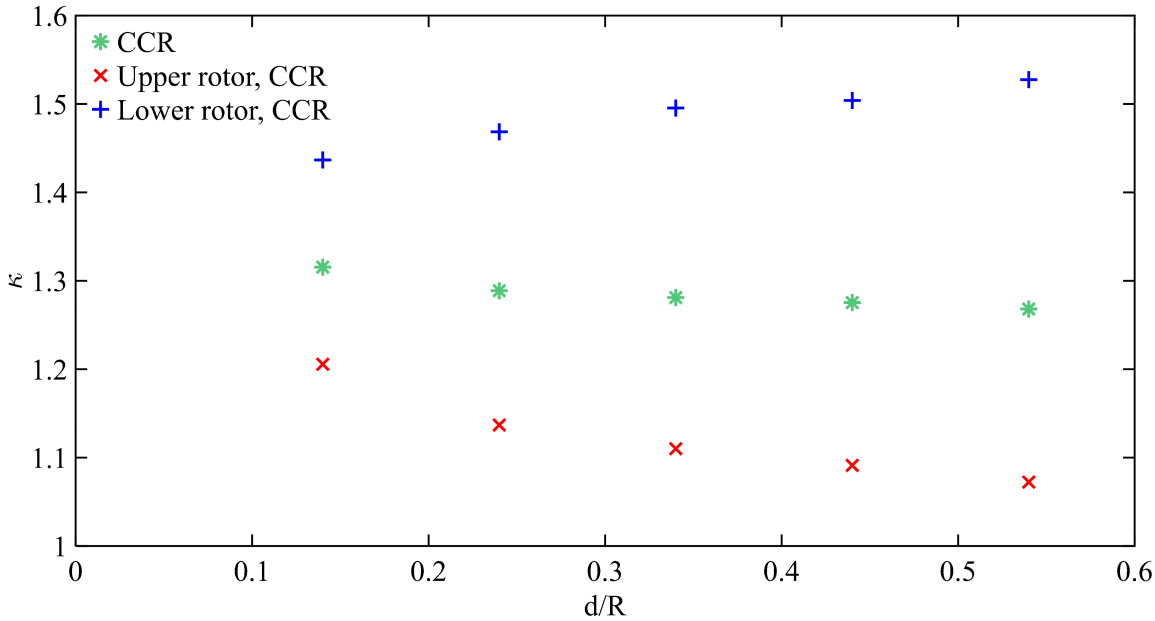

Figure 4.8: Interferences of the CCR hovering out-of-ground effect across the d/R spectrum of the present study. The total 95% confidence bound for each κ factor is within ± 0.045.

The power correction factors computed thus far align with established findings in literature [5, 11, 21]. However, it was necessary to quantify them for the current experimental facility as a baseline for the CCR IGE condition. The following section provides the performance analysis of the CCR IGE condition, where these baseline factors are referenced in the appropriate CCR IGE equations outlined in Sect. 3.3. These factors provide a foundation for comparison and further analysis of rotor performance near the ground.

4.2 Coaxial rotor hovering in-ground effect

4.2.1 Rotor-ground interactions

The empirical factors $(\kappa_g)_{int}$ and $(\kappa_g)_{u|l}$ were introduced to characterize the net rotor-ground interactions of the CCR IGE. The factors are defined relative to the OGE power of the CCR, analogous to the κ_g parameter for a single rotor to compare the power requirements of IGE versus OGE. As the rotor-rotor interactions are modified when the CCR operates near the ground, these factors provide a quantitative measure of the *net* rotor-ground interactions. The impact of varying z/R and d/R is evaluated to capture the interactional dynamics experienced by both rotors across the entire parametric space of this study. The influence of ground proximity is first examined to provide a comprehensive overview of its effect on CCR performance; then, the individual rotors are analyzed to offer deeper insight into their specific performance behavior.

CCR performance: The net rotor-ground interactions of the CCR IGE across various z/R conditions are presented in Fig. 4.9a. For reference, the single rotor models established by Cheeseman and Hayden are included to benchmark the CCR performance [10, 11]. Overall, the CCR performance aligned with the single rotor predictions, consistent with observations in prior studies [45]. However, minor discrepancies arose, particularly within the $1.0 \leq z/R \leq 2.5$ range, where the model underestimated the performance gains due to the ground, especially at larger d/R conditions. These non-linear trends suggest evolving rotor-rotor interactions. Fig. 4.10a provides the variation in performance concerning the inter-rotor spacing. The rotor-ground interactions show minimal sensitivity across the parametric space, suggesting that the ground predominantly governs the performance characteristics.

While the net ground effect experienced by the CCR was generally comparable to that of a single rotor, subtle anomalies indicated the presence of rotor-rotor interactions. These interactions were further investigated by analyzing the ground effect experienced by the individual rotors of the system.

Individual rotor performance: The net rotor-ground interactions of the upper and lower rotor as a function of z/R are depicted in Fig. 4.9b,c, respectively. For reference, single rotor models are again employed, alongside the experimental results for the single rotor IGE from Fig. 4.4. The upper rotor interactions revealed a stark deviation from the single rotor, where the ground effect experienced by the upper rotor in the CCR configuration was greater than that of the single rotor configuration for all ground heights. Conversely, the lower rotor in CCR experienced reduced net ground effect, particularly in conditions where $z/R < 1.0$. These findings suggest that the rotor-rotor interactions are modified in the presence of the ground, and they appear to favor the upper rotor.

Figure 4.10b,c illustrates the ground effect experienced by the upper and lower rotor as the inter-rotor spacing varies. For large z/R conditions, the ground effect remained approximately constant; however, notable variations occurred as the rotors approached the ground. In the experimental facility, the lower rotor's height above the ground remained fixed across all inter-rotor spacings, while increasing d/R elevated the upper rotor's ground height. Consequently, the net ground effect of the upper rotor should diminish as d/R increases at a constant ground height. And, the lower rotor's ground interactions should remain largely unaffected by changes in d/R. Nevertheless, the data revealed a reduction of $\sim 5\%$ in the ground effect experienced by the lower rotor as d/R increases.

The analysis of the net ground effect experienced by the upper and lower rotors of a CCR operating IGE revealed intriguing behavior. Significant deviations from single rotor IGE performance were observed, particularly as the system approached the ground. However, these variations effectively negated each other, as the reduction in power for the CCR IGE is similar to that for a single rotor IGE. This behavior highlights that the presence of the ground highly influenced the rotor-rotor interactions, and further analysis is needed to quantify these complex interactions.

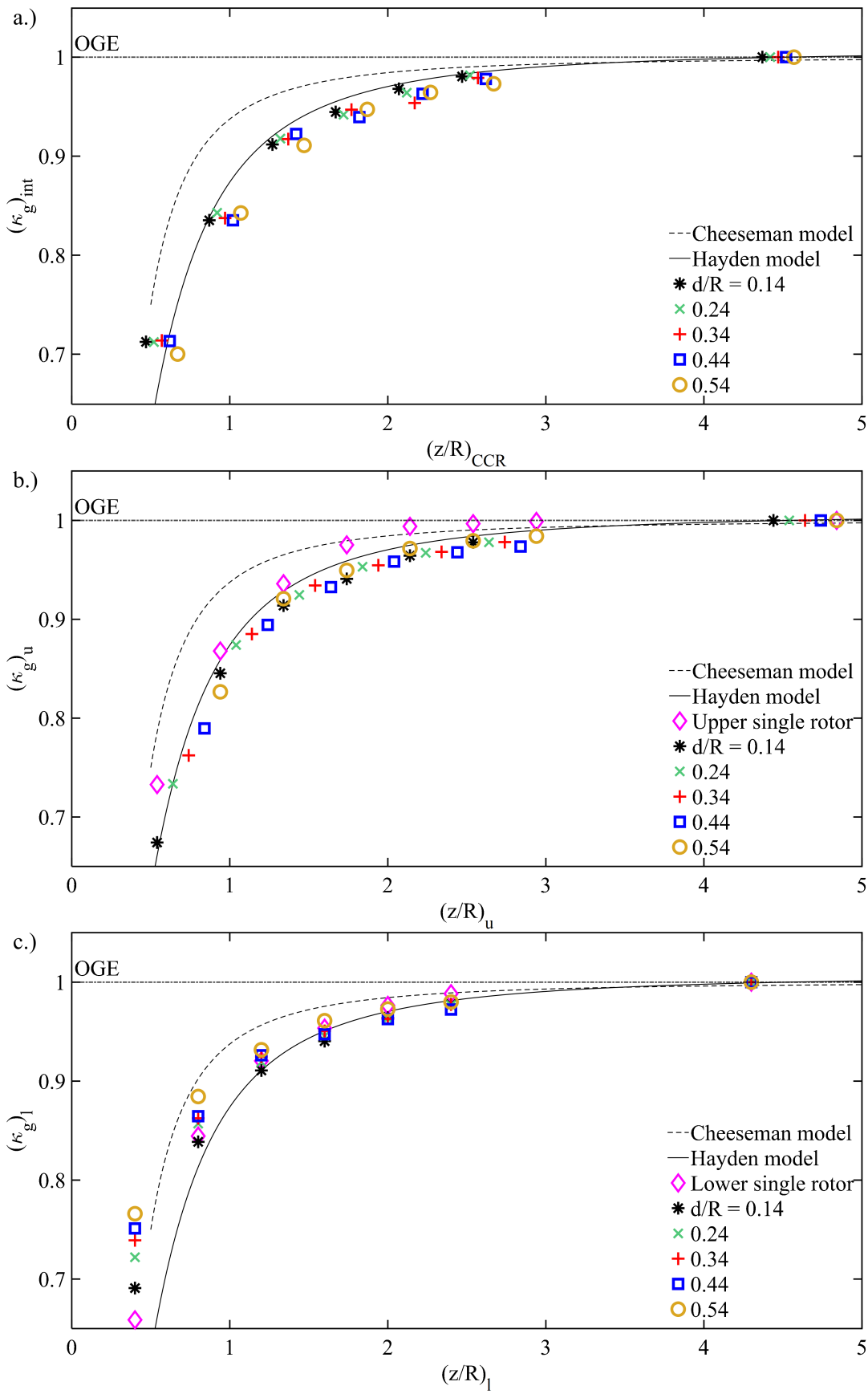

Figure 4.9: Effect of z/R on the net rotor-ground interactions of the CCR operating in IGE conditions. The total 95% confidence bound for each $(\kappa_g)_{CCR}$ factor is within ± 0.085.

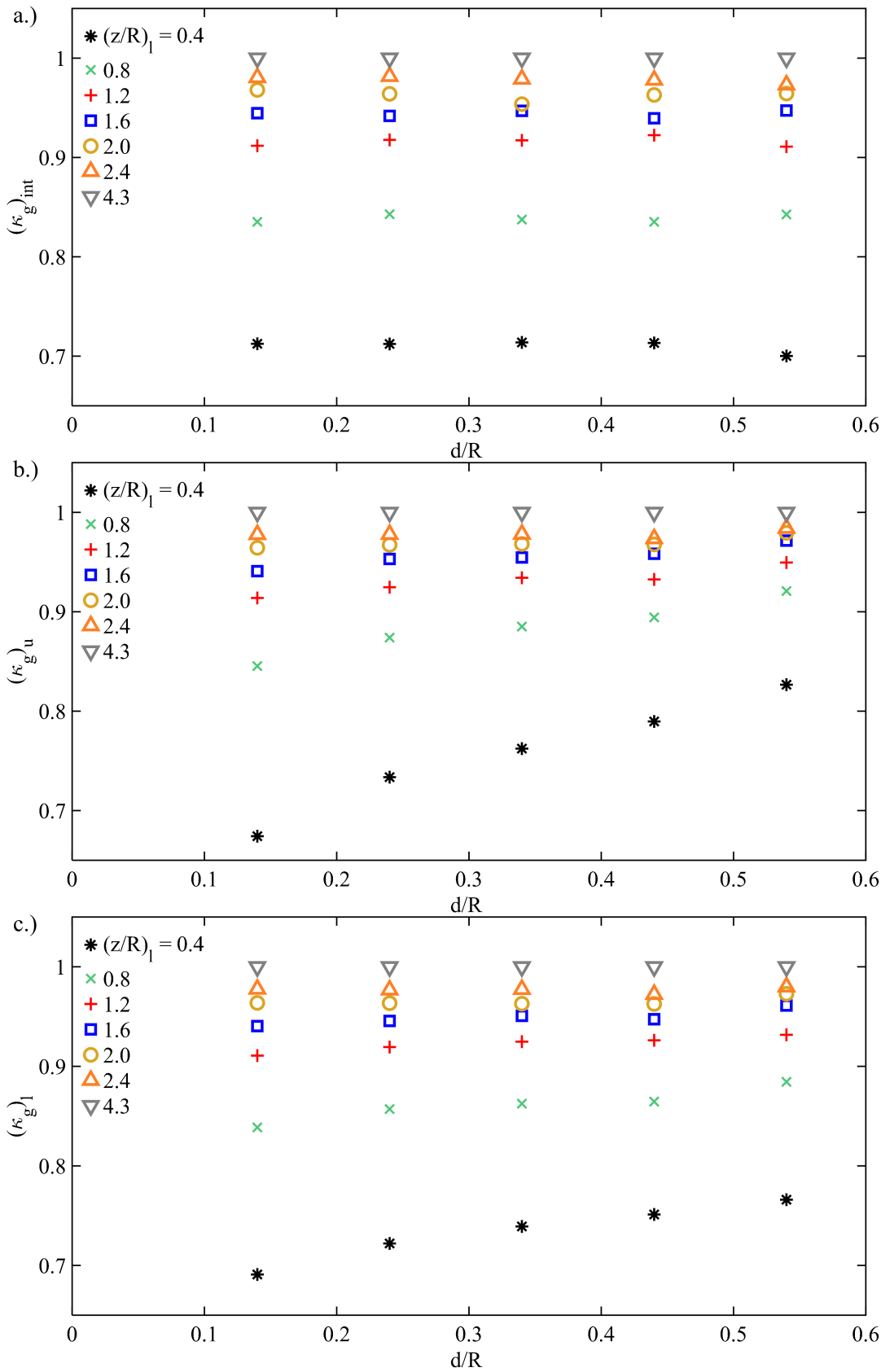

Figure 4.10: Effect of d/R on the net rotor-ground interactions of the CCR operating in IGE conditions.The total 95% confidence bound for each $(\kappa_g)_{CCR}$ factor is within ± 0.085.

4.2.2 Rotor-rotor interactions

The empirical factors $(\kappa_{int})_g$ and $(\kappa_{u|l})_g$ were established to isolate the rotor-rotor interactions from the net rotor-ground interactions previously quantified. These factors are analogous to κ_{int} and $\kappa_{u|l}$ for the OGE condition, which compares the CCR performance to that of a single rotor with equivalent solidity. For the in-ground analysis, the CCR is compared to a single rotor at the same IGE condition. Therefore, these factors assess the rotor-rotor interactions in the presence of the ground. The interactions are mapped across the entire parametric space of this study to elucidate the interactional behavior between the rotors. As with the rotor-ground interaction analysis, the CCR performance is presented first to provide a holistic view of the interactional effects on the system, followed by an analysis of the individual rotor performances.

CCR performance: The rotor-rotor interactions of the CCR in the presence of the ground are depicted in Fig. 4.11a. As the system entered IGE conditions, the rotor-rotor interferences slightly diminished from OGE conditions and reached a minimum when $(z/R)_{CCR} \approx 2.0$. As the rotor system approached the ground, the interference increased again, and peaked at the nearest ground height. This trend was consistent across all inter-rotor spacings, as illustrated in Fig. 4.12a. The observed behavior indicated that the ground influences the rotor-rotor interactions across all IGE conditions. To investigate the source of these interferences further, the rotor-rotor influences of the upper and lower rotors were analyzed to determine how the ground modifies the interactions between the rotors.

Individual rotor performance: The variation in rotor-rotor interactions for the upper and lower rotors across the range of z/R conditions is presented in Figs. 4.11b,c. The upper rotor's interactions exhibited a systematic trend for all d/R, and showed a reduction in interference under the most extreme IGE conditions compared to OGE. This suggested a reduction in the influence of the lower rotor on the upper rotor as the ground height reduced. This behavior is intuitive, as the inflow of the lower rotor highly reduces in the presence of the ground, reducing the negative interactions it imposes on the upper rotor.

Across the z/R spectrum, the reduction in influences followed a non-monotonic pattern: as the CCR enters IGE conditions, $(\kappa_u)_g$ reduced until $(z/R)_u \approx 2.0$, then increased until

$(z/R)_u \approx 0.8$, before sharply decreasing again at the closest ground proximity. These non-linear trends suggested a complex interplay between the rotor-ground and rotor-rotor interactions, where competing effects led to non-monotonic performance fluctuations in the upper rotor's performance.

The performance improvement of one rotor due to the ground typically has an adverse effect on the other rotor, as previously noted [5, 45]. Figure 4.11c aligns with these observations, showing a significant increase in $(\kappa_l)_g$ under the most extreme ground condition. At this point, the upper rotor wake experiences less wake contraction due to the ground and impinges on a larger area of the lower rotor, resulting in performance degradation. The physics behind this behavior are discussed in further detail later in this chapter. These results suggested that in extreme IGE conditions, the upper rotor experiences a higher net benefit from the ground, which in turn increases rotor-rotor interactions on the lower rotor.

While the competitive nature between the rotor-rotor and rotor-ground interactions resulted in a non-monotonic trend in the upper rotor performance across various z/R conditions, the lower rotor performance showed less susceptibility to a systematic performance trend. Its performance remains relatively constant, with only minor inconsistencies observed across the z/R spectrum. This behavior was consistent for all inter-rotor spacings tested.

The effect of inter-rotor spacing on the rotor-rotor interactions is presented in Fig. 4.12b,c. The results were comparable to OGE conditions, where the interactions on the upper rotor increased with decreasing spacing while those of the lower rotor decreased. Generally, the upper rotor's performance improved as it approached the ground, with the interactions observed in any IGE conditions being less than those at the OGE condition. In contrast, the lower rotor showed no clear trend, as the interactions remained within approximately 2% of the OGE condition outside the most extreme IGE condition, where a more pronounced change is observed.

Although these findings illustrated how the rotor-rotor interactions are influenced by ground proximity, the underlying physical mechanisms driving these trends remain largely unexplored. For this, a hypothesis has been proposed from these findings to describe the performance of the CCR under IGE conditions:

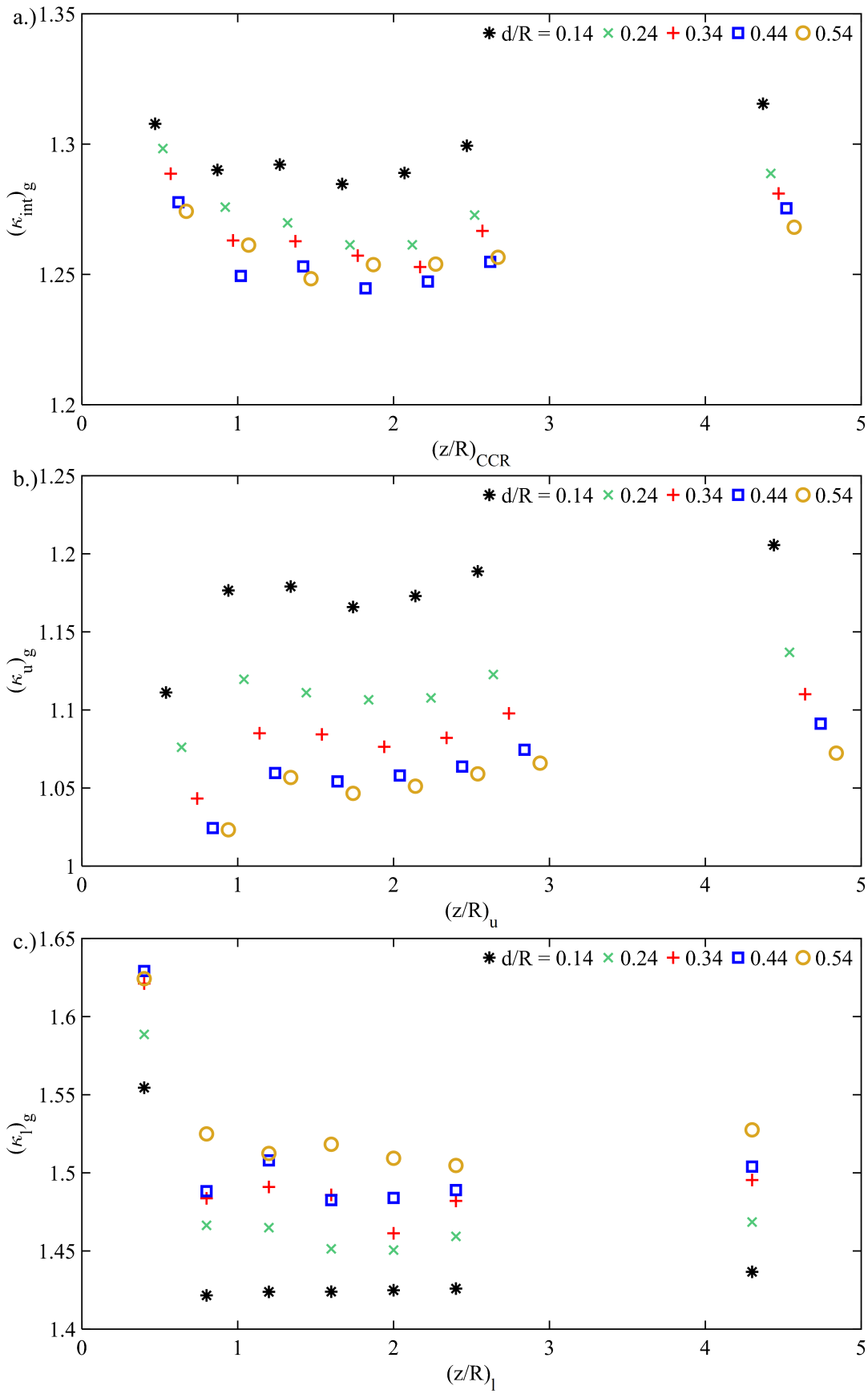

Figure 4.11: Effect of z/R on the rotor-rotor interactions of the CCR operating in IGE conditions. The total 95% confidence bound for each $(\kappa_{CCR})_g$ factor is within ± 0.090.

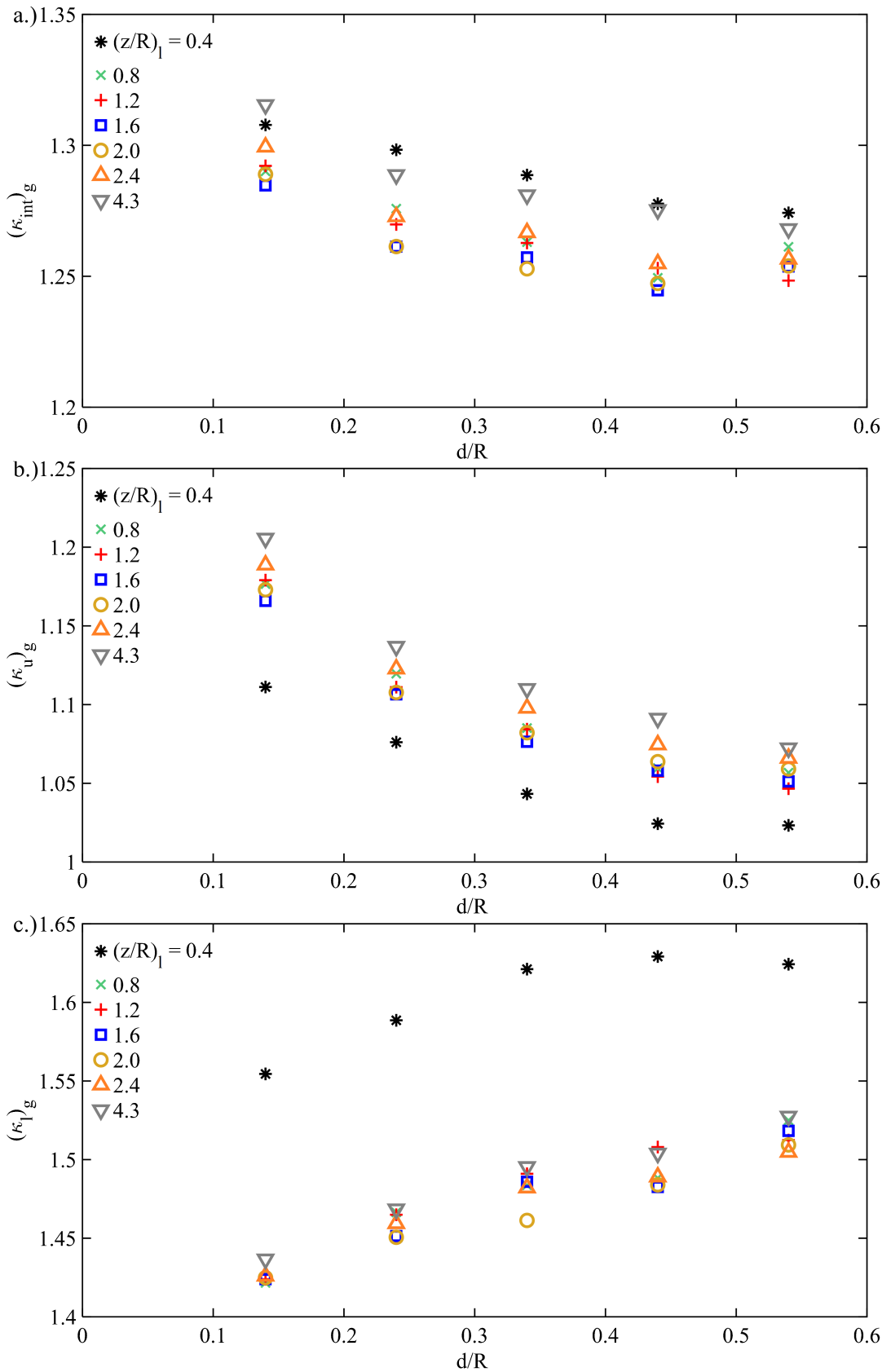

Figure 4.12: Effect of d/R on the rotor-rotor interactions of the CCR operating in IGE conditions. The total 95% confidence bound for each $(\kappa_{CCR})_g$ factor is within ± 0.090.

- When a rotor operates very close to the ground, the wake contraction reduces compared to OGE conditions. This results from the boundary forcing the wake to deflect radially outward and form an outwash. Consequently, when the CCR operates at $(z/R)_l = 0.4$, the upper rotor's wake experiences less contraction. This results in the wake impinging on a larger area of the lower rotor's disk, thereby increasing the inflow velocities over a higher portion of the lower rotor.

This hypothesis was tested using PIV to quantify the 2D velocity field through the rotor plane, followed by an inflow analysis. The results and discussion of the hypothesized flow field behavior, as well as a deeper analysis of the load measurements, are presented in Section 4.3 to gain further insights into the physical foundations driving the rotor performance IGE.

4.2.3 Comparison of the rotor-rotor interactions IGE to OGE

Assessing the performance of a CCR IGE has provided valuable insight into how ground proximity influences the interactions between rotors. The interactions between the rotors were found to be altered when compared to OGE, and distinct performance trends were observed across the parametric space. These interactional changes affect the overall performance of the CCR, which indicates changes in the aerodynamic environment of the system.

The previous analysis provided information that solely describes the performance effects of IGE operation on the rotor-rotor interactions, but further characterization towards comparing these interactions to their OGE counterparts is desired for a better understanding of the ground influence. This analysis will compare IGE and OGE interactions, which provides deeper insight into how ground proximity influences induced power consumption and helps to clarify the overall effect of the ground on each rotor.

Although a rotorcraft spends considerable time hovering IGE, most of its operational time is spent in OGE conditions. Therefore, hovering in OGE can be defined as the "rule", while hovering in IGE is the "exception." As such, comparing the power requirements between a specific IGE condition and general OGE operating conditions is valuable to highlight the deviations in rotor performance. To facilitate this comparison, this section evaluates the ratio of the rotor-rotor interactions IGE at each d/R to the respective interactions characterized in

OGE conditions. The factors developed for this analysis were summarized in Eqs. 3.11, where the IGE interferences factors $(\kappa_{int})_g$ & $(\kappa_{u|l})_g$ were normalized by their OGE counterparts, κ_{int} & $\kappa_{u|l}$. Based on these ratios, three scenarios can be identified for the coaxial rotor performance IGE:

1. **Increased interactions:** If $\kappa_{IGE} > \kappa_{OGE}$, it indicates that rotor-rotor interactions play a more significant role in rotor performance under IGE conditions.

2. **Decreased interactions:** If $\kappa_{IGE} < \kappa_{OGE}$, it indicates that rotor-ground interactions play a more significant role in rotor performance under IGE conditions.

3. **Unchanged interactions:** If $\kappa_{IGE} \approx \kappa_{OGE}$, it indicates that the *net* aerodynamic interactions between rotors remain similar between IGE and OGE conditions.

This analysis provides critical insight into whether the influence of the ground yields a net benefit or detriment to the performance of the coaxial rotor system. Figure 4.13 illustrates how this empirical parameter varies across the spectrum of IGE conditions for the CCR and its individual rotors.

It was initially observed through visual inspection of Fig. 4.13 that the rotor-rotor interactions exhibit minimal variation across the d/R spectrum, suggesting that the changes in rotor performance between OGE and IGE conditions were the same, regardless of inter-rotor spacing. The overall interference trends of the system are shown in Fig. 4.13a, where the interferences remained roughly equivalent to those in OGE conditions. However, they slightly reduced for most IGE conditions (except the most extreme z/R). This suggested that while the ground has a minimal impact on the overall rotor-rotor interactions, it does influence the performance of each rotor differently, particularly as the system nears the ground.

Figs. 4.13b,c highlight the changes in interactions for the individual rotors. The results showed that the ground benefits the upper rotor across all conditions, particularly in the most extreme IGE condition. In contrast, the lower rotor experienced interactions that remain largely comparable to OGE conditions, except when $(z/R)_l = 0.4$, where the ground influence causes the lower rotor performance to degrade by as much as 8%. This degradation is linked to the

rotor-rotor interactions and indicates that the ground reduces the rotor-rotor interactions of the upper rotor while increasing those interactions on the lower rotor in extreme ground conditions. These results underscore the complex influence of the ground on CCR performance, with a favorable effect on the upper rotor but a detrimental effect on the lower rotor under extreme IGE conditions.

4.3 Discussion

Performance measurements: To gain further insight into the performance of the coaxial rotor IGE, the rotor thrust sharing and collective blade pitch behavior for different IGE conditions were analyzed. As shown in Fig. 4.14a, the thrust sharing ratio between the upper and lower rotors varied as the system transitioned into IGE operation, indicating changes in aerodynamic interactions. Fig. 4.14b also illustrates variations in rotor collective pitch, where the lower rotor remains mostly constant for $z/R \geq 1.2$. Meanwhile, the collective of the upper rotor decreased by approximately $0.5°$ for the same z/R regime. This subtle change also pointed to minor alterations in the rotor interactions within this operating regime, in line with prior analysis of the load measurements (Fig. 4.11b,c).

More pronounced changes were observed as the rotor operates at $z/R < 1.2$. Under these conditions, thrust sharing was largely insensitive to variations in d/R, with only a 3% difference in the most extreme condition. This indicated that the ground substantially influences system performance more than rotor-rotor interactions. Notably, the collective of the lower rotor decreased by $2°$ to maintain constant thrust while balancing torque with the upper rotor. Conversely, the upper rotor collective decreased by approximately $1.5°$, and the collective pitch of the rotors started to converge at $z/R = 0.4$.

The total inflow for the lower rotor is a combined result of its own induced inflow, induced inflow effects from the upper rotor, and downwash from the upper rotor. In contrast, the inflow experienced by the upper rotor is influenced solely by its own induced inflow and induced effects from the lower rotor. In the presence of the ground, both rotors experience reduced induced inflow, leading to a reduction in collective pitch to maintain constant thrust, thereby lowering power consumption. However, in $z/R > 1.2$ regimes, the downwash from

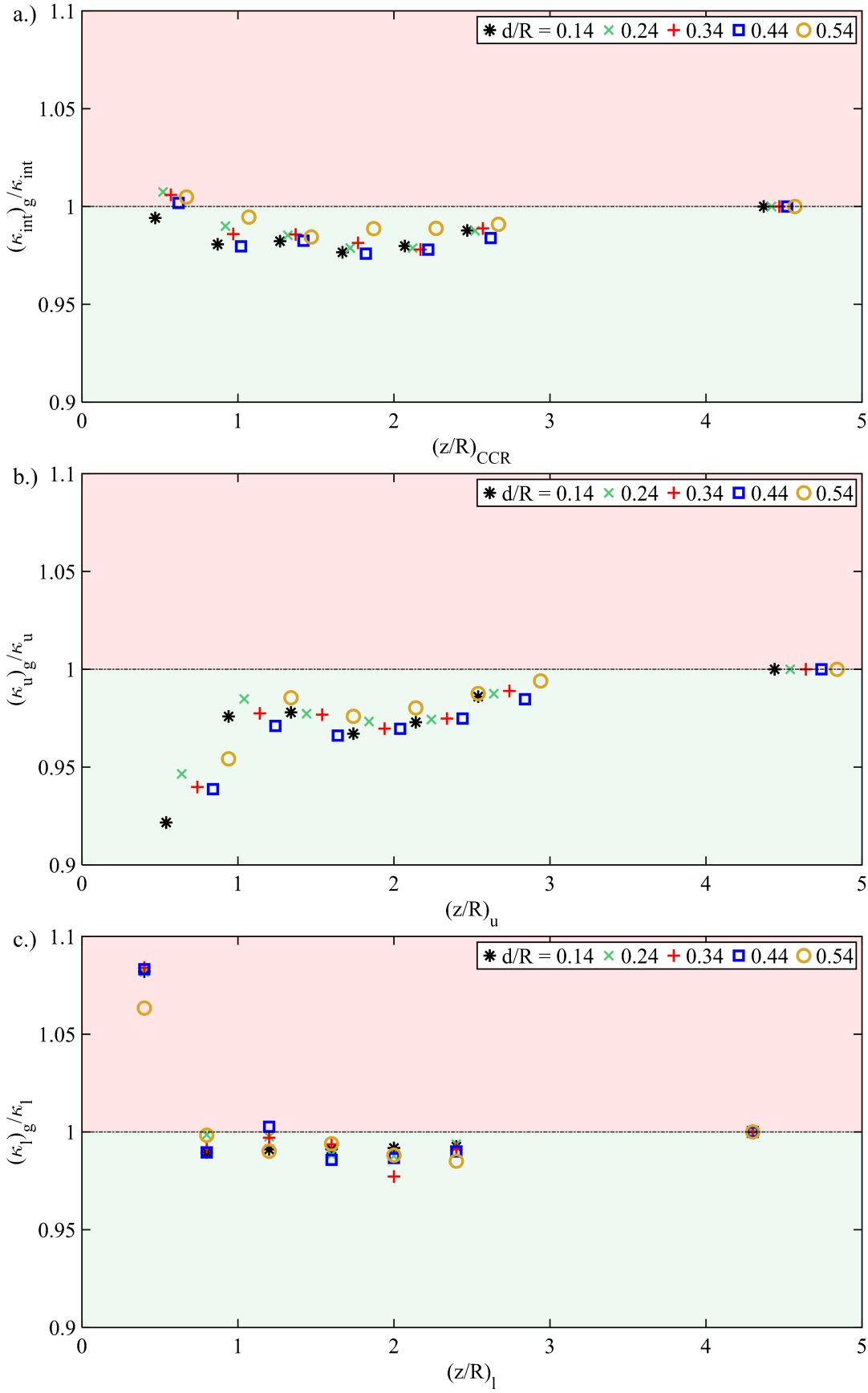

Figure 4.13: Net change in aerodynamic interactions of the CCR IGE when compared to the aerodynamic interactions experienced in OGE conditions.

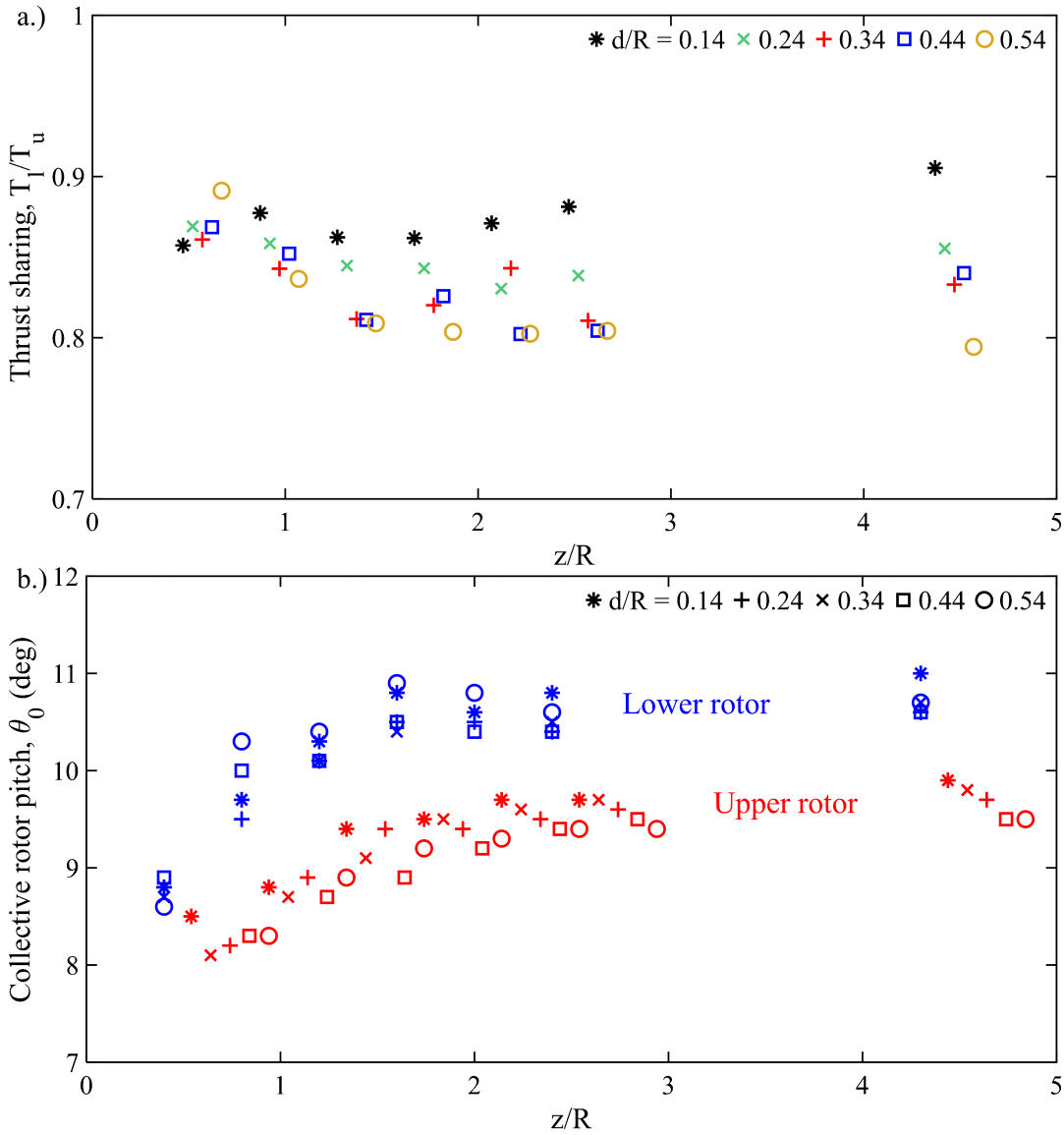

Figure 4.14: a). Rotor thrust sharing for $C_{T,CCR} = 0.0081$. b). Rotor collective pitch angles for $C_{T,CCR} = 0.0081$.

the upper rotor imposes substantial losses on the lower rotor, offsetting the performance benefit provided by the ground. Because the ground still provides a net benefit to the CCR (Fig. 4.9a), the torque reduction was achieved through a decrease in the upper rotor's collective. This decrease reduced the downwash impact on the lower rotor, which reduced the lower rotor's torque while keeping similar rotor-rotor interactions, so the overall torque balance trim condition was maintained.

At $z/R = 0.4$, the ground significantly limits the induced inflow of the lower rotor, reducing its negative interaction with the upper rotor, as observed in Fig. 4.11b. This results in

increased thrust of the upper rotor. The upper rotor collective is reduced to maintain a constant overall thrust, decreasing its torque consumption. Since the ground significantly impacts the lower rotor, the system maintained torque balance as the upper rotor's collective decreased. Compared to OGE conditions, the influence of the upper rotor's downwash on the lower rotor was more pronounced in IGE, which led to greater losses.

Flow field analysis: PIV measurements were performed to characterize the inflow patterns through the rotor planes of both a single rotor and a CCR system. These measurements provide a detailed quantification of the axial velocity fields, enabling an in-depth analysis correlating rotor inflow dynamics with observed aerodynamic load measurements. The post-processed PIV field of the CCR is provided here, and comparisons with the single rotor configuration are discussed further in appendix C. Visualization of the flow field offers insights into the rotor flow characteristics under varying operating conditions.

Figures 4.15 and 4.16 depict the axial velocity contours for the CCR system operating OGE and $z/R = 0.4$ conditions, respectively. These contours reveal a distinct slipstream boundary associated with the upper rotor, which propagates downstream and interacts with the lower rotor's inflow. In OGE conditions, the maximum axial velocity is approximately $2\ m/s$ higher than IGE, and the slipstream exhibits greater contraction due to reduced ground interference. Conversely, in IGE conditions, the flow field exhibits a pronounced upwash in the hub region of the coaxial rotor system, indicative of a recirculation zone. This recirculation region reduces effective thrust production over the central portion of the rotor disk.

The hypothesis regarding the rotor-rotor interaction dynamics posed in Sec. 4.2.2 was investigated using PIV techniques to quantify and compare the inflow behavior of the coaxial rotor system operating under IGE and OGE conditions. Figure 4.17a illustrates the measured inflow for the CCR in OGE and $z/R = 0.4$ conditions. Inflow profiles for $z/R = 1.6$ are omitted due to their near-identical similarity to the OGE condition. The radial location of the peak axial velocity on the lower rotor's plane was determined from Fig. 4.17a to evaluate the reduced wake contraction of the upper rotor at the $z/R = 0.4$ condition. The results reveal that from the OGE condition to $z/R = 0.4$, the maximum velocity location shifted outward by approximately 8%, from $r/R \sim 0.77$ to $r/R \sim 0.85$. This shift corresponds to an approximate

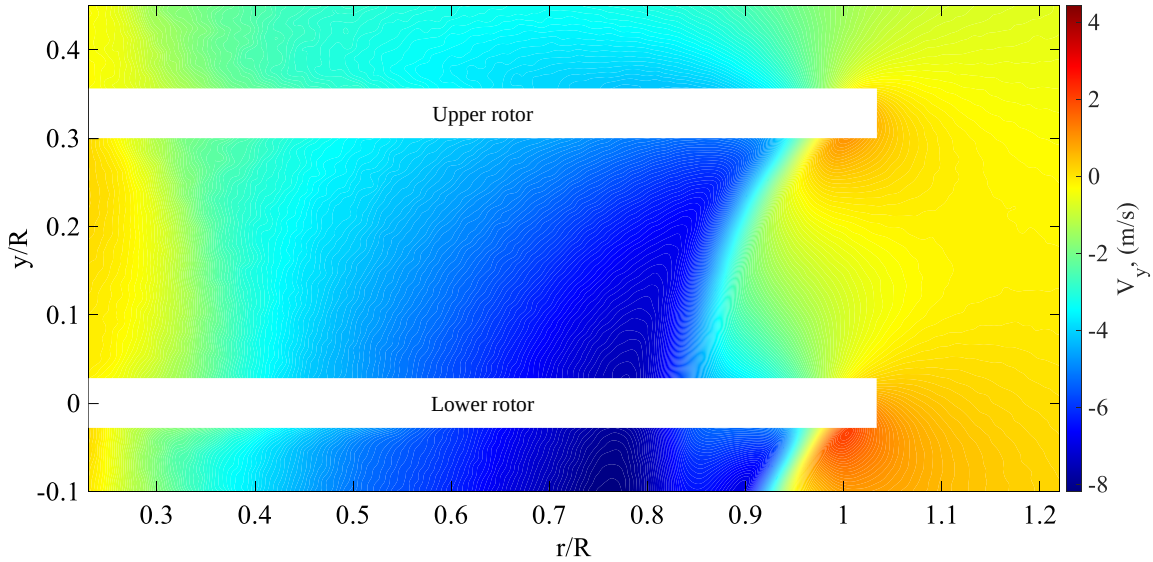

Figure 4.15: Axial velocity contour for the CCR system operating in OGE conditions at $d/R = 0.34$.

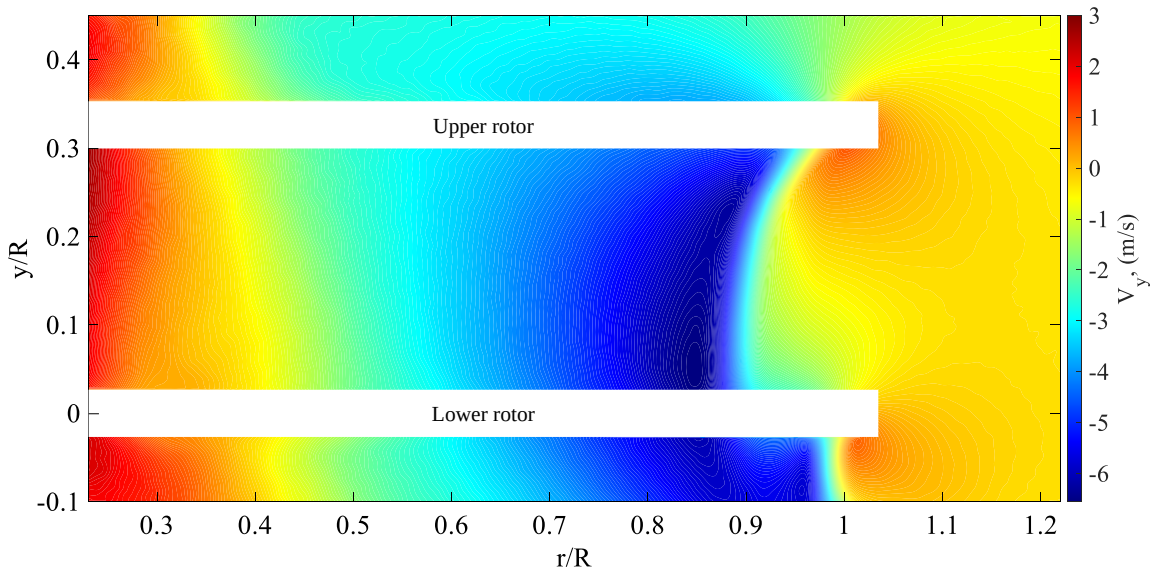

Figure 4.16: Axial velocity contour for the CCR system operating in $z/R = 0.4$ conditions at $d/R = 0.34$.

13% increase in the lower rotor's area immersed in the upper rotor's wake. The increased inflow indicates a heightened aerodynamic influence on the lower rotor, contributing to greater interactional losses.

Despite the increased impingement area of the upper rotor's wake on the lower rotor, the presence of the ground significantly diminishes the overall inflow magnitude. To validate that the larger impingement area of the upper rotor's wake intensifies the aerodynamic interactions

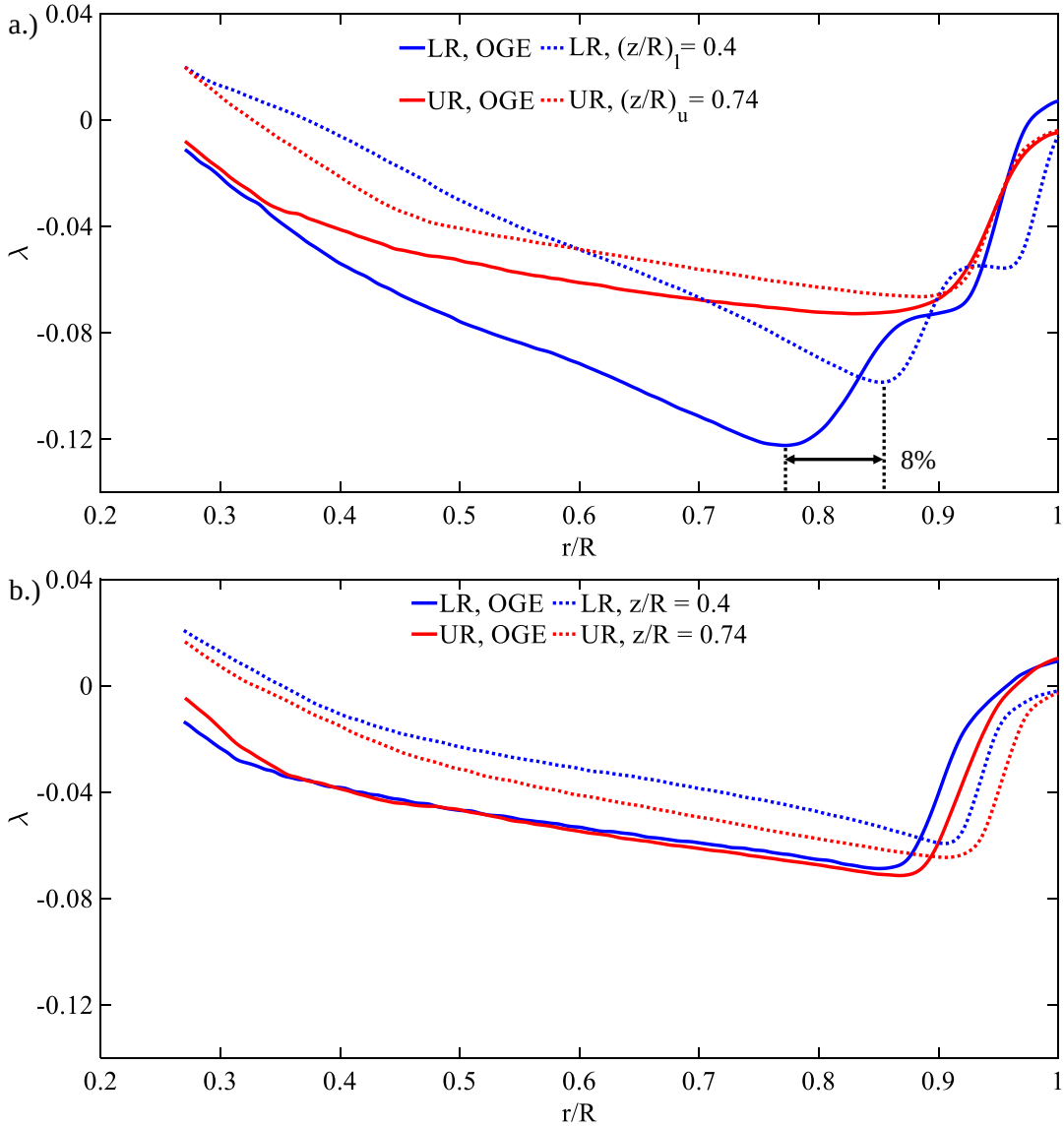

Figure 4.17: Rotor inflow at $d/R = 0.34$. a). CCR configuration. b). Single rotor configuration with thrust matched to CCR.

experienced by the lower rotor, a correlation was examined between the load measurements and the inflow data obtained through PIV. In the load measurements, a relative power metric was established by comparing the power of the upper and lower rotors in the counter-rotating coaxial rotor (CCR) system to that of a single rotor operating at the same height above the ground. Based on momentum theory, a corresponding inflow relationship was hypothesized: IGE, the relative inflow of the lower rotor should increase compared to OGE. In contrast, the relative inflow of the upper rotor should decrease under IGE conditions.

The momentum theory used to derive the empirical power factors established that the induced power is related to the inflow as $C_{Pi} = C_T\lambda$. To develop the empirical factors, a ratio was established to compare the CCR IGE performance to a reference, such as an isolated rotor at the same IGE condition when quantifying the rotor-rotor interactions in the presence of the ground. The thrust was held constant in load measurements, so comparing an analogous ratio for inflow should yield a similar trend to the power factors. Equation 4.1 presents a general form of this equation. In this equation, the left-hand side represents the power ratios quantified through load measurements, while the ratio on the right-hand side corresponds to the inflow ratio between the CCR and the single rotor under the same operating condition. Given that the rotor-rotor interactions of the lower rotor increase under extreme ground effect conditions, the inflow ratio for the lower rotor should also increase. Conversely, the inflow ratio of the upper rotor is expected to reduce to follow the trend observed in the load measurements.

$$\frac{C_{Pi,u|l}}{C_{Pi,SR}} \approx \frac{\lambda_{u|l}}{\lambda_{SR}} \tag{4.1}$$

In the CCR (Fig. 4.17a), non-linearity in the lower rotor inflow is evident where the upper rotor's wake impinges, as noted previously. The difference in the inflow between the OGE and IGE conditions is also notable, with an upwash near the rotor hub in the IGE condition. Similarly, the single rotor (Fig. 4.17a) inflow at an equivalent thrust condition exhibits an upwash region near the hub. The total rotor inflow was computed by integrating the spanwise inflow variation from the root cutout to the blade tip and around the rotor disk, per Eq. 2.1. The summary of rotor inflow for the three z/R conditions is provided in Table 4.2. The inflow ratio across the operating conditions is expected to follow a similar trend found from the load measurements. However, the computed inflow ratios did not meet this expectation.

The absence of a clear correlation between the load measurements and PIV data suggests that the momentum theory relationship underlying this hypothesis may only partially apply in this context. The theoretical relationship between the thrust, power, and inflow in momentum theory assumes uniform inflow, no tip effects, and inviscid, one-dimensional flow in momentum theory. However, as demonstrated in Fig. 4.17, the spanwise distribution of inflow is

Table 4.2: Comparison of the relative inflow between extreme, intermediate, and out-of-ground operating conditions.

Operating condition	$(\kappa_u)_g$	$\frac{\lambda_{UR}}{\lambda_{SR}}$	$(\kappa_l)_g$	$\frac{\lambda_{LR}}{\lambda_{SR}}$
OGE	1.11	1.16	1.50	1.73
$z/R = 1.6$	1.08	1.10	1.49	1.78
$z/R = 0.4$	1.04	1.09	1.62	1.68

highly non-uniform, characterized by the near-zero inflow at the blade root, peaking around $r/R = 0.8$, and diminishing again near the blade tip. Moreover, the impact of viscous, 3D flow, including radial spanwise flow induced by centrifugal forces, and the presence of wake swirl all affect CCR performance in ways that momentum theory does not capture. This discrepancy between the load and inflow trends underscores the limitations inherent in applying low-order models like momentum theory to relate flow fields with load measurements.

In response to these findings, alternative approaches were employed to quantify the relationship between load measurements and rotor inflow. These alternative approaches form relationships between the thrust, power, and inflow while neglecting some restrictive assumptions imposed in momentum theory. Blade element theory (BET), for instance, accommodates the non-uniform inflow thrust distribution and calculates the induced power required for hover as

$$C_{Pi} = \int \lambda dC_T \quad \text{where} \quad dC_T = 0.5\sigma C_{l\alpha}(\theta r^2 - \lambda r)dr. \tag{4.2}$$

However, in the time-averaged PIV results of this study, the near-zero inflow near the blade tip results in a significant increase in thrust using the BET equation. This limitation renders BET less effective for estimating the induced power from experimental data since the thrust distribution near the blade tip goes to zero in practice. Thus, the correlation between induced power estimation from load measurements and the rotor inflow profile obtained via PIV cannot be accurately represented by directly applying experimental data to momentum theory or BET. Instead, the correlation is governed by a complex function involving the integrated effects of non-uniform inflow and the spatial thrust distribution across the rotor disk. Future works aim

to address the correlation between the rotor inflow and load measurements to verify that the additional performance penalty on the lower rotor in extreme IGE results from an increased area of upper rotor wake impingement.

This chapter applied a theoretical foundation to an experimental dataset of CCR performance IGE. While the CCR system showed minimal variation compared to OGE conditions, the ground highly influenced the upper and lower rotors, particularly under extreme IGE conditions. Detailed investigation using PIV revealed that the upper rotor wake contracted less in IGE, leading to increased impingement on the lower rotor and, consequently, higher aerodynamic losses. Further analysis of the load measurements demonstrated a non-linear thrust-sharing relationship between the upper and lower rotors, challenging the validity of momentum theory for correlating performance metrics with PIV flow fields. The following chapter expands this analysis by examining CCR performance at varying Reynolds numbers to quantify the effects on rotor behavior IGE.

Chapter 5

Reynolds number effect on the aerodynamic interactions of a hovering coaxial rotor system

This chapter seeks to characterize the influence of Reynolds number on the aerodynamic interactions for both a single rotor and CCR hovering OGE and IGE. As CCRs continue to evolve and find applications across a wide range of operating conditions, understanding these influences is critical for optimizing their design and performance. The chapter first examines the non-ideal losses of a single rotor OGE across three tip Reynolds number conditions, followed by an analysis of rotor-ground interactions for the single rotor. Then, the coaxial configuration is introduced, and the rotor-rotor interactions of the CCR OGE are quantified. Finally, results showing the competitive effects from rotor-ground and rotor-rotor interactions of the CCR IGE are presented and discussed.

5.1 Single rotor performance characterization

5.1.1 Out-of-ground effect

Previous studies on hovering rotors at low Reynolds numbers have reported performance degradation due to varying wake characteristics from higher Reynolds number conditions [53, 8, 50]. The rotor wake structure significantly influences the induced power consumption of the rotor, and therefore, induced power requirements are expected to vary with the Reynolds number. Fig. 5.1 compares the hovering efficiency of the single lower rotor for the three Reynolds number conditions considered in this study, revealing that the onset of stall occurs at a lower C_T/σ as the Reynolds number decreased. However, a near-linear FM increase was observed for

$C_T/\sigma \lessapprox 0.6$ for all conditions, indicating operation in an essentially constant profile power regime. Consequently, the empirical power factors were computed using experimental data below this stall regime.

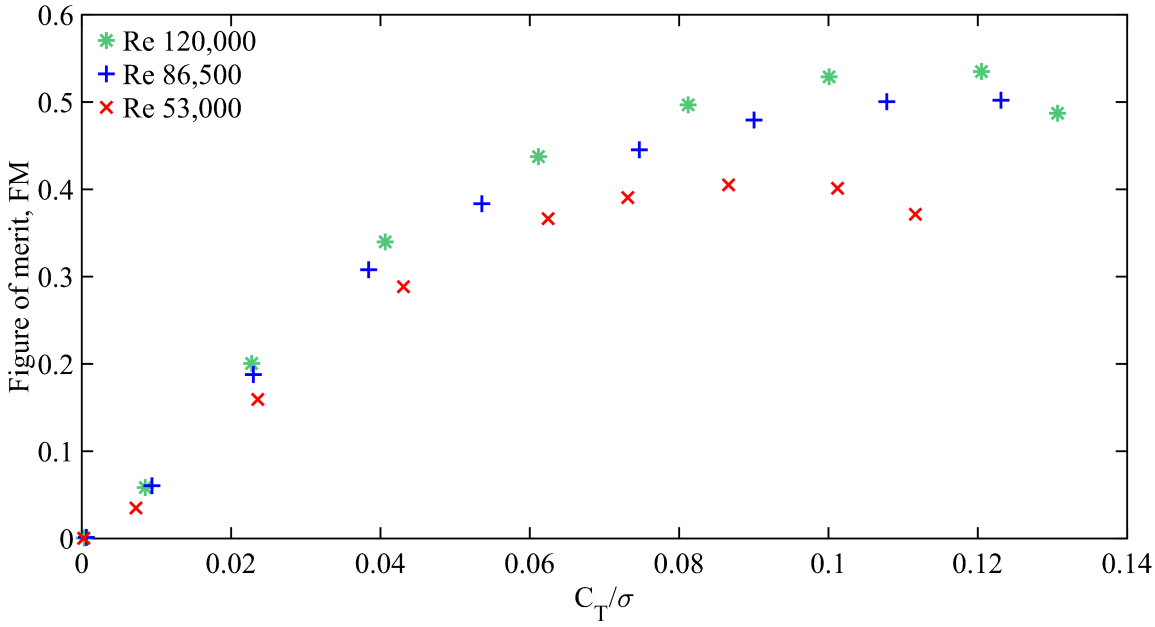

Figure 5.1: Single rotor figure of merit variation with tip Reynolds number.

Figure 5.2 presents the non-ideal induced losses across the Reynolds number spectrum for the single upper and lower rotors. The performance between them was similar at each Reynolds number, where the non-ideal losses of the upper rotor consumed $\sim 2\%$ more induced power for all conditions. Furthermore, the non-ideal losses of the rotor at $Re = 86,500$ were about 4% greater than the $Re = 120,000$ condition, and the non-ideal losses at $Re = 53,000$ were significantly greater, increasing by roughly 18%. These results suggested that the Reynolds number strongly affects the rotor wake structure.

5.1.2 In-ground effect

In quantifying the ground effect on a single rotor, the induced power factor describing the ground effect should remain $\lessapprox 1$ across all Reynolds numbers since the comparison is to an OGE condition. Figure 5.3 illustrates the effect of the ground on the induced power for the upper and lower single rotors, showing that the benefit observed across the Reynolds number spectrum was consistent with predictions for single rotor models. At the closest in-ground

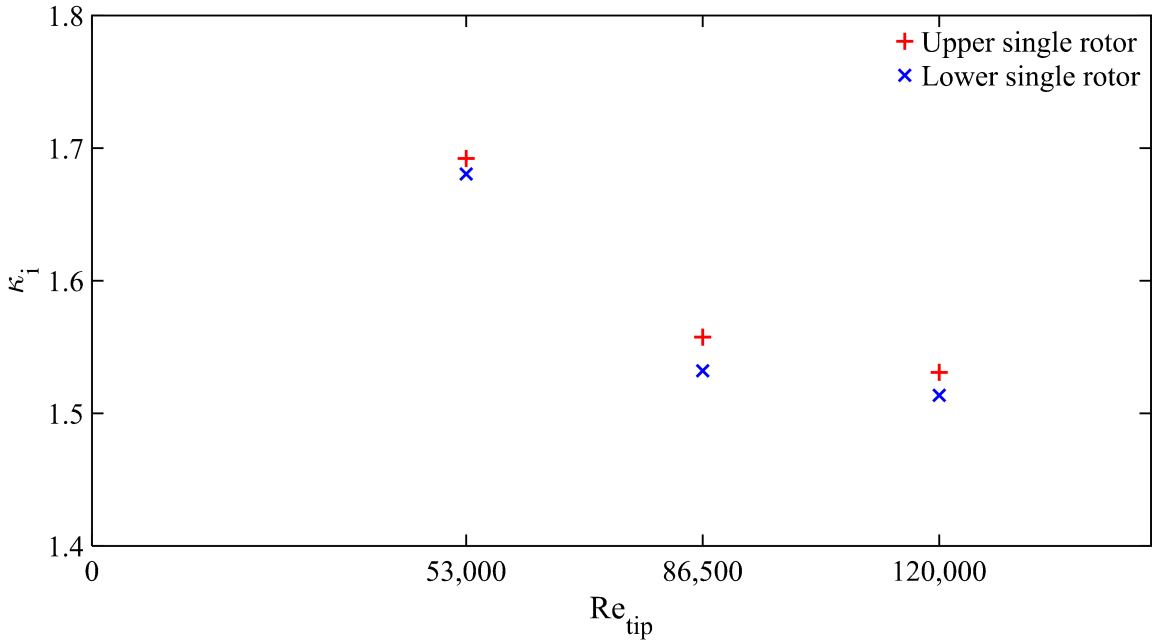

Figure 5.2: Reynolds number effect on the single rotor induced power factor. The total uncertainties for the upper rotor are within ± 0.025 for all Re_{tip} conditions, and uncertainties for the lower rotor are within ± 0.035.

condition for both rotors, the rotor-ground interaction decreased by approximately 5% as the Reynolds number decreased, suggesting that the ground was slightly less beneficial at lower Reynolds numbers. This decrease may be partially attributed to recirculation effects that are more pronounced at low Reynolds numbers, however, future work to fully address this observation is necessary. Similar to the method applied in Ch. 4, a fourth-order polynomial fit was fitted to the κ_g characterization for the upper rotor at Reynolds numbers of 86,500 and 53,000 to quantify the performance of the CCR IGE across the entire parametric space.

5.2 Coaxial rotor performance characterization

After characterizing single rotor performance across OGE and IGE conditions, the Reynolds number effect on the coaxial rotor was examined. First, the rotor-rotor interactions were quantified for the range of d/R conditions; then, the IGE performance was examined.

5.2.1 Out-of-ground effect

For a single Reynolds number, the performance of the lower rotor improved as the inter-rotor spacing decreased, while the performance of the upper rotor degraded in the CCR OGE. From

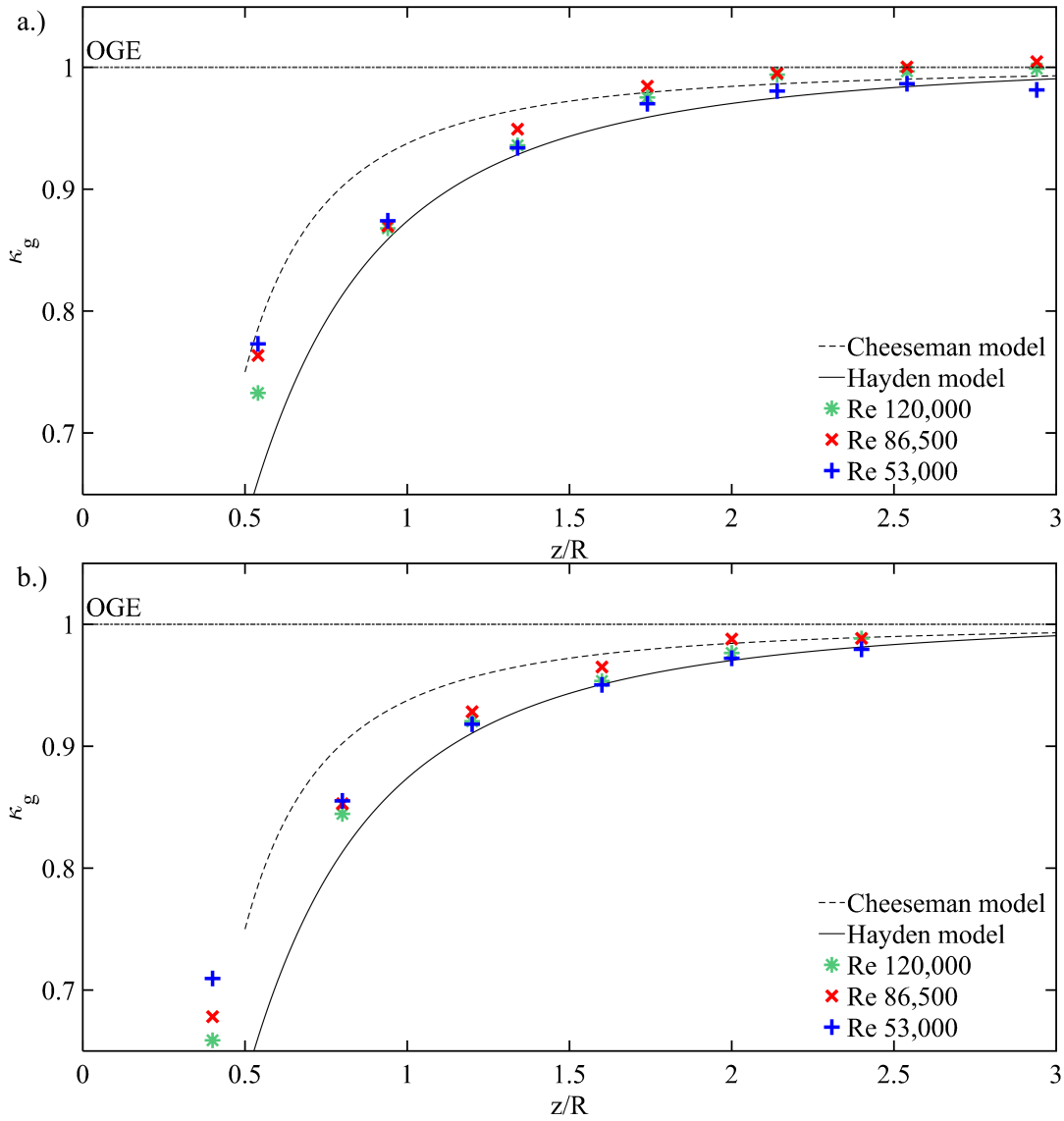

Figure 5.3: Effect of Reynolds number on κ_g. a). Upper rotor. b). Lower rotor. The total uncertainties for the upper rotor are within ± 0.045 for all Re_{tip} conditions, and uncertainties for the lower rotor are within ± 0.050.

a fundamental physics perspective, these general trends in the rotor performance should remain as the Reynolds number varies; however, the extent to which the induced power is affected as any interactional changes occur must be investigated further.

Figure 5.4 presents the rotor-rotor interactions of the coaxial rotor system OGE across a range of Reynolds numbers. The overall interferences are illustrated in Fig. 5.4a, showing that at small d/R operation, the highest Reynolds number condition exhibited slightly more interference than the two lower Reynolds numbers cases. Notably, the interferences at the $Re = 53,000$ condition were constant, indicating that rotor spacing had minimal impact on

rotor-rotor interactions. The upper and lower rotor performance were analyzed to address any changes not visible in the overall interferences.

Fig. 5.4b,c depict these interactions for each rotor. Since the overall interference showed minor discrepancies where they slightly decreased with Reynolds number, the individual rotor influences should reflect that trend. The upper rotor's performance was invariant to Reynolds number, suggesting that the influences of the lower rotor on its performance do not change. In contrast, the lower rotor exhibited a roughly $6 - 9\%$ performance change across different Reynolds numbers, and the interactions reduced with Reynolds number.

The upper rotor of the coaxial system experiences a negative influence from the lower rotor due to induced inflow effects. In comparison, the lower rotor is subject to two negative influences from the upper rotor: induced inflow effects and direct wake impingement of the upper rotor wake on its rotor plane. Given that the upper rotor's interactions remain unchanged while the lower rotor's interactions vary, the mechanism for which the lower rotor interactional changes originate must lie in the wake impingement of the upper rotor. Previous studies have shown that the wake structure of low Reynolds number rotors differs from high Reynolds numbers, with increased wake diffusivity and modifications in tip vortex strength and trajectory as the wake convects downstream [8, 53, 65]. These wake modifications may reduce the downwash effects on the lower rotor and should be explored further in future work.

5.2.2 In-ground effect

Until now, the Reynolds number performance effects of the single rotor OGE, IGE, and the coaxial rotor OGE have been evaluated. The influence of Reynolds number on non-ideal losses was quantified with the single rotor OGE, where viscous effects modified the wake characteristics, leading to rotor performance degradation. In the single rotor IGE configuration, the ground altered the wake characteristics of the rotor by directing the slipstream radially outwards. This resulted in performance improvements, and changing the Reynolds number minimally impacts the rotor-ground interactions. Changing the Reynolds number affected rotor-rotor interactions for the coaxial rotor in OGE, as the wake of the upper rotor had less influence on the lower rotor plane as the Reynolds number decreased. With these rotor configurations characterized across

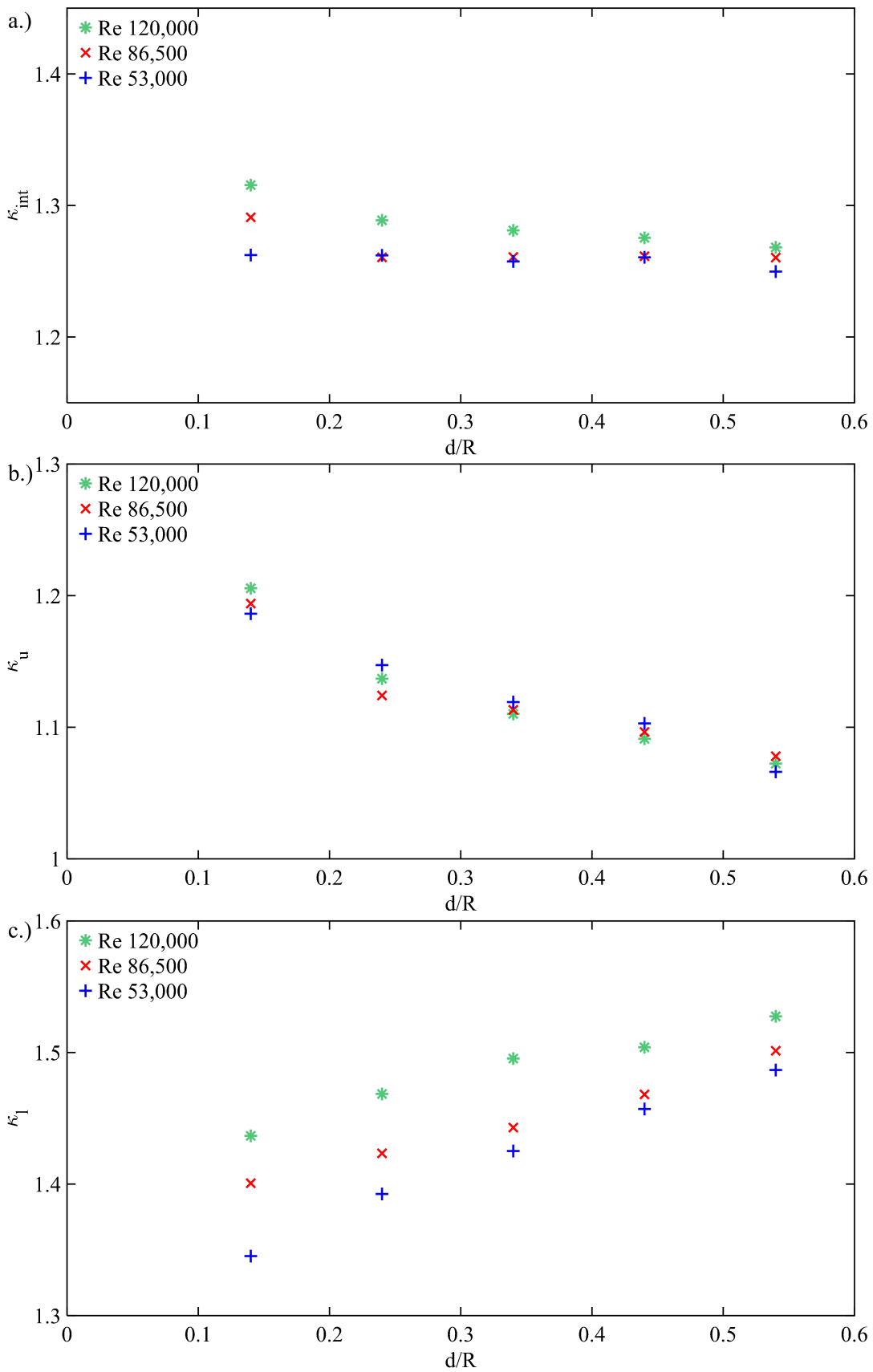

Figure 5.4: Rotor-rotor interactions in out-of-ground effect with varying Reynolds number conditions. a). $Re_{tip} = 120,000$. b). $Re_{tip} = 86,500$. c). $Re_{tip} = 53,000$. The total uncertainties for all Re_{tip} conditions are within ± 0.050.

the full Reynolds number spectrum of the study, the ground plane was introduced to analyze the performance of the CCR IGE. The following analysis of CCR IGE was performed similarly to Ch. 4. Across Reynolds number conditions, the net ground effect of the CCR showed similar variations that highlighted the presence of rotor-rotor interactions. As such, the net rotor-ground interactions are presented and briefly discussed in appendix D. The rotor-rotor interactions in the presence of the ground showed drastic changes. This section is focused on the rotor-rotor interactions in the presence of the ground and discusses the observed performance behavior.

Figure 5.5 highlights the rotor-rotor interferences as a function of the ground height, and each subfigure represents the interferences at a particular Reynolds number condition. The highest condition, discussed in Ch. 4, experienced a shallow decrease in interferences as the rotor system first entered IGE, then increased again as the system moved closer to the ground. The intermediate Reynolds number condition displayed similar behavior, with a slight decrease in interference followed by an increase in closer IGE conditions. However, in these close IGE regimes, smaller inter-rotor spacing conditions showed less interference increase, and at $d/R = 0.14$, the interferences remain roughly constant across the ground height range. These differences were exacerbated in the lowest Reynolds number condition, as the interferences displayed a drastically different trend. Here, the interferences remained similar to OGE conditions in larger IGE conditions, but when the ground height was reduced to $(z/R)_{CCR} \lessapprox 1.5$, the interference decreased further. A general trend emerged across these three Reynolds number conditions where interference in close IGE conditions decreased with Reynolds number, with more pronounced differences between $Re = 86,500$ and $Re = 53,000$. To investigate the root of these interference changes, the individual rotor influences were analyzed.

The influences of the lower rotor on the upper rotor are quantified with respect to the ground height in Fig. 5.6. Visual inspection of the d/R effect showed that for the two highest Reynolds numbers, the interactions of the upper rotor remained relatively constant for the same d/R, with minor differences $< 2\%$ in the induced power effect between conditions. However, the upper rotor in the lowest Reynolds number condition experienced more interactional losses for the same d/R, by about $3 - 5\%$. As ground height changed, the interactions of the upper

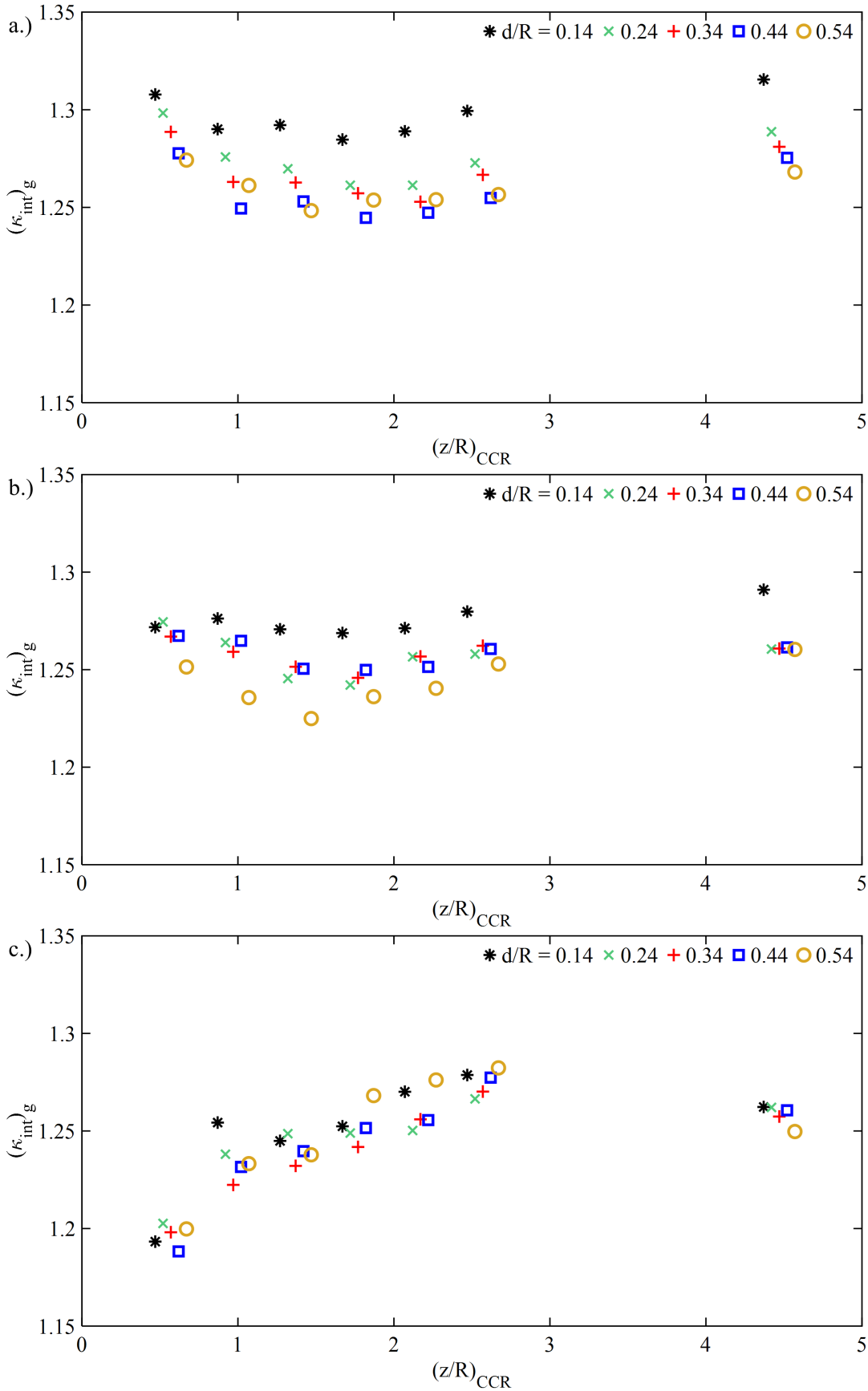

Figure 5.5: Rotor-rotor interferences in the presence of the ground with varying Reynolds number conditions. a). $Re_{tip} = 120,000$. b). $Re_{tip} = 86,500$. c). $Re_{tip} = 53,000$. The total uncertainties for all Re_{tip} conditions are within ± 0.105.

rotor in the lowest two Reynolds numbers followed a similar trend to the base Reynolds number, with local fluctuating trends in the interactions present for intermediate z/R conditions, followed by a sharp decrease at the most extreme IGE condition. These observations regarding the interactions of the upper rotor IGE with respect to d/R and z/R provide further proof that the influences of the lower rotor on the upper rotor are insensitive to a change in Reynolds number across a wide range of operating conditions.

The influence of the upper rotor on the lower rotor, with respect to the ground height, is presented in Fig. 5.7. Again, visual inspection of the d/R effect between the two highest Reynolds number conditions showed minimal variation in the induced power effect. However, in the lowest Reynolds number condition, the interactions for a specific d/R reduced significantly compared to Fig. 5.7a,b, particularly for smaller inter-rotor spacing cases.

In the two highest Reynolds number cases, slight variation was observed across the z/R range, and random fluctuations in the induced power effect were present in both for intermediate IGE conditions. One noticeable change was that the sudden increase in induced power due to interactions is less pronounced for the middle Reynolds number condition at $z/R = 0.4$, suggesting that the upper rotor influences on the lower rotor decreased in this condition. In the lowest Reynolds number condition, the influences were significantly different, as the smaller d/R conditions remained constant, while the larger d/R conditions exhibited an interactional decrease as the CCR moved closer to the ground. This indicates that contrary to the upper rotor interactions, the lower rotor interactions depend on both d/R and z/R.

In summary, it was observed in OGE conditions that the upper rotor's interactions remained largely constant, while the lower rotor interactions exhibited a sensitivity to d/R. Similarly, in IGE conditions, the upper rotor showed only minor variations with respect to d/R, and the interactions showed a constant trend across the z/R range. The lower rotor IGE, however, displayed variation with respect to d/R and z/R, particularly at the lowest Reynolds number condition. These observations further elucidate the hypothesis that between Reynolds number cases, there are fundamental differences in the wake structure of the upper rotor as it impinges on the lower rotor's plane. Further investigation into specific factors influencing these interactions is required and will be the focus of future experimental studies.

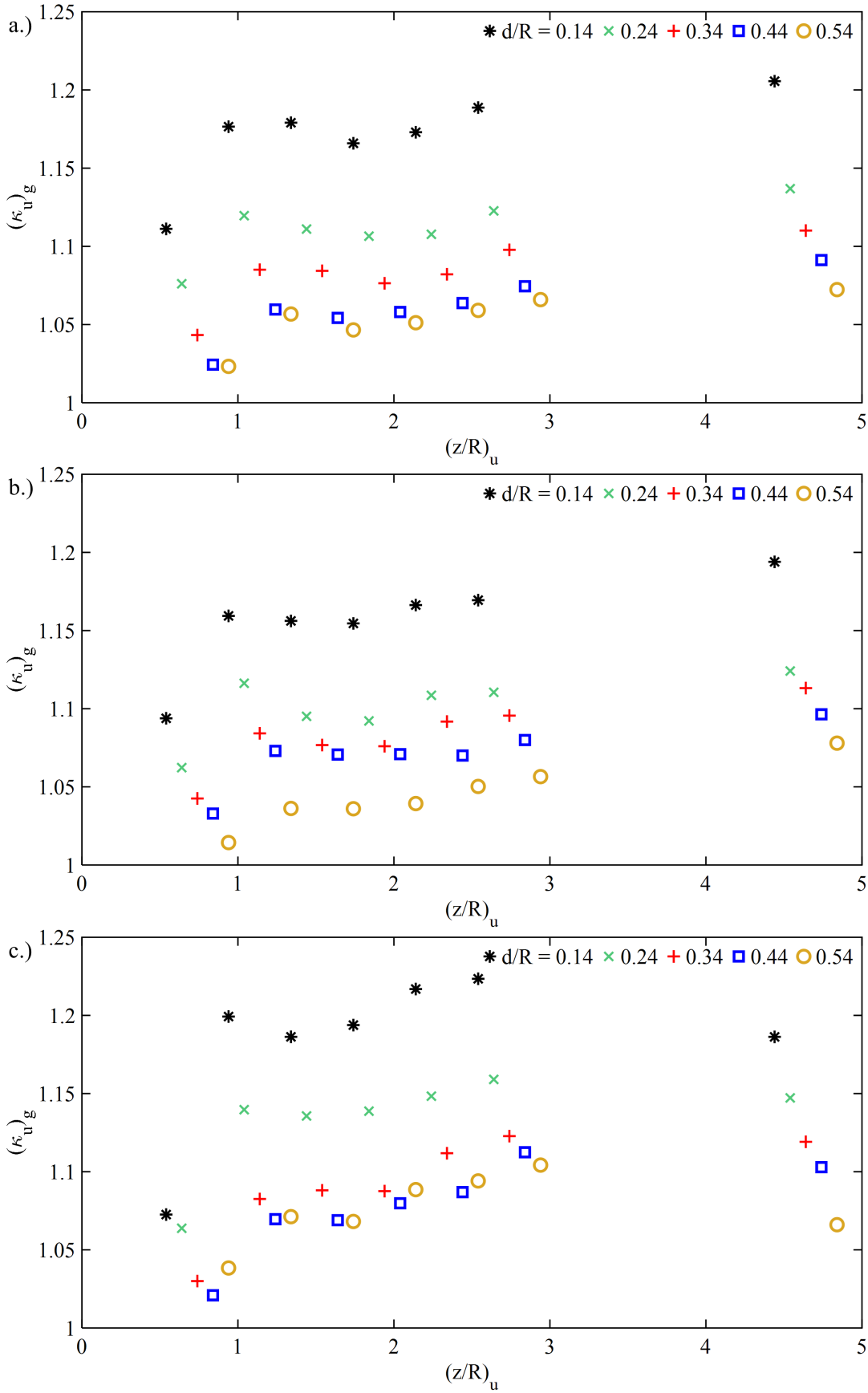

Figure 5.6: Influences of the lower rotor on the upper rotor in the presence of the ground with varying Reynolds number conditions. a). $Re_{tip} = 120,000$. b). $Re_{tip} = 86,500$. c). $Re_{tip} = 53,000$. The total uncertainties for all Re_{tip} conditions are within ± 0.095.

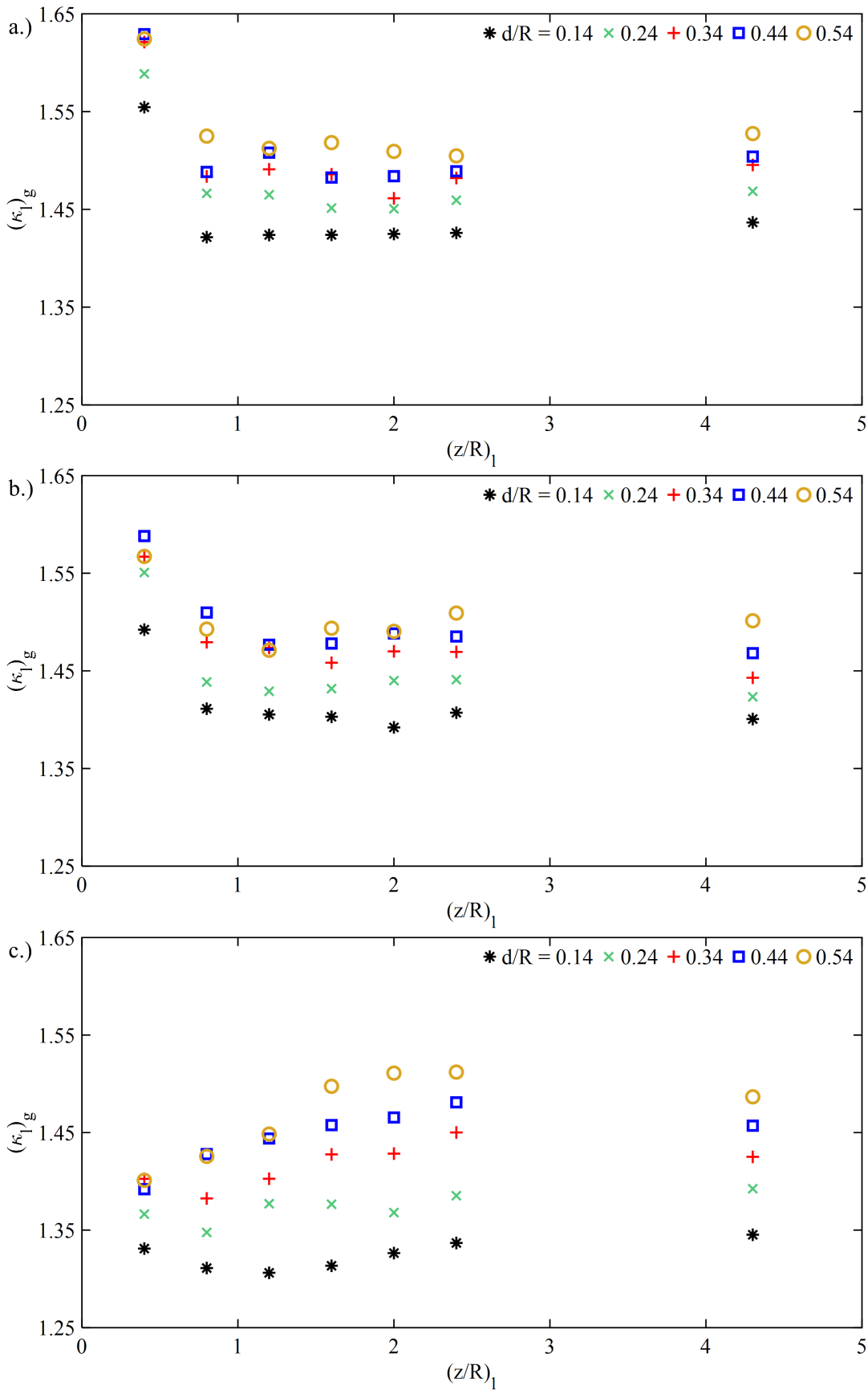

Figure 5.7: Influences of the upper rotor on the lower rotor in the presence of the ground with varying Reynolds number conditions. a). $Re_{tip} = 120,000$. b). $Re_{tip} = 86,500$. c). $Re_{tip} = 53,000$. The total uncertainties for all Re_{tip} conditions are within ± 0.110.

Chapter 6

Conclusions and future work

6.1 Conclusions and implications

This thesis presented two experimental studies: 1) quantification of the aerodynamic interactions in a CCR system hovering IGE, and 2) an assessment of the Reynolds number influence on rotor performance and aerodynamic interactions. The first study integrated momentum theory with an experimental coaxial rotor facility to analyze the aerodynamic loads acting on the CCR system. These experiments isolated rotor-ground and rotor-rotor interactions and provided insights into their contributions to the induced power requirements of the CCR in IGE conditions. The second study extended this analysis across varying rotor speeds, enabling an evaluation of how viscous effects at different Reynolds numbers impact rotor performance.

Some key conclusions and implications of these studies are provided below:

6.1.1 Conclusions from quantifying the aerodynamic interactions of a hovering coaxial rotor system

1. Using momentum theory, empirical power correction factors were derived to quantify the performance effects of rotor-rotor and rotor-ground interactions. These factors proved effective in showing that low-order modeling tools can be used to predict rotor performance with high accuracy.

2. The CCR operating IGE demonstrated performance characteristics similar to two single rotors with half the solidity. Minor variations in induced power of the CCR indicated

changes in rotor-rotor interactions, which significantly impacted the net ground effect felt by the individual rotors comprising the CCR.

3. These rotor-rotor interactions were analyzed further to understand how they vary in the presence of the ground. As the CCR system approached very close to the ground, the interactions of the lower rotor increased by up to 8%, while those of the upper rotor decreased by a similar magnitude compared to the interactions in OGE.

4. Attempts to explain the physical foundations driving the rotor performance IGE by correlating rotor performance through inflow and load measurements revealed limitations in momentum theory for explaining this behavior. Discrepancies were attributed to integrated effects of the inflow and changes in rotor thrust distribution under IGE conditions, which are not resolvable using experimental data and momentum theory alone.

The implications of these findings are described below:

1. As coaxial rotor systems gain widespread adoption across various applications, low-order models offer valuable predictive capability for early-stage design, particularly for evaluating rotor-rotor and rotor-ground interactions.

2. Developing comprehensive performance trends across a broad parametric range has implications for enhancing pilot training tools and flight simulators, offering improved handling guidance across different flight conditions.

3. A deeper understanding of the interactional aerodynamics IGE can inform handling strategies and safety measures, as rotor performance was observed to be sensitive to changes in IGE conditions. This knowledge is critical for mitigating risks associated with CCR operation, particularly in complex or dynamic environments.

6.1.2 Conclusions from the Reynolds number effect on rotor performance and aerodynamic interactions

1. The empirical power correction factors demonstrated robustness and usefulness across a range of Reynolds numbers, and accurately captured changes in the aerodynamic interactions.

2. For a single rotor OGE, induced power losses increased as the Reynolds number decreased, suggesting an increase in induced losses due to the growing influence of viscous effects. However, the single rotor IGE highlighted that the ground effect was largely invariant to the Reynolds number, suggesting that the ground effect is independent of the non-ideal induced losses.

3. In OGE, the upper rotor's aerodynamic interactions were largely invariant to Reynolds number, while the lower rotor experienced a reduction in interactions as Reynolds number decreased. This suggested the presence of different wake characteristics of the upper rotor as it impinges on the lower rotor.

4. In IGE, the upper rotor performance was largely unaffected by changes in ground height. However, the lower rotor showed significant performance alterations, with its interactions in the lowest Reynolds number condition exhibiting substantial performance differences when the rotor system was operated IGE.

The implications of these findings are described below:

1. As coaxial rotor technology is being integrated into applications across various rotor sizes and operating conditions, understanding the effects of Reynolds number and viscous phenomena will guide more informed and complete design decisions.

2. Quantifying how aerodynamic interactions evolve with Reynolds number provides critical insights for engineers, scientists, and operators, aiding in developing, operating, and maintaining CCR systems.

6.2 Recommendations for future work

1. The inherent coupling of rotor-rotor and rotor-ground interactions suggests that further methods to decouple these effects would enhance the accuracy of current models. While complete decoupling may not be possible, alternative rotor performance methods could verify and extend the present methodology.

2. Expanding the current body of research by systematically investigating different rotor parameters (number of blades, twist, taper) and operating conditions (axial climb, descent) would broaden the understanding of CCR performance. Low-order tools should continue to be employed to quantify interactional changes, improving performance predictions and safety considerations.

3. Further research is essential to understand the inflow behavior and its correlation with rotor loads, especially under IGE conditions where rotor-rotor interactions exhibit significant variation. This would address the limitations of momentum theory in capturing integrated inflow and radial thrust distribution effects.

4. A focused investigation on the lower rotor's performance at low Reynolds numbers is necessary, as CCR systems operating in this regime, such as small drones, are becoming increasingly common. Understanding these performance characteristics is vital for improving safety and operational efficiency in these vehicles.

5. In the Reynolds number investigation, the performance of the lower rotor exhibited minimal variation across the two highest Reynolds number conditions, while demonstrating more pronounced differences at the two lowest conditions. This behavior suggests the presence of a specific Reynolds number regime at which viscous effects increasingly influence rotor interactions. Further load measurements to quantify potential performance plateaus and delineate interaction regimes could provide essential insights into rotor performance across distinct Reynolds number domains.

References

[1] Robinson helicopter. https://www.robinsonheli.com/.

[2] NASA. https://www.lockheedmartin.com/.

[3] Lockheed Martin. https://science.nasa.gov/mission/mars-2020-perseverance/ingenuity-mars-helicopter/.

[4] Puneet Singh. *Aeromechanics of Coaxial Rotor Helicopters using the Viscous Vortex Particle Method*. PhD thesis, University of Michigan, 2020.

[5] Manikandan Ramasamy. Hover performance measurements toward understanding aerodynamic interference in coaxial, tandem, and tilt rotors. *Journal of the American Helicopter Society*, 60(3):1–17, 2015.

[6] Patrick Mortimer, Jayant Sirohi, Stefan Platzer, and J Rauleder. Coaxial rotor wake measurements in hover using phase-resolved and time-resolved piv. In *Proc. Vertical Flight Soc. 75th Annu. Forum*, pages 13–16, 2019.

[7] Philip E Tanner, Austin D Overmeyer, Luther N Jenkins, Chung-Sheng Yao, and Scott M Bartram. Experimental investigation of rotorcraft outwash in ground effect. In *AHS International Annual Forum & Technology Display*, number NF1676L-21054, 2015.

[8] Manikandan Ramasamy, Timothy E Lee, and J Gordon Leishman. Flowfield of a rotating-wing micro air vehicle. *Journal of aircraft*, 44(4):1236–1244, 2007.

[9] Gordon J Leishman. *Principles of helicopter aerodynamics*. Cambridge university press, 2006.

[10] IC Cheeseman and WE Bennett. The effect of the ground on a helicopter rotor in forward flight. 1955.

[11] James S Hayden. The effect of the ground on helicopter hovering power required. In *Proc. AHS 32nd Annual Forum, 1976*, 1976.

[12] J Gordon Leishman. A history of helicopter flight. *University of Maryland, Available in: http://terpconnect. umd. edu/ leishman/Aero/history.html*, 2000.

[13] Ray Leoni. ABC: The high speed helicopter. *https://sikorskyarchives.com/the-high-speed-helicopter/.*

[14] Marion K Taylor. A balsa-dust technique for air-flow visualization and its application to flow through model helicopter rotors in static thrust. Technical report, 1950.

[15] Robert D Harrington. Full-scale-tunnel investigation of the static-thrust performance of a coaxial helicopter rotor. Technical report, 1951.

[16] Richard C Dingeldein. *Wind-tunnel studies of the performance of multirotor configurations*, volume 3236. National Advisory Committee for Aeronautics, 1954.

[17] MC Cheney. The abc helicopter. *Journal of the American Helicopter Society*, 14(4):10–19, 1969.

[18] Colin P Coleman. A survey of theoretical and experimental coaxial rotor aerodynamic research. Technical report, 1997.

[19] T Nagashima, H Ouchi, and F Sasaki. Optimum performance and load sharing of coaxial rotor in hover. *J. Jpn. Soc. Aeronaut. Space Sci*, 26:293, 1978.

[20] T Nagashima and K Nakanishi. Optimum performance and wake geometry of co-axial rotor in hover. 1981.

[21] J Gordon Leishman and Monica Syal. Figure of merit definition for coaxial rotors. *Journal of the American Helicopter Society*, 53(3):290–300, 2008.

[22] Seongkyu Lee and Maxime Dassonville. Iterative blade element momentum theory for predicting coaxial rotor performance in hover. *Journal of the American Helicopter Society*, 65(4):1–12, 2020.

[23] Joon W Lim, Kenneth W McAlister, and Wayne Johnson. Hover performance correlation for full-scale and model-scale coaxial rotors. *Journal of the American Helicopter Society*, 54(3):32005–32005, 2009.

[24] Jimmy C Ho, Hyeonsoo Yeo, and Mahendra Bhagwat. Validation of rotorcraft comprehensive analysis performance predictions for coaxial rotors in hover. *Journal of the American Helicopter Society*, 62(2):1–13, 2017.

[25] Vinod K Lakshminarayan and James D Baeder. High-resolution computational investigation of trimmed coaxial rotor aerodynamics in hover. *Journal of the American Helicopter Society*, 54(4):42008–42008, 2009.

[26] KW McAlister, C Tung, O Rand, V Khromov, and JS Wilson. Experimental and numerical study of a model coaxial rotor. In *American Helicopter Society 62nd Annual Forum, Phoenix, AZ*, 2006.

[27] Lokesh Silwal, Karlyle Munz, and Vrishank Raghav. Development and validation of a thrust-scaled counter-rotating coaxial rotor to study interactional aerodynamics. In *AIAA Scitech 2019 Forum*, page 1100, 2019.

[28] Lokesh Silwal and Vrishank Raghav. Preliminary study of the near wake vortex interactions of a coaxial rotor in hover. In *AIAA SciTech 2020 Forum*, page 0305, 2020.

[29] Patrick Mortimer, Jayant Sirohi, Stefan Platzer, and Juergen Rauleder. Phase-resolved flowfield measurements of a coaxial counter-rotating rotor in hover. *Journal of Aircraft*, 60(6):1986–1997, 2023.

[30] Aditya Suvithiraj Rajendiran Vijayaraj, Lokesh Silwal, Zachary T Moore, and Vrishank Raghav. Time-averaged flowfield measurements of a coaxial rotor to understand the rotor-on-rotor interactions in hover. In *AIAA SCITECH 2024 Forum*, page 0008, 2024.

[31] Stefan Platzer, Manfred Hajek, J Rauleder, Patrick Mortimer, and Jayant Sirohi. Investigation of the flow fields of coaxial stacked and counter-rotating rotors using piv measurements and urans simulations. In *Proceedings of the Vertical Flight Society's 77th Annual Forum and Technology Display, Virtual*, pages 10–14, 2021.

[32] Dhwanil Shukla and Narayan Komerath. Drone scale coaxial rotor aerodynamic interactions investigation. *Journal of Fluids Engineering*, 141(7):071106, 2019.

[33] Montgomery Knight and Ralph A Hegner. Analysis of ground effect on the lifting airscrew. Technical report, 1941.

[34] Evan A Fradenburgh. The helicopter and the ground effect machine. *Journal of the American Helicopter Society*, 5(4):24–33, 1960.

[35] J Zbrozek. Ground effect on the lifting rotor. *ARC R&M*, 2347:1–8, 1950.

[36] Jeffrey S Light. Tip vortex geometry of a hovering helicopter rotor in ground effect. *Journal of the American helicopter society*, 38(2):34–42, 1993.

[37] Albert Betz. The ground effect on lifting propellers. Technical report, 1937.

[38] Richard E Brown and Glen R Whitehouse. Modelling rotor wakes in ground effect. *Journal of the American Helicopter Society*, 49(3):238–249, 2004.

[39] Daniel A Griffiths, Shreyas Ananthan, and J Gordon Leishman. Predictions of rotor performance in ground effect using a free-vortex wake model. *Journal of the American Helicopter Society*, 50(4):302–314, 2005.

[40] Nita Darshini Nathan. *The rotor wake in ground effect and its investigation in a wind tunnel*. PhD thesis, University of Glasgow, 2010.

[41] Joseph I Milluzzo III and J Gordon Leishman. Vortical sheet behavior in the wake of a rotor in ground effect. *AIAA Journal*, 55(1):24, 2017.

[42] Sayan Ghosh, Mark Lohry, and R Rajagopalan. Rotor configurational effect on rotorcraft brownout. In *28th AIAA applied aerodynamics conference*, page 4238, 2010.

[43] WP Schane. *Effects of downwash upon man*. US Army Aeromedical Research Unit, 1967.

[44] Manikandan Ramasamy, Mark Potsdam, and Gloria K Yamauchi. Measurements to understand the flow mechanisms contributing to tandem-rotor outwash. In *Annual Forum and Technology Display*, number ARC-E-DAA-TN21861, 2018.

[45] Lokesh Silwal, Mahendra Bhagwat, and Vrishank Raghav. Aerodynamic interactions of counter-rotating coaxial rotors hovering in ground effect. *Journal of Aircraft*, 59(6):1416–1425, 2022.

[46] Mark Miller, Geoffrey Karli, Zarif Rahman, Constantinos Kandias, Eric Greenwood, and Jose Palacios. Characterizing rotor performance changes with scale in compressed air. In *American Helicopter Society 80th Annual Forum, Montréal, Quebec, Canada*, 2024.

[47] Jeffrey D Singleton and William T Yeager Jr. Important scaling parameters for testing model-scale helicopter rotors. *Journal of Aircraft*, 37(3):396–402, 2000.

[48] Isaac Bensignor, Dhuree Seth, and Matthew McCrink. Rotor propulsion modeling for low reynolds number flow (re¡ 105) for martian rotorcraft flight. In *AIAA AVIATION 2022 Forum*, page 3958, 2022.

[49] Witold JK Koning, Ethan A Romander, and Wayne Johnson. Low reynolds number airfoil evaluation for the mars helicopter rotor. In *Annual Forum and Technology Display*, number ARC-E-DAA-TN53889, 2018.

[50] Manikandan Ramasamy, Bradley Johnson, and J Gordon Leishman. Understanding the aerodynamic efficiency of a hovering micro-rotor. *Journal of the American Helicopter Society*, 53(4):412–428, 2008.

[51] PBS Lissaman. Low-reynolds-number airfoils. *Annual review of fluid mechanics*, 15(1):223–239, 1983.

[52] Michael S Selig and James J Guglielmo. High-lift low reynolds number airfoil design. *Journal of aircraft*, 34(1):72–79, 1997.

[53] Dhwanil Shukla, Nandeesh Hiremath, and Narayanan M Komerath. Low reynolds number aerodynamics study on coaxial and quad-rotor. In *2018 Applied Aerodynamics Conference*, page 4118, 2018.

[54] Vinod K Lakshminarayan and James D Baeder. Computational investigation of microscale coaxial-rotor aerodynamics in hover. *Journal of aircraft*, 47(3):940–955, 2010.

[55] Atsushi Yamaguchi, Raoul S Golani, Koji Fujita, and Hiroki Nagai. Experimental investigation on aerodynamic performance of coaxial rotor at low reynolds numbers. In *AIAA Scitech 2021 Forum*, page 1308, 2021.

[56] Align hobby helicopter. `https://www.amainhobbies.com/250-size-main-blades-helicopters/c2227`.

[57] Christopher G Cameron, Anand Karpatne, and Jayant Sirohi. Performance of a mach-scale coaxial counter-rotating rotor in hover. *Journal of Aircraft*, 53(3):746–755, 2016.

[58] Anton J Landgrebe. The wake geometry of a hovering helicopter rotor and its influence on rotor performance. *Journal of the American Helicopter society*, 17(4):3–15, 1972.

[59] Ashish Bagai, J Gordon Leishman, and Jacob Park. Aerodynamic analysis of a helicopter in steady maneuvering flight using a free-vortex rotor wake model. *Journal of the American Helicopter Society*, 44(2):109–120, 1999.

[60] Krishnamohan R Krothapalli, JVR Prasad, and David A Peters. Helicopter rotor dynamic inflow modeling for maneuvering flight. *Journal of the American Helicopter Society*, 46(2):129–139, 2001.

[61] H. Glauert. *Airplane Propellers*, pages 169–360. Springer Berlin Heidelberg, 1935.

[62] GAM Van Kuik, Jens Nørkær Sørensen, and VL Okulov. Rotor theories by professor joukowsky: momentum theories. *Progress in Aerospace Sciences*, 73:1–18, 2015.

[63] Jens N Sørensen and Gijs AM van Kuik. General momentum theory for wind turbines at low tip speed ratios. *Wind Energy*, 14(7):821–839, 2011.

[64] Wayne Johnson. *Helicopter theory*. Courier Corporation, 2012.

[65] Benjamin R Hein and Inderjit Chopra. Hover performance of a micro air vehicle: rotors at low reynolds number. *Journal of the American Helicopter Society*, 52(3):254–262, 2007.

[66] Stephen J Kline. Describing uncertainties in single-sample experiments. *Mech. Eng.*, 75:3–8, 1963.

[67] He Zhu, Shaoxiong Wei, Hong Nie, Yuhao Du, and Xiaohui Wei. Ground effect on the thrust performance of staggered rotor system. *Drones*, 8(4):118, 2024.

[68] Ifan Hughes and Thomas Hase. *Measurements and their uncertainties: a practical guide to modern error analysis*. OUP Oxford, 2010.

[69] Vern Lindberg. Uncertainties and error propagation. *Manual on Uncertainties, Graphing and the Vernier Caliper, Part I. Rochester Institute of Technology, New York, USA.(http://www. rit. edu/uphysics/uncertinities/Uncertinitiespart2. html# addsub)*, 2000.

[70] Ronald J Adrian and Jerry Westerweel. *Particle image velocimetry*. Number 30. Cambridge university press, 2011.

[71] Bernhard Wieneke. Piv uncertainty quantification from correlation statistics. *Measurement Science and Technology*, 26(7):074002, 2015.

[72] Andrea Sciacchitano and Bernhard Wieneke. Piv uncertainty propagation. *Measurement Science and Technology*, 27(8):084006, 2016.

Appendix A

Measurement uncertainty

A.1 Load measurements

This study utilized the thrust and power coefficients, which have an associated measurement error. The thrust and power coefficients depend on the axial force and torque load measurements, angular velocity, and density. Calibration of the load cells used for the load measurements was performed using a set of standard mass blocks. The uncertainty of the measured loads with respect to the expected load of the known masses was, on average, 0.23% for the axial force (thrust) and 1.12% for the torque. The measurement error of the rotational speed was found to be $7.20\ \mathrm{RPM}$ based on the motor, ESC controller, and NPN hall sensor. The laboratory environment was temperature-controlled and was held between $21°\mathrm{C}$ and $24°\mathrm{C}$ for all experiments, and the estimated density uncertainty was $0.0073\ kg/m^3$.

The uncertainty of the thrust and power coefficients was computed using the method introduced in [66] as:

$$u_y^2 = \left(\frac{\partial y}{\partial x_1} u_{x_1}\right)^2 + \left(\frac{\partial y}{\partial x_2} u_{x_2}\right)^2 + \cdots + \left(\frac{\partial y}{\partial x_n} u_{x_n}\right)^2 \tag{A.1}$$

where y represents the thrust or power coefficient, x_n represent the dependent variables of the load coefficients, and u_{x_n} represents the error of each variable. This method was implemented for rotor load measurement uncertainty in [67]. Substituting the various measurement uncertainties, the resulting measurement error of the load coefficients was computed using:

$$\frac{\Delta C_T}{C_T} = \sqrt{\left(\frac{\Delta T}{T}\right)^2 + 4\left(\frac{\Delta \Omega}{\Omega}\right)^2 + \left(\frac{\Delta \rho}{\rho}\right)^2} \tag{A.2}$$

$$\frac{\Delta C_P}{C_P} = \sqrt{\left(\frac{\Delta Q}{Q}\right)^2 + 9\left(\frac{\Delta \Omega}{\Omega}\right)^2 + \left(\frac{\Delta \rho}{\rho}\right)^2} \tag{A.3}$$

The measurement errors of C_T and C_P were calculated to be 0.87% and 1.54%, respectively.

The uncertainty associated with the empirical power factors was calculated using the propagation of error methodology proposed in [68, 69]. The approach for quantifying error propagation of the empirical factors in this study is outlined below for a single rotor IGE, and a similar methodology was applied for the other rotor configurations and operating conditions of this study.

The initial experiment on a single rotor OGE yielded an empirical correction expressed as

$$\kappa_i \pm \delta\kappa_i$$

where $\delta\kappa_i$ was determined from the 95% confidence interval of the momentum theory curve fit. For the single rotor in-ground effect, the empirical correction took the form

$$\kappa \pm \delta\kappa, \quad \text{which decouples into} \quad (\kappa_i \pm \delta\kappa_i)(\kappa_g \pm \delta\kappa_g)$$

where $(\kappa_g \pm \delta\kappa_g)$ quantifies the ground effect experienced by the rotor since $(\kappa_i \pm \delta\kappa_i)$ was found from the single rotor OGE and considered constant so that all changes in rotor performance are encapsulated as an effect of the ground. Thus,

$$\kappa_g \pm \delta\kappa_g = \frac{\kappa \pm \delta\kappa}{\kappa_i \pm \delta\kappa_i}$$

To compute the total uncertainty in $\delta\kappa_g$, the error propagation method was used [68, 69]. In this method, the absolute uncertainty of the empirical factor is converted into a percentage uncertainty, and then the uncertainties are added together. Afterward, the percentage is

converted back to an absolute form by taking $\kappa_g/\delta\kappa_g$. By adding the uncertainties, each factor is assumed to be combined in the same direction and perfectly correlated. Therefore, the computed propagated uncertainty range provided in the figure captions of Chs. 4 and 5 is at a worst-case scenario condition, and the actual total uncertainty is likely well within that range.

A.2 Flow field measurements

The uncertainty in velocity measurements in PIV experiments primarily arises from errors in estimating particle displacements, such as calibration errors, background noise, out-of-plane particle motion, peak locking, and non-uniform particle reflection. A calibration was performed in the field-of-view (FOV) to map the camera's pixel coordinates to real-world dimensional coordinates, which introduces magnification errors. The magnification error was quantified by calculating the fit error during calibration. In the experiments conducted in this thesis, the calibration fit error was maintained below 0.3 pixels, which ensured that the magnification errors were negligible in the PIV experiments.

Peak locking occurs when particle image displacements fall close to integer pixel values, introducing a bias in velocity measurements due to sub-pixel displacements. Adrian and Westerweel recommend maintaining particle image diameters between 2-4 pixels to reduce the likelihood of peak locking [70]. To ensure the particles were of appropriate size, the camera was defocused slightly such that the particles were at least 2 pixels in diameter while the signal-to-noise ratio was at least 10-to-1 in the FOV. The probability density function (PDF) generated by the DaVis 10.1.2 software was used to verify the absence of particle peak locking, thus ensuring that the effect on measurement uncertainty was negligible.

The uncertainty in particle displacement measurements originates from estimating particle position differences across two interrogation windows. The displacement uncertainty was assessed using a statistical technique developed by Wieneke and later refined by Sciacchitano and Wieneke, which estimates the contribution of cross-correlation peak distribution to displacement vector uncertainty [71, 72]. The DaVis 10.1.2 software generated a measurement uncertainty field for the time-averaged axial velocity, as shown in Fig. A.1. The upper and lower rotor inflow and its uncertainty are shown in Figs. A.2 and A.3, and it was found that the

uncertainty of the inflow was less than 1.5% of the maximum time-averaged axial velocity for all experiments.

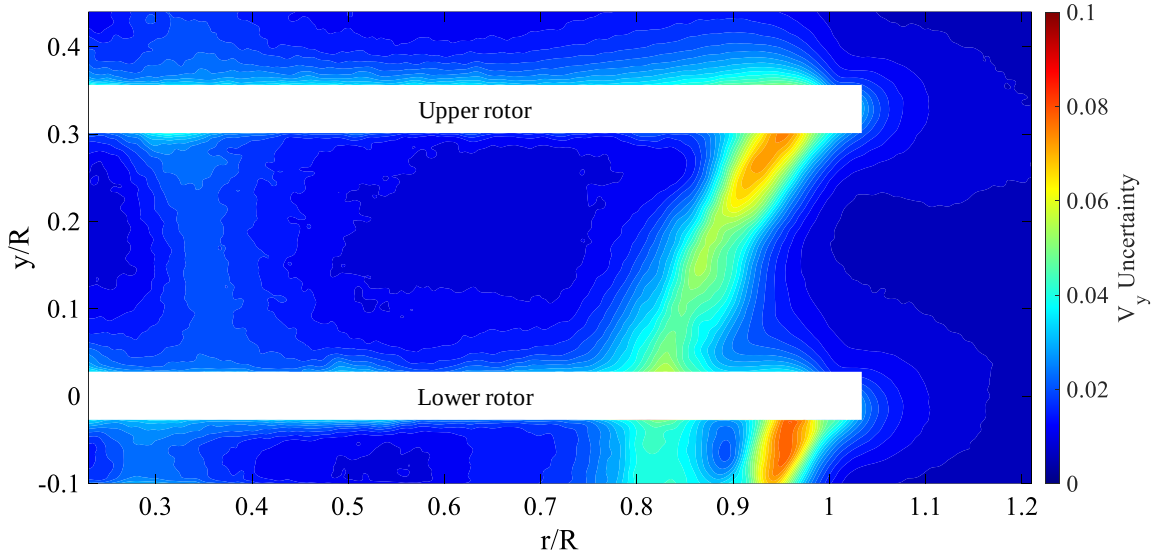

Figure A.1: Measurement uncertainty for the time-averaged axial velocity in the measurement FOV for the CCR in OGE conditions.

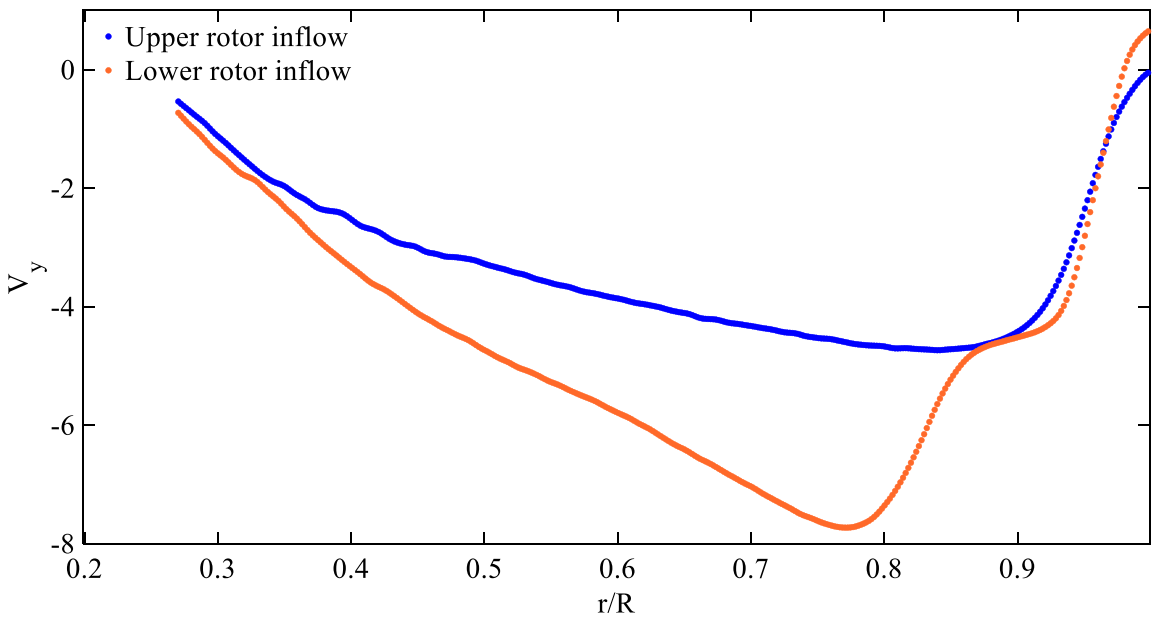

Figure A.2: Axial velocity through the upper and lower rotor planes for the CCR in OGE conditions.

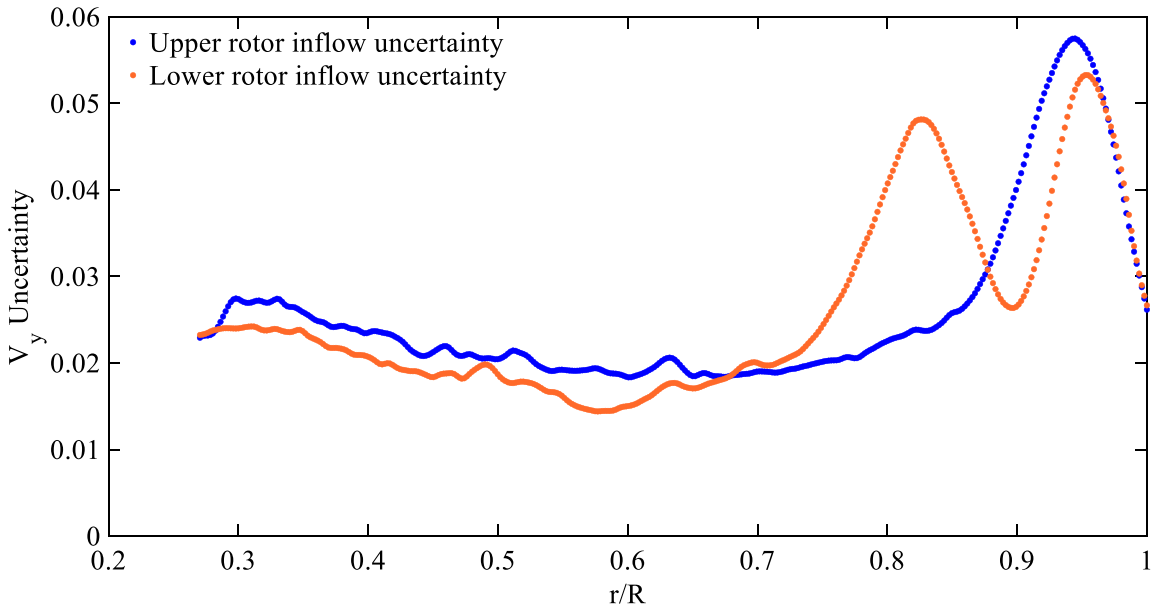

Figure A.3: Measurement uncertainty for the axial velocity through the upper and lower rotor planes for the CCR in OGE conditions.

Appendix B

Experimental facility setup and fabrication considerations

B.1 Load cell measurements and calibration

This study involved load measurements at three operational speeds, and the maximum dimensional load varied between these three (Fig. B.1 shows the loads variation across conditions for the lower single rotor OGE). To accommodate the changing loads while using a single load cell, the amplifier sensitivity was reduced as the rotational speed of the rotor decreased. This adjustment ensured that the voltage range of recorded data remained around $\pm 5V$ in the $\pm 10V$ maximum capacity. Maintaining this range was critical to avoid minute fluctuations in output voltage at lower speeds, which could have introduced measurement inaccuracies.

Calibration of the axial force sensor was conducted in both compression and tension directions, and torque calibration was performed in clockwise (CW) and counterclockwise (CCW) directions. For each direction, the load cell bias was recorded, then five known masses were placed on the load cell and data was collected for 10 seconds. This procedure resulted in 10 points for the thrust and torque calibration slopes. The resulting calibration curves for the axial force and torque across each operational speed are presented in Figs. B.2, B.3, B.4 for the lower rotor load cell, and the similar results were obtained for the upper rotor load cell. Each calibration curve had an R-squared value of 1.

B.2 Rotor and thrust stand vibration mitigation

A major challenge encountered early in the experimental campaign was a persistent structural vibration in the upper rotor during operation. This vibration was evident at all tested rotor

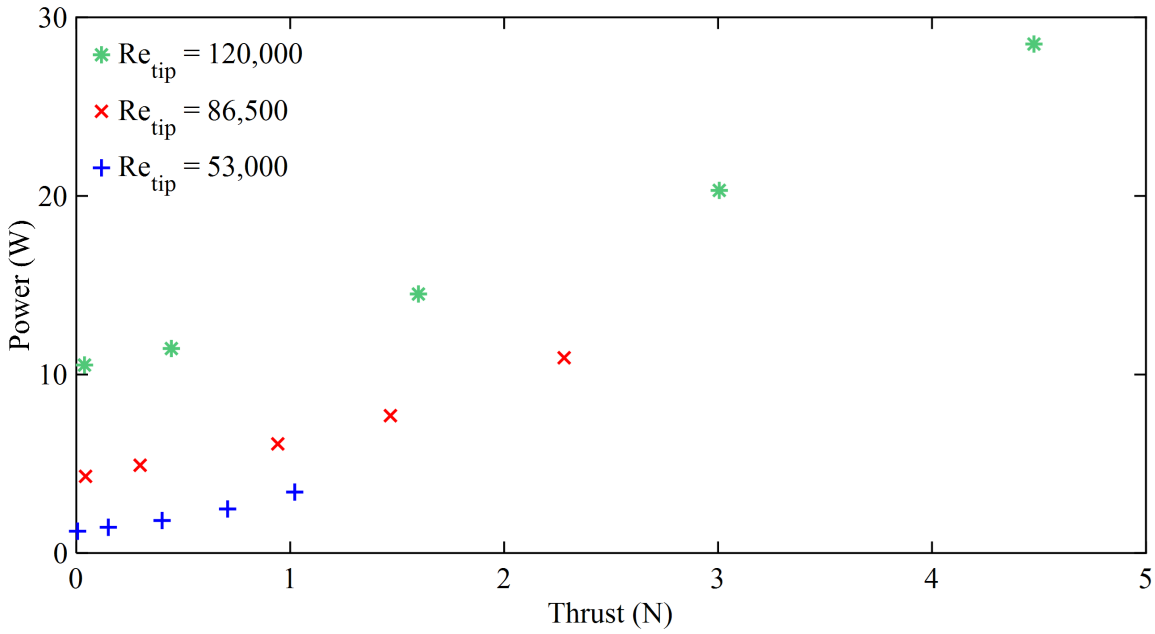

Figure B.1: Dimensionalized loads variation for the lower single rotor across the Reynolds number operating conditions of the present study.

RPMs, intensifying significantly above 2000 RPM and leading to the damage of a load cell during testing. Consequently, this issue rendered the upper rotor inoperable for an extended period, halting all coaxial rotor experiments.

To mitigate the vibration, Sorbothane strips were initially placed between each rotor assembly and its respective thrust stand to provide damping. While the approach successfully reduced vibration in the lower rotor, it proved ineffective for the upper rotor. Several attempts were made to identify the source of the vibration, including replacing various rotor components, such as the motor, transmission assembly, and structural supports. Ultimately, the source was traced to a blade imbalance, as indicated by discrepancies in blade weights shown in Table B.1. Replacement blades with nearly equal weights were subsequently acquired and installed on the upper rotor (Table B.2), after which the structural vibration was eliminated.

Table B.1: Weight of the original blades in the coaxial rotor system.

Rotor blade weights (g)	Blade 1	Blade 2	Percentage difference
Lower rotor	17.48	17.39	0.5%
Upper rotor	16.40	17.32	5.5%

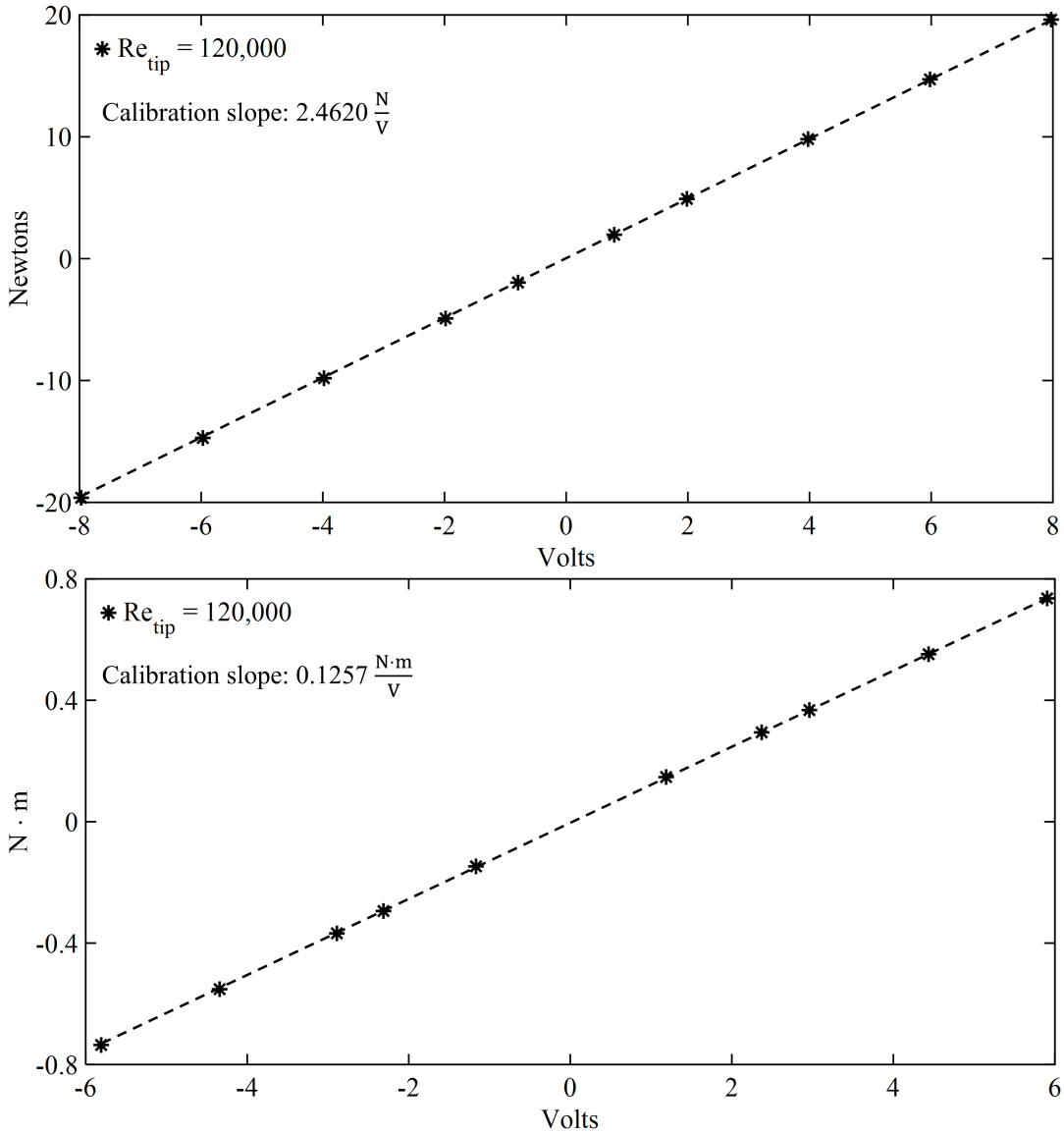

Figure B.2: Calibration curves for the lower rotor load cell operating at $Re_{tip} = 120,000$. a). Thrust. b). Torque.

Table B.2: Weight of the blades in the coaxial rotor system after replacing the upper rotor blades.

Rotor blade weights (g)	Blade 1	Blade 2	Percentage difference
Lower rotor	17.48	17.39	0.5%
Upper rotor	17.26	17.32	0.3%

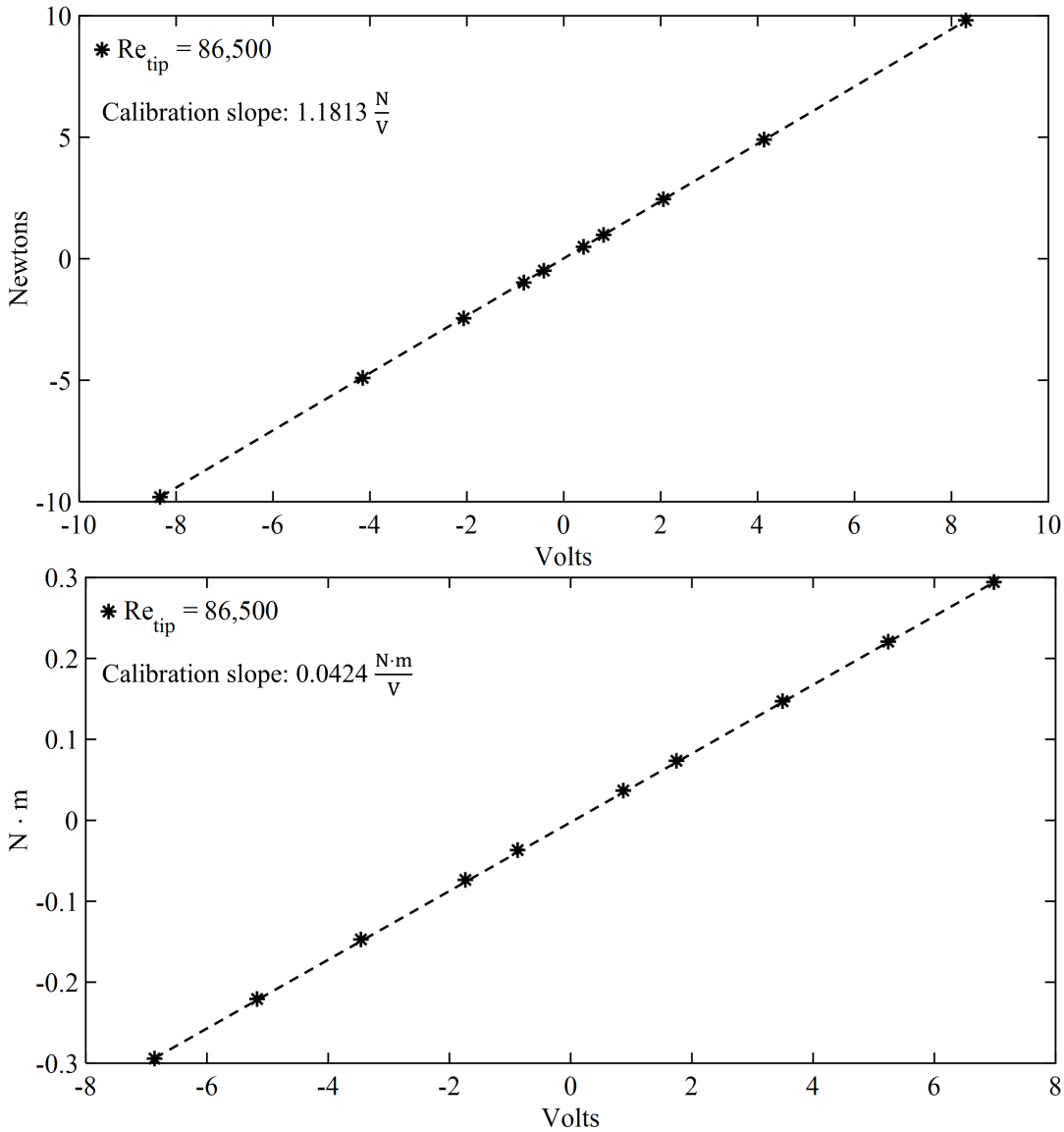

Figure B.3: Calibration curves for the lower rotor load cell operating at $Re_{tip} = 86,500$. a). Thrust. b). Torque.

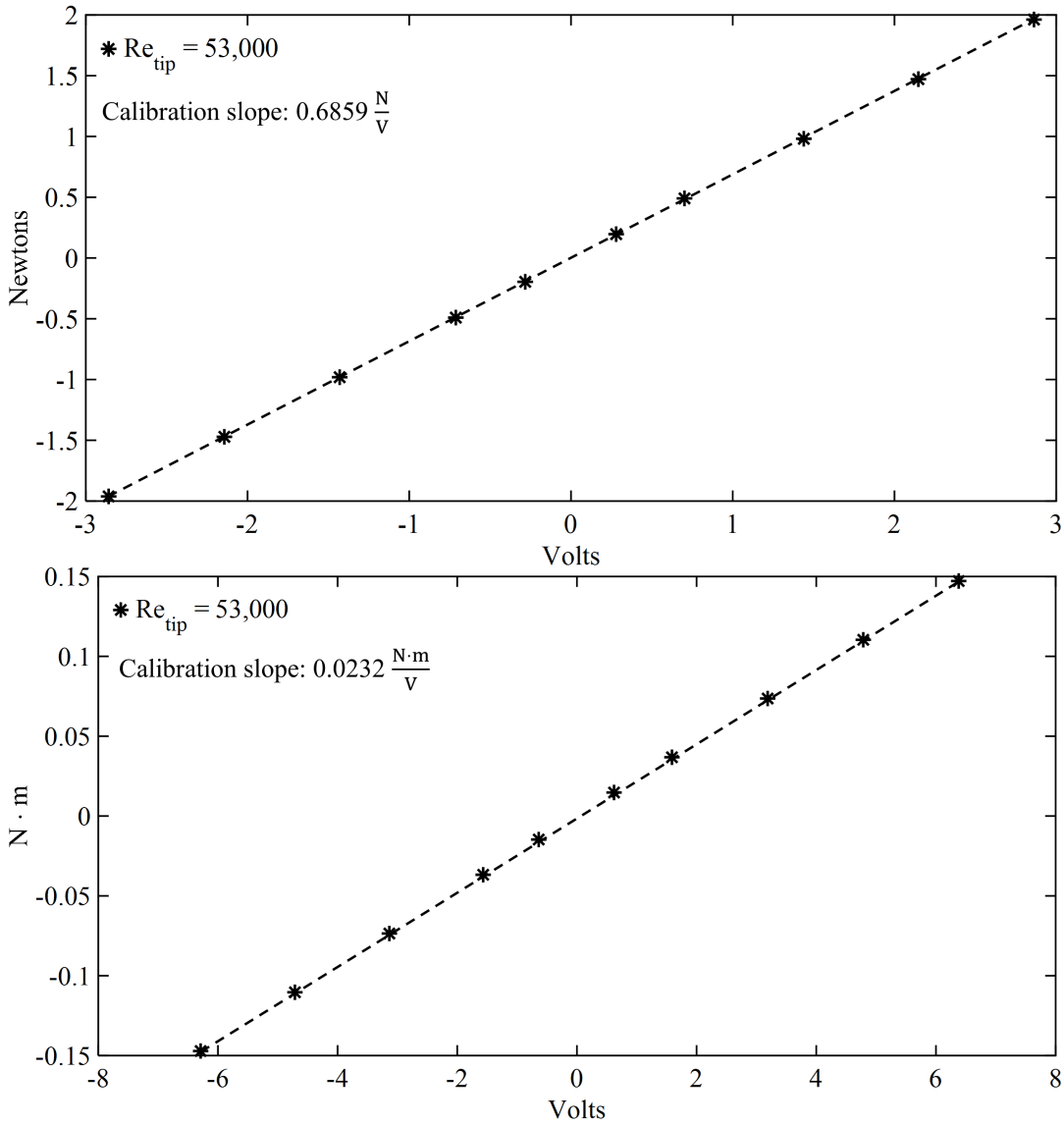

Figure B.4: Calibration curves for the lower rotor load cell operating at $Re_{tip} = 53,000$. a). Thrust. b). Torque.

Appendix C

Single rotor flow field velocity contours

The velocity fields of the single lower rotor are presented in Figures C.1 and C.2. In OGE conditions, the single rotor achieves a higher maximum axial velocity, which decreases by approximately $1m/s$ under IGE conditions due to ground interference. A similar upwash region is observed near the rotor hub, delineating the influence of ground-induced recirculation. In IGE conditions, the wake of the lower rotor initially contracts, accompanied by an axial velocity acceleration. However, as the wake approaches approximately $0.1R$ below the rotor plane, the flow begins to deflect radially outward and subsequently convects parallel to the ground surface, indicating strong ground interaction effects.

The axial velocity contours highlight the complex interplay between rotor inflow dynamics, slipstream behavior, and ground effect in both single and coaxial rotor configurations. The axial velocity distributions and wake characteristics provide critical insights into the source of aerodynamic losses and interactional effects inherent to ground proximity operations, underscoring the importance of inflow analysis in understanding rotor system performance.

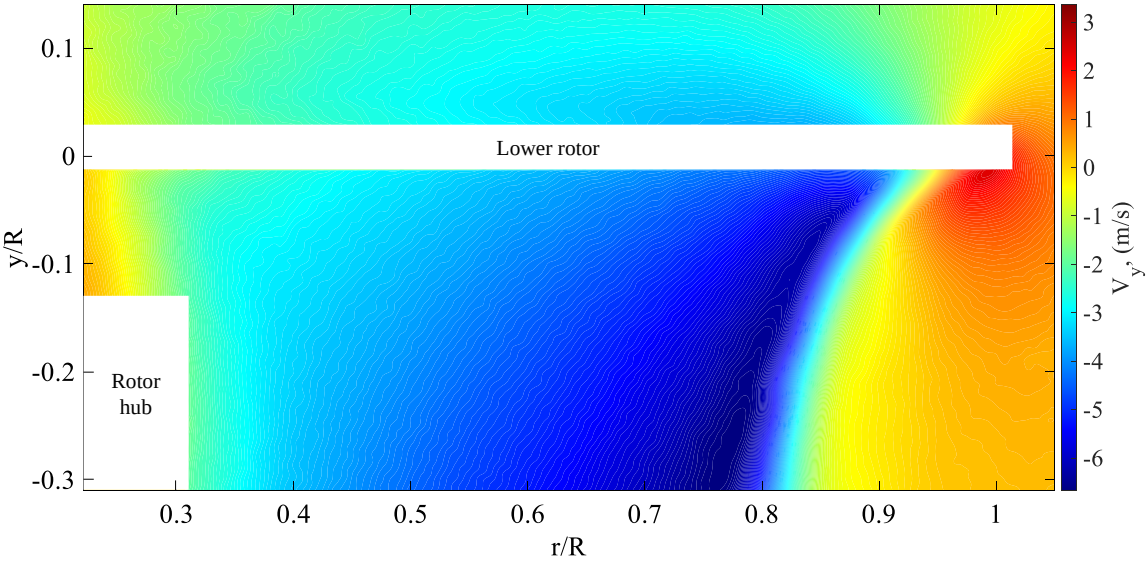

Figure C.1: Axial velocity contour for the lower single rotor operating in OGE conditions.

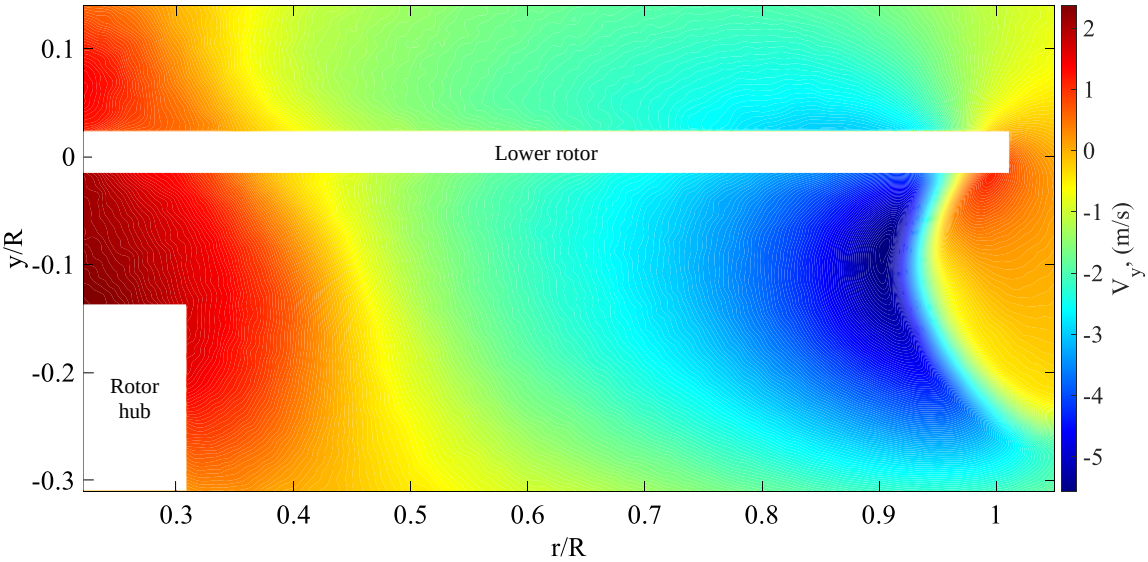

Figure C.2: Axial velocity contour for the lower single rotor operating in $z/R = 0.4$ conditions.

Appendix D

Reynolds number effect on the aerodynamic interactions

D.1 Net ground effect on the coaxial rotor

The net rotor-ground interactions are presented in Figs. D.1, D.2, D.3. Analysis of the net-ground effect showed subtle changes in the ground effect of the overall CCR system and the individual rotors, indicating that the ground proximity influences rotor-rotor interactions across all Reynolds number conditions.

In Fig. D.1, the overall interferences are presented and highlight a notable difference between the highest Reynolds number condition and the lower conditions. At the highest condition, the ground effect remained the same for all d/R conditions at one z/R. However, the net ground effect at the two lower Reynolds number conditions reduced as the d/R increased. This observation was most pronounced at smaller z/R conditions and underscores the changing rotor-rotor interactions with variation in Reynolds number.

As seen in Fig D.2, the upper rotor at the two lower Reynolds number conditions experienced a similar net ground effect to the highest case, where the single upper rotor experienced less net ground effect than the upper rotor in CCR configuration, particularly in the most extreme IGE condition. As was discussed in Ch. 4, this does not necessarily signal that the upper rotor in CCR performs better than the single rotor at the same ground height; it only signifies that the ground acts to reduce the rotor-rotor interactions, hence improving the net ground effect. The reduced rotor-rotor interactions were shown in Sec. 5.2.2.

The lower rotor net ground effect as Reynolds number changes is shown in Fig. D.3. More intriguing trends were observed here, which underscore the results discussed in Sec. 5.2.2. At

the highest two Reynolds number conditions, where the rotor-rotor interactions in the presence of the ground were observed to be similar, the net ground effect was similar. However, at the lowest Reynolds number condition, the lower rotor in CCR had a greater net ground effect than the single rotor. This suggested that the ground effect reduced the rotor-rotor interactions and was validated through analysis of the rotor-rotor interactions in the presence of the ground. The improved performance of the lower rotor at this Reynolds number condition may follow the swirl recovery hypothesis posed by [32, 53].

Overall, the analysis of the net ground effect served to prove that rotor-rotor interactions in the presence of the ground change; however, it cannot provide significant information about solely the rotor-ground interaction since the definition describes the comparison between IGE and OGE conditions, where the rotor-ground and rotor-rotor interactions are subject to change. A separate definition describing the rotor-rotor interactions in the presence of ground isolates the rotor-rotor interactions from the ground effect. The Reynolds number impact on this definition was discussed in deeper detail in Sec. 5.2.2.

D.2 Comparison of the rotor-rotor interactions in the presence of the ground with rotor-rotor interactions experienced in OGE conditions

The change in rotor-rotor interactions between IGE and OGE are presented in Figs. D.4, D.5, D.6. This definition compares how the rotor-rotor interactions change to those in OGE conditions. It provides a measure of how the ground alters the interactions (see Sec. 3.3 and 4.2.3 for further discussion of these empirical factor's meanings and their application to the experimental data).

Fig. D.4 shows how the overall CCR interferences change, and the main observation was that the ground served to reduce the interferences at the lowest Reynolds number conditions. This signified that the influences of each rotor on the other at this condition drive the CCR to experience less severe rotor-rotor interactions IGE, which was further elucidated by comparing the influences of the upper and lower rotors individually.

Fig. D.5 breaks down the interferences to show the influence of the lower rotor on the upper rotor, and it was observed that the interactional changes follow a similar trend across all Reynolds number conditions, signifying that the change in the overall interferences does not

originate with the performance of the upper rotor. However, the lower rotor showed drastic changes in the interaction comparison, as seen in Fig. D.6. The two highest Reynolds number conditions highlight similar performance trends, where the interferences were significantly increased at the most extreme IGE condition. The lowest Reynolds number condition was starkly different, where the rotor-rotor interactions IGE were less than OGE at the most extreme IGE condition. As discussed in Sec. 5.2.2, the physics driving this trend is undetermined and beyond the scope of this thesis. However, it was hypothesized that fundamental differences in the upper rotor's wake structure at the lowest Reynolds number condition are less impactful to the performance of the lower rotor upon impingement.

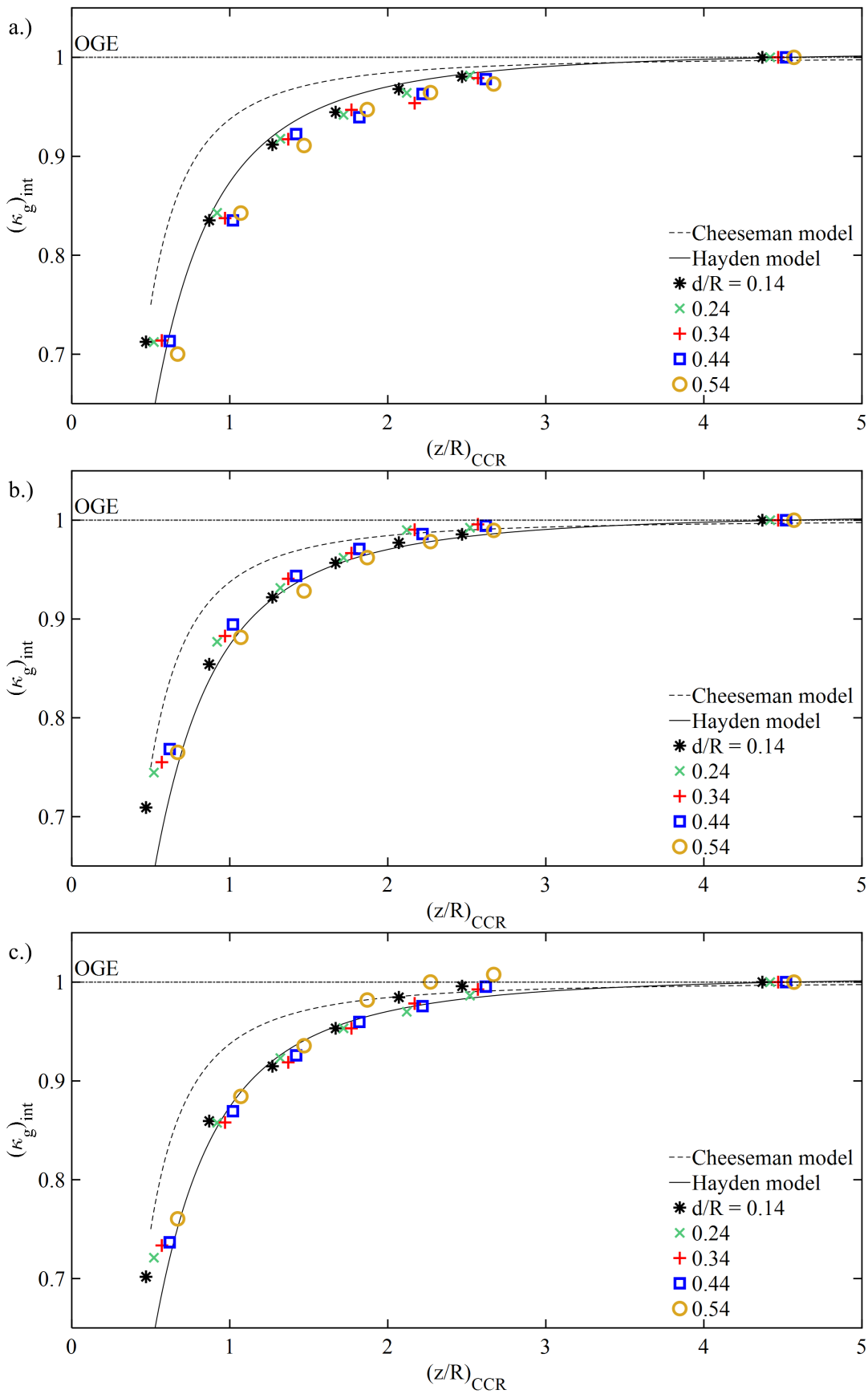

Figure D.1: Rotor-ground interactions of a CCR operating in IGE conditions. a). $Re_{tip} = 120,000$. b). $Re_{tip} = 86,500$. c). $Re_{tip} = 53,000$. The total uncertainties for all Re_{tip} conditions are within ± 0.095.

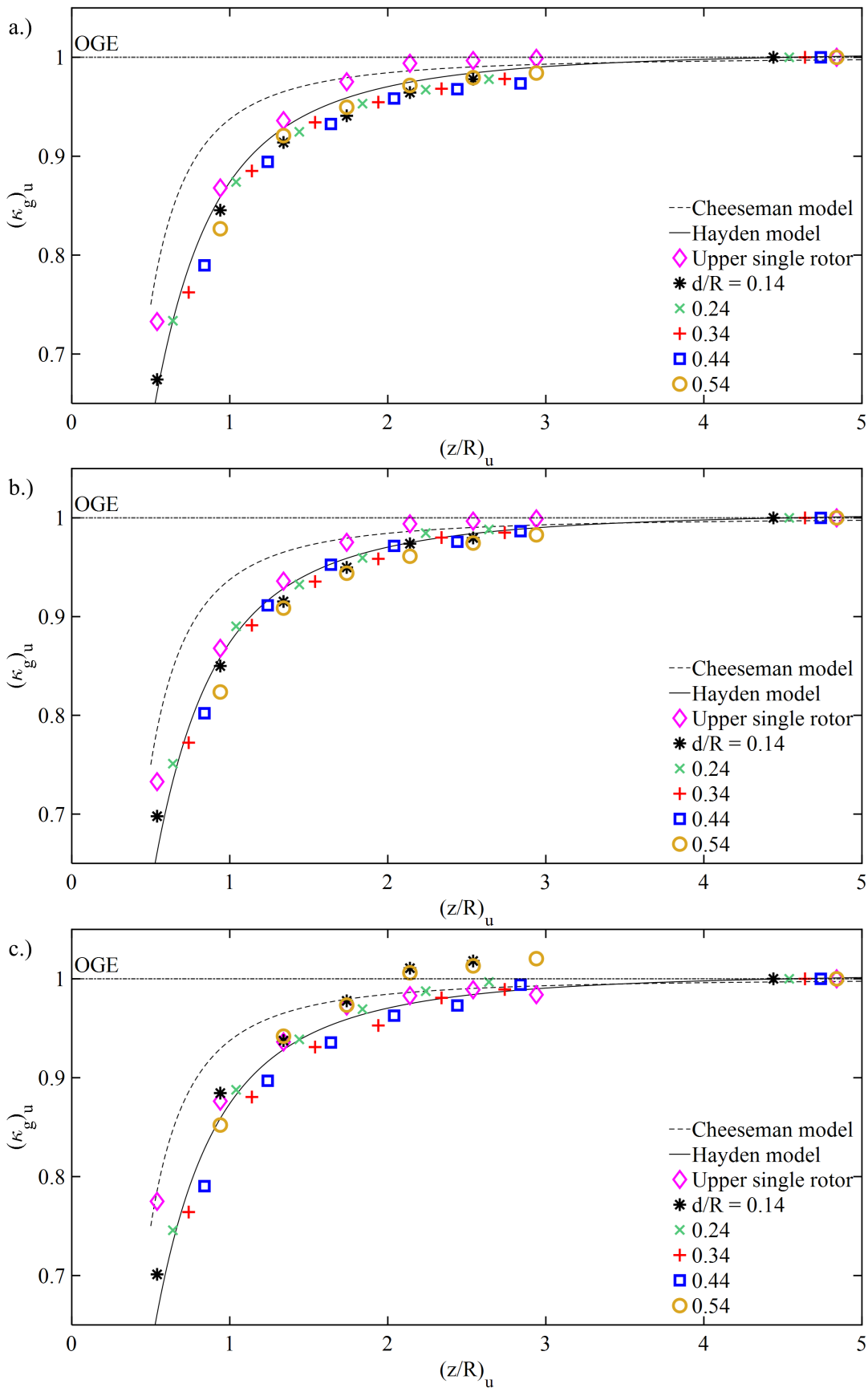

Figure D.2: Rotor-ground interactions of the upper rotor in the CCR operating in IGE conditions. a). $Re_{tip} = 120,000$. b). $Re_{tip} = 86,500$. c). $Re_{tip} = 53,000$. The total uncertainties for all Re_{tip} conditions are within ± 0.090.

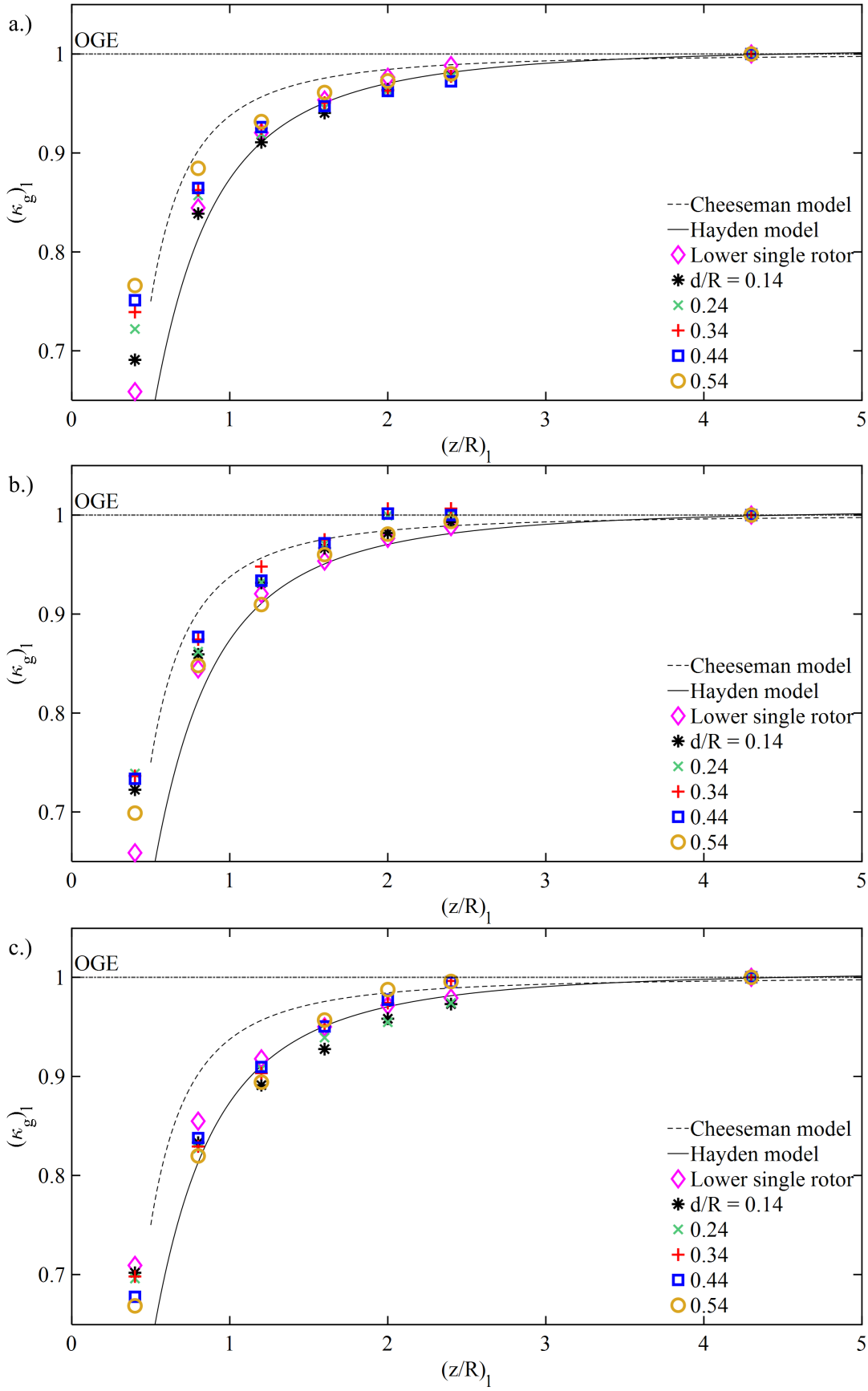

Figure D.3: Rotor-ground interactions of the lower rotor in the CCR operating in IGE conditions. a). $Re_{tip} = 120,000$. b). $Re_{tip} = 86,500$. c). $Re_{tip} = 53,000$. The total uncertainties for all Re_{tip} conditions are within ± 0.100.

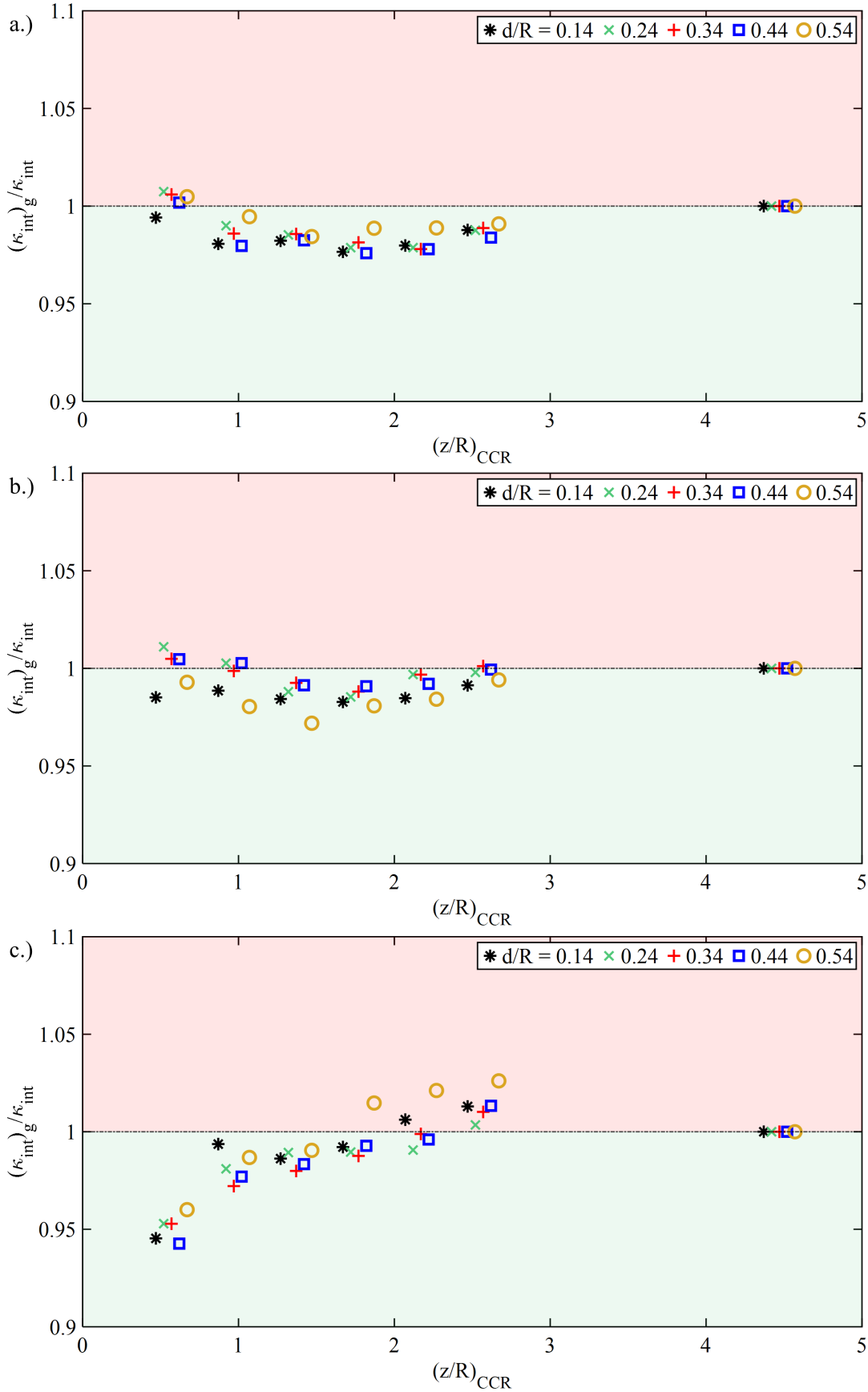

Figure D.4: Net change in aerodynamic interactions of the CCR IGE when compared to the aerodynamic interactions experienced in OGE conditions. a). $Re_{tip} = 120,000$. b). $Re_{tip} = 86,500$. c). $Re_{tip} = 53,000$.

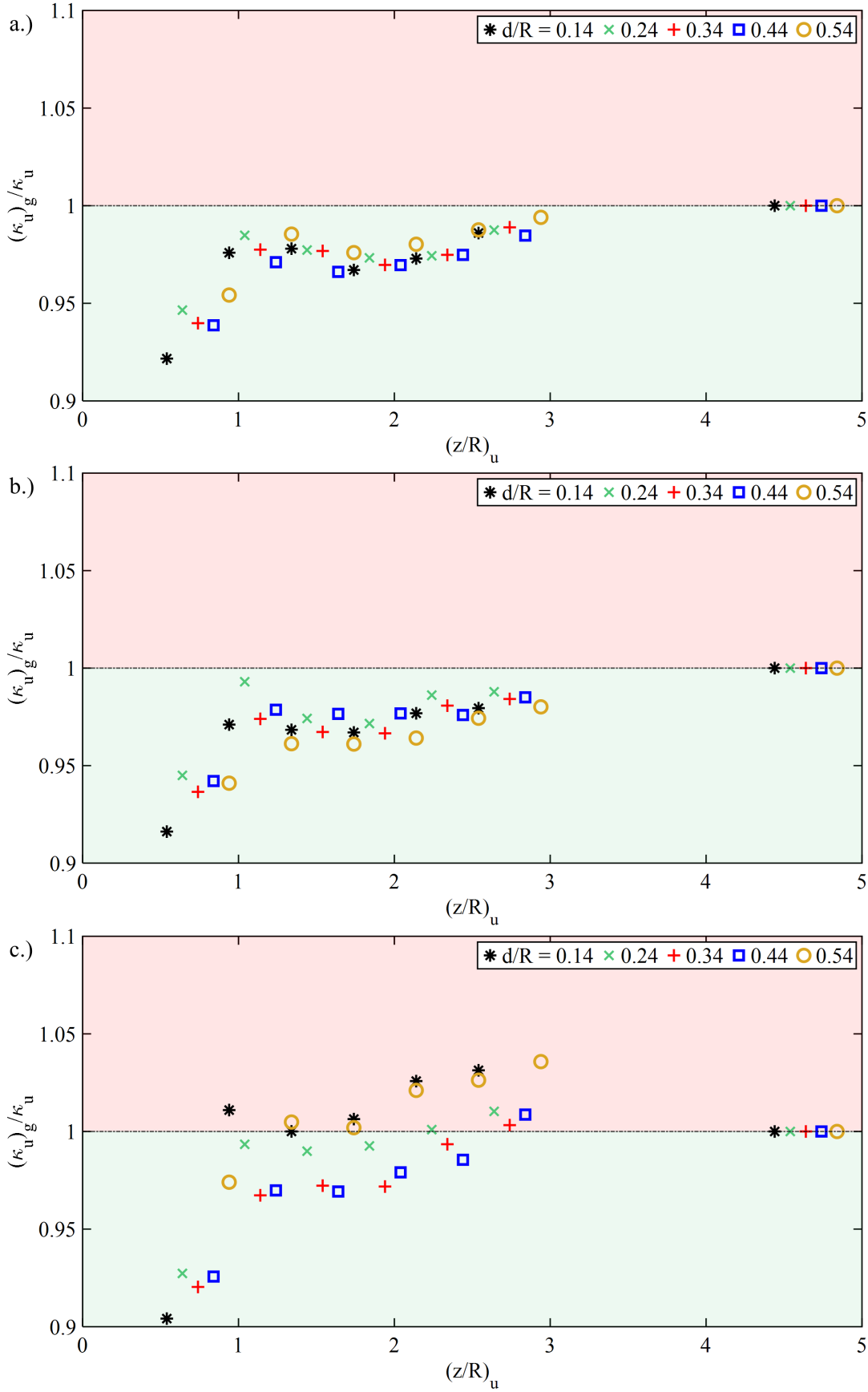

Figure D.5: Net change in aerodynamic interactions of the upper rotor in the CCR IGE when compared to the aerodynamic interactions experienced in OGE conditions. a). $Re_{tip} = 120,000$. b). $Re_{tip} = 86,500$. c). $Re_{tip} = 53,000$.

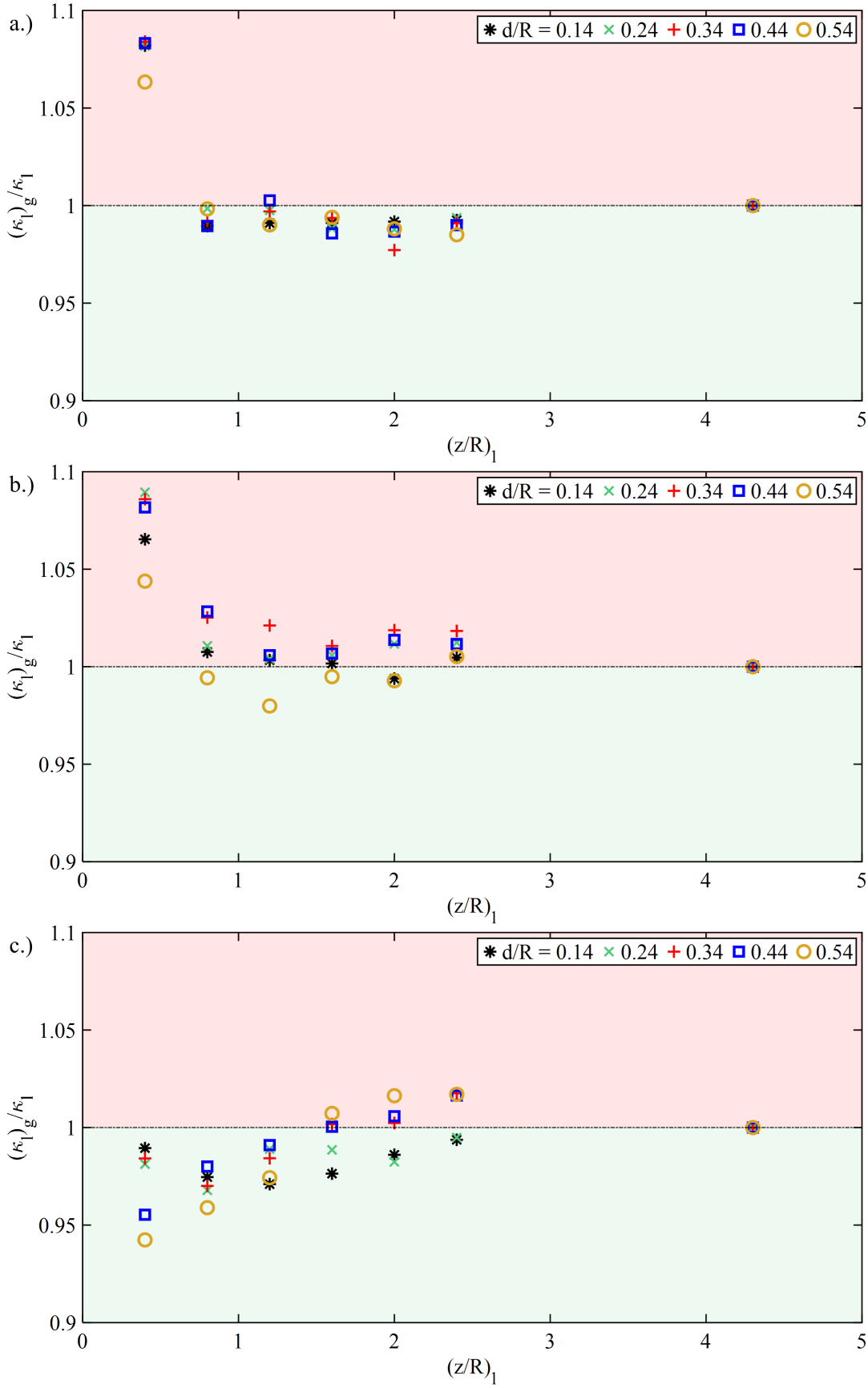

Figure D.6: Net change in aerodynamic interactions of the lower rotor in the CCR IGE when compared to the aerodynamic interactions experienced in OGE conditions. a). $Re_{tip} = 120,000$. b). $Re_{tip} = 86,500$. c). $Re_{tip} = 53,000$.

Appendix E

Products during the graduate program

Manuscripts under review/preparation

- Manuscript under review: **Moore, Z.**, Silwal, L., Vijayaraj, A., and Raghav, V., *"Aerodynamic Interference Factors for Counter-Rotating Coaxial Rotors Hovering In-Ground Effect"*, Journal of the American Helicopter Society, 2024.
- Conference paper in progress: Vijayaraj, A., **Moore, Z.**, and Raghav, V., *"Downwash and outwash of counter-rotating coaxial rotors hovering in-ground effect"*, VFS Forum 81, 2025.

Conference publications

- **Moore, Z.**, Silwal, L., Vijayaraj, A., and Raghav, V., *"Quantification of the Aerodynamic Interference for Counter-Rotating Coaxial Rotors In-Ground Effect"*, VFS Forum 80, 2024.
- **Moore, Z.**, Silwal, L., Vijayaraj, A., and Raghav, V., *"Reynolds number effects on the interference factors for a counter-rotating coaxial rotor"*, AIAA SciTech 2024 Forum.
- Vijayaraj, A., Silwal, L., **Moore, Z.**, and Raghav, V., *"Time-averaged flowfield measurements of a coaxial rotor to understand the rotor-on-rotor interactions in hover"*, AIAA SciTech 2024 Forum.

Posters and presentations

- **Moore, Z.**, Silwal, L., Vijayaraj, A., and Raghav, V., *"An Experimental Investigation on the Aerodynamic Interactions of Counter-Rotating Coaxial Rotors"*, Council of Engineering Graduate Students, Graduate Engineering Research Showcase, Auburn University.